# Magnetoelectric Properties of Epitaxial Spinel Oxide Thin Films

**Author:**
Zhou, Dongyi

**Publication Date:**
2016

**DOI:**
https://doi.org/10.26190/unsworks/19253

# MAGNETOELECTRIC PROPERTIES OF EPITAXIAL SPINEL OXIDE THIN FILMS

**DONGYI ZHOU**

A thesis in fulfilment of the requirements for the Degree of Doctor of Philosophy

**School of Materials Science and Engineering**

**Faculty of Science**

**University of New South Wales**

November 2016

# ACKNOWLEDGEMENTS

Many people have provided strong support throughout this work and I would like to take this opportunity to thank all of them.

First and foremost, I would like to thank my supervisor Prof. Nagarajan Valanoor who offered me the opportunity to work under him. He gave me clear instructions and guidance throughout the project which enriched my intellectual capabilities. I would also like to thank Prof. Paul Munroe, Prof. Jan Seidel and my co-supervisor Dr. Danyang Wang who gave me encouragement and advice on the project.

Next, I would like to express my thanks to the collaborators who performed various measurements in this work: Dr. Ryota Takahashi, Ms. Yanyu Zhou, Mr. Dohyung Kim, Dr. Qing He, Dr. Kumar Suresh, Dr. Vishal Thakare, Prof. Mikk Lippmaa and Prof. Ying-Hao Chu. Without their support, I could not have finished this thesis.

Thanks to the group members of our team: Dr. Jeffrey Cheung, Dr. Qi Zhang, Dr. Jason Chen, Dr. Ronald Maran, Dr. Vivian Liu, Dr. Daniel Sando, Mr. Guangqing Liu, Ms. Xuan Cheng and Ms. Solmaz Jahangir. Thanks for their support.

Many thanks to the school administration staff and technical staff of the labs. Thanks to Dr. Yu Wang and Mr. Sean Lim for their support in the Analytical Centre.

Finally but most importantly, I thank my parents and other members in my family for their moral support. In particular I thank my wife. Her love, support and encouragement has made this work a reality.

The financial support from the Australia-India Strategic Research Fund (Grant No.:ST060022) is gratefully acknowledged.

# PREFACE

Non-collinear spinel multiferroics, which have an $AB_2O_4$ structure, have attracted a great deal of attention in the past few years. Amongst them, the one that has drawn great attention is spinel vanadate, $FeV_2O_4$ (FVO), which has transition metal elements at both A and B sites. The interplay among the spin, orbital and lattice degrees of freedom makes FVO a very complex system which exhibits interesting properties. This thesis focuses on the growth and functional characterization of high quality FVO epitaxial thin films on perovskite $SrTiO_3$ substrates. The magnetic and electrical properties of FVO films are presented as well as the characterization of magnetoelectric coupling of the material. Secondly, another unique spinel, Cobalt Chromite, $CoCr_2O_4$ (CCO), which has a canted conical magnetic ordering and shows spontaneous polarization, is also studied in this thesis. The polarization and resistivity switching behaviour of CCO/LSMO ($CoCr_2O_4/La_{6.6}7Sr_{3.33}MnO_3$) heterostructure is also investigated.

The thesis is organized into 7 chapters to give a systematic discussion. In Chapter 1, the structure and physical properties of spinel FVO and CCO are introduced. The background theory and experimental methods, which are used in the following chapters, are presented in Chapter 2. The general theories of ferromagnetic, ferroelectric and multiferroics are introduced in this chapter, followed by physical models for dielectric constant and resistivity. The basics of the methods employed are also discussed. In Chapter 3, the growth method and the structural characterization of epitaxial FVO films on STO substrates are presented. The effects of pulsed laser deposition (PLD) growth conditions on the FVO films are discussed and structural characterization by X-ray diffraction (XRD), atomic force microscopy (AFM), transmission electron microscopy (TEM), etc. are presented. In Chapter 4, the electron and spin states of FVO films, studied by X-ray absorption spectroscopy (XAS) and X-ray magnetic circular dichroism (XMCD) are presented, followed by the magnetic properties as measured by superconducting quantum interference device (SQUID) and magnetic force microscopy (MFM). In Chapter 5, the dielectric properties of FVO films are investigated by measuring the capacitance

of a Pd/FVO/Nb:STO junction, and the magnetocapacitance effect of the material is also presented. The fabrication of CCO/LSMO heterostructure is described in Chapter 6 and its polarization and resistivity switching behaviour are discussed. The conclusions of this thesis, and the directions of possible future related work, are provided in Chapter 7.

# Table of Contents

# List of Figures

# List of Tables

# Publications

1. D. Zhou, R. Takahashi, Y. Zhou, D. Kim, V.K. Suresh, Y.Chu, Q.He, P. Munroe, M. Lippmaa, J. Seidel and N. Valanoor, Magnetic and Magnetodielectric Properties of Iron Vanadate Thin Films, Accepted by Advanced Electronic Materials, Nov. 2016
2. Y. Zhou, D. Zhou, D. R. G. Mitchell, N. Valanoor & P. Munroe, (2015). Analysis of interfacial structure and chemistry inFeV2O4-based heterostructures on (001)-oriented SrTiO3. Journal of Physics: Conference Series, 644 012003-1-012003-4.

# CHAPTER ONE

# 1 INTRODUCTION TO TMO SPINELS

## 1.1 Introduction

Transition metal oxide (TMO) spinels with a chemical formula $AB_2O_4$ have recently attracted considerable attention. Because of their complex interaction among the spin, orbital and crystal lattice degrees of freedom,[1] TMO spinels emerge as materials with spintronic[2] related properties. As a geometrically frustrated pyrochlore lattice, which is a network of corner-sharing tetrahedral system, the B site sub-lattice in the spinels induces complicated exchange interactions.[3] Efforts have been made to obtain a deeper insight into the links between their ferromagnetic properties,[4-5] polar properties[6-7] and electronic structures[8].

Simultaneously, this family of compounds has also been intensively explored as non-collinear multiferroics (NCMs),[6] an exciting new class of functional materials.[9] NCMs have a spiral magnetic structure, which breaks the space-inversion symmetry and induces ferroelectricity;[10-11] thus both magnetic and ferroelectric order parameters are directly coupled. The inherent helicity in the magnetic spin order induces charge (polarization) in the lattice, which leads to a delicate interplay between lattice strain, polar charge, electronic spin and orbital bonding in NCMs.[12] Also, these materials typically exhibit strong ferrimagnetic (or ferromagnetic) ordering rather than the anti-ferromagnetic ordering found in the currently popular $BiFeO_3$.

Despite these interesting reports and the potential of the non-collinear multiferroism in this material, the multiferroic or magnetoelectric properties of such spinels in thin film form are not known. Fundamentally, the ability to fabricate these materials in phase-pure epitaxial thin film form allows for two benefits. Firstly, it sheds insight into the intrinsic properties, without the complications inherent in grain boundaries or secondary phases. Secondly, it opens new opportunities to tailor or create novel properties using the precise

control offered by epitaxial strain and/or the defined crystallographic orientations resulting from the epitaxy process. Thin films also offer potentially new ways in which the ferroic order parameter coupling can be exploited to make useful practical devices, particularly those that could be integrated such as logic, memory and sensor technologies.

This thesis focuses on the synthesis of non-collinear spinel thin films on perovskite substrate, and their potential multiferroic or magneto-electric properties.

## 1.2 Spinel Structure

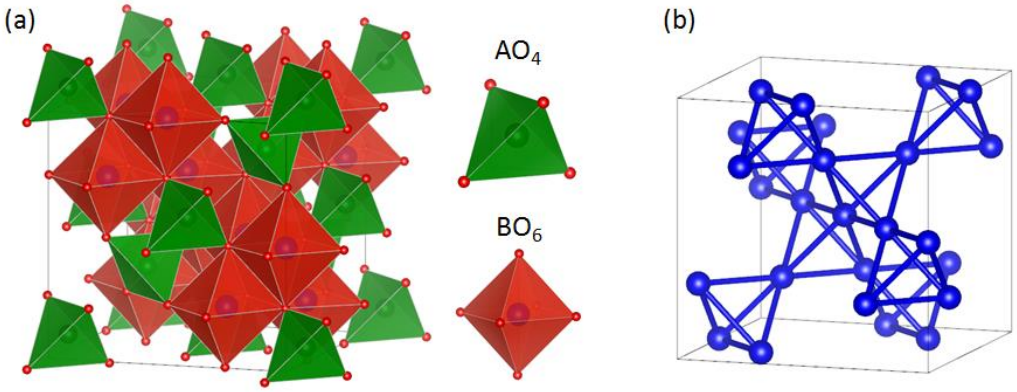


**Figure 1.1** (a) The spinel structure. The divalent A ions sit at the centre of tetrahedral sites, and the trivalent B ions sit at the centre of octahedral sites. (b) B site ions form a corner shared tetrahedral pyrochlore sub-lattice.

Crystals with the general formula $AB_2X_4$ (A and B are cations; X is an anion) having the same structure as the mineral, $MgAl_2O_4$, are named after their parent compound as 'spinel'. Bragg and Nishikawa were the first researchers to determine the structure of spinel. It belongs to the space group $Fd3m$. In spinel, the anion sublattice is arranged in a close-packed (ccp) spatial arrangement creating a total of 96 interstices between the anions in the unit cell. However, only 24 of them are occupied by cations. 8 out of 64 tetrahedral interstices (A site) are occupied by divalent cations, and 16 trivalent cations occupy half of the remaining

32 octahedral interstices (B site). This kind of spinel structure is known as 'normal spinel', while in an 'inverse spinel', the divalent ions share half of the locations of the trivalent ions, and the formula can be written as $B(AB)O_4$.

The crystal lattice arrangement for normal spinels are shown in **Figure 1.2** by layers along the [001] axis. Although anions are located in the ideal position in **Figure 1.2**, they are usually dilated away from the ideal locations which will induce changes in bond lengths, angles, interstice volumes and the symmetries of co-ordinated polyhedral, which further lead to the changes in electrical and magnetic properties of the crystal.

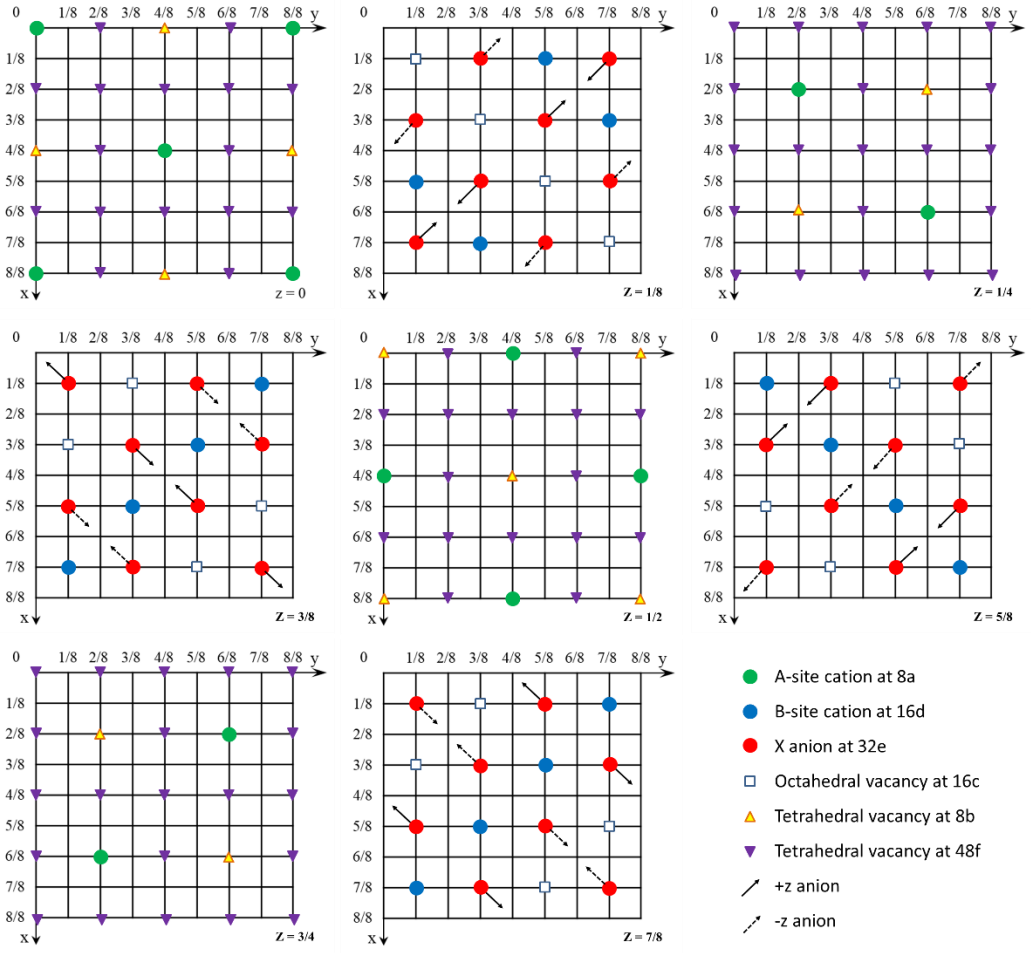


**Figure 1.2** Lattice sites in spinel, as a function of height along the [001] cubic cell axis. Layer sequence is shown at intervals of a/8. Solid arrows denote anion sublattice dilations along +z, dashed arrows indicate dilations along –z. Adapted from Ref. [13]

## 1.3 Iron Vanadate

The interplay between spin, orbit, charge and lattice degrees of freedom plays an important role in determining the various properties of materials. Spinel vanadate ($AV_2O_4$) with transition-metal elements ($Mn^{2+}$, $Fe^{2+}$,$Co^{2+}$) at the A sublattice are Mott insulators. B site Vanadium ($V^{3+}$) cations on the pyrochlore sublattice have a high-spin $3d^2$ electron configuration in the triply degenerate $t_{2g}$ states. They usually have two phase transitions at low temperature. Amongst them, Iron Vanadate, $FeV_2O_4$ (FVO), which has divalent $Fe^{2+}$ ions with the $3d^6$ high-spin electron configuration in the doubly degenerate $e_g$, is unique. Having both A site ($Fe^{2+}$) and B site ($V^{3+}$) ions with orbital degrees of freedom, it exhibits interesting properties.

Studies by T. Katufuji[14] and G.J. MacDougall[4] have shown that, unlike other spinel vanadate, FVO undergoes three phase transitions as the temperature decreases from room temperature. **Figure 1.3** shows the X-ray powder diffraction (a), the lattice parameters (b) and the distortion of O-O and V-O bonds (c) as a function of temperature. The inset in **Figure 1.3**(a) shows the FVO(440) peak(s). At 150 K it is a single peak indicating a cubic spinel structure. As the temperature drops, the peak splits into two at 110 K, and then further splits into three peaks at 90 K. Finally, at 60 K, the peaks merge into two peaks again. This phenomena suggests that the crystal changes from cubic, to tetragonal, to orthorhombic and back to tetragonal again, with decreasing temperature. The temperature dependence of the lattice parameters are shown in **Figure 1.3**(b), revealing the phase transition temperatures are ~140 K (from cubic to tetragonal), ~110 K (from tetragonal to orthorhombic) and ~70 K (from orthorhombic to low-temperature orthorhombic). Evidence of these three phase transitions is also seen in neutron powder diffraction (NPD)[4] and heat capacity[6] measurements, as shown in Figure 1.4 and Figure 1.5

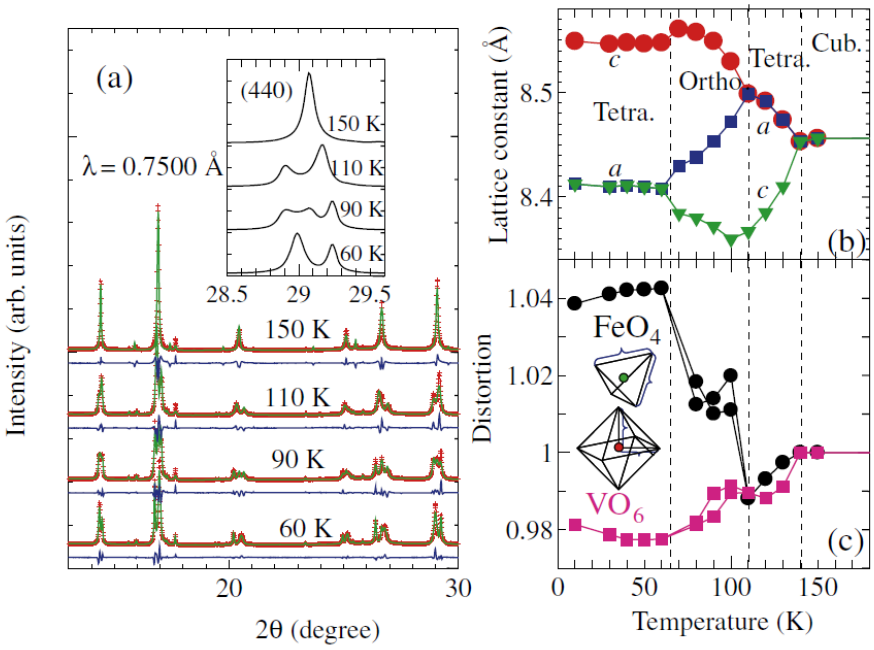


**Figure 1.3** (a) XRD 2θ pattern of FVO at different temperatures. (b) Temperature dependence of the lattice constant. (c) Temperature dependence of the distortion ratio of the O-O and V-O bonds. Adapted from Ref. [14]

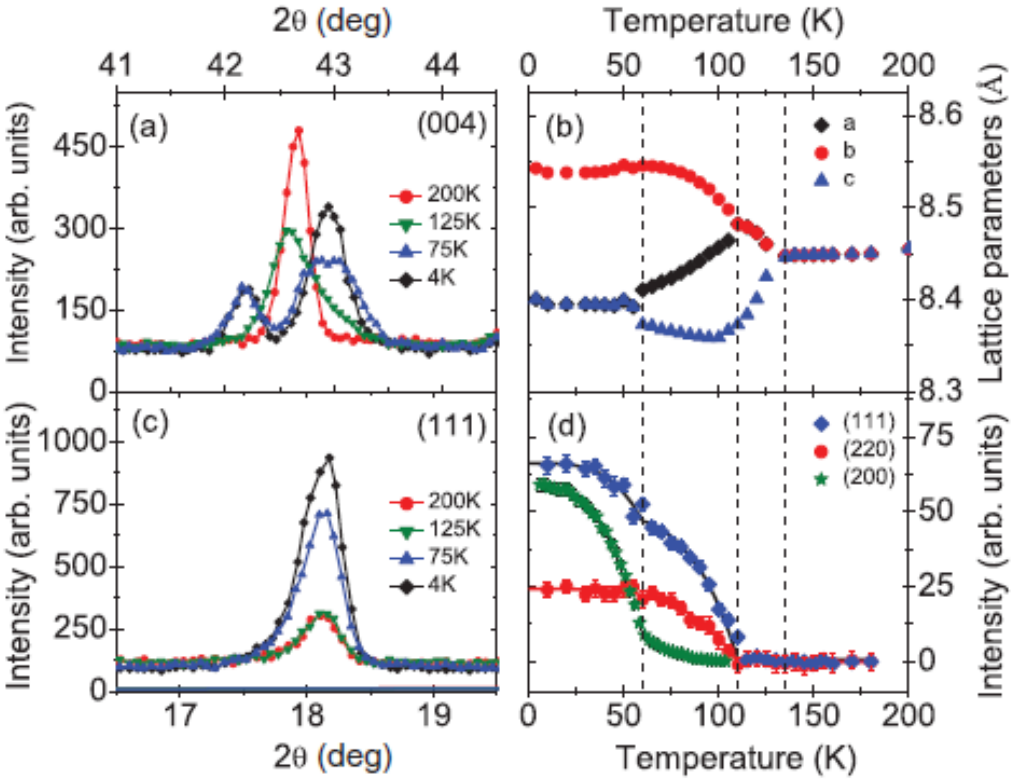


**Figure 1.4** (a) NPD data around the cubic (004) peak of FVO crystal. (b) Plot of the lattice parameters. (c) NPD data around the cubic (111) peak of FVO crystal. (d) A comparison of the temperature evolution of NPD (111) and (220) Bragg peak intensities above their values at 180 K. Overlaid is the scaled intensity of the (200) Bragg peak, as measured in a single-crystal sample. Adapted from Ref.[4]

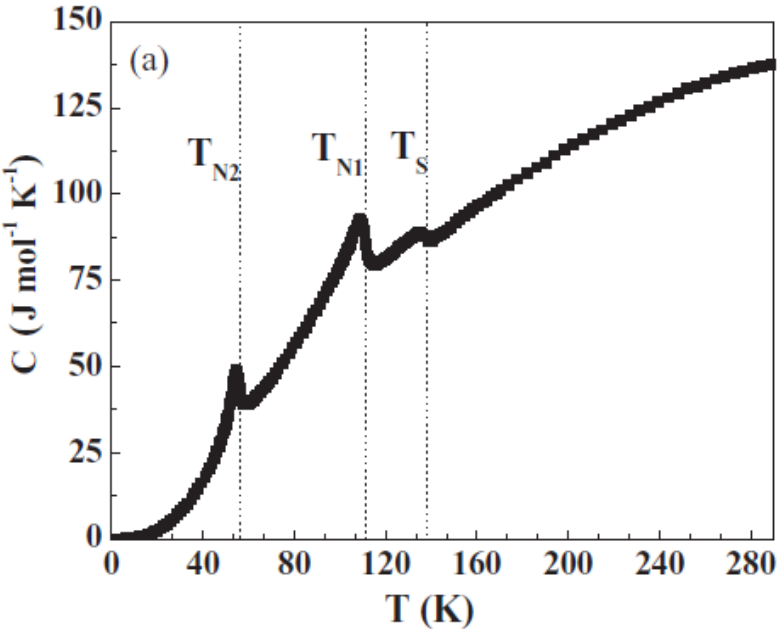


**Figure 1.5** Temperature dependence of the heat capacity in zero field for $Fe_{1.18}V_{1.82}O_4$, with dashed lines marking the three transitions. Adapted from Ref. [6]

The NPD measurements also reveal the ferrimagnetic and noncollinear ferrimagnetic ordering of FVO in its orthorhombic and low temperature tetragonal phases (shown in **Figure 1.6**(c,d)), respectively. The $V^{3+}$ moments are canted and form a two-in-two-out spin structure on the pyrochlore sublattice, as shown in **Figure 1.6**(e).

In its noncollinear ferrimagnetic phase, FVO shows a spontaneous polarization, as reported by Zhang et al.,[6] which makes it ferroelectric at low temperature. The magneto-electric coupling was observed by measuring the polarization as a function of applied magnetic field, as shown in **Figure 1.7**. Zhang et al. suggested that the ferroelectricity originates from the canted $V^{3+}$ moments, which can be explained by the 'spin-current' model. Evidence of the multiferroic FVO were also reported by Takei[15] and Kismarahardja[16] as a magnetocapacitance effect of FVO, as shown in **Figure 1.8**.

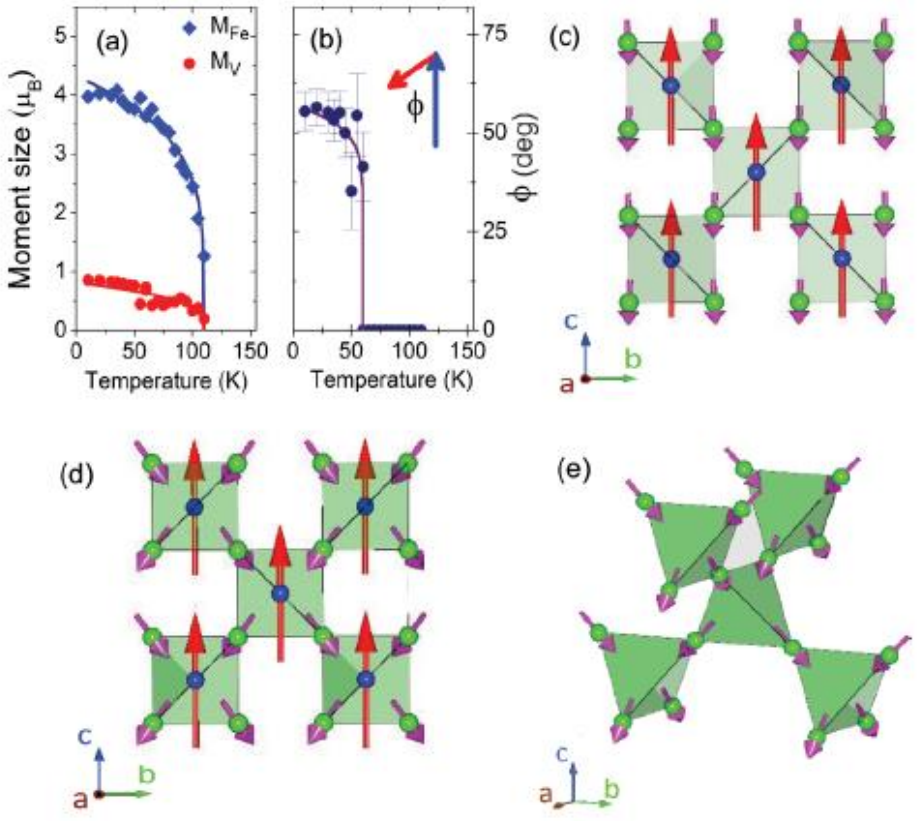


**Figure 1.6** (a) Plot of the ordered moment size on the $Fe^{2+}$ and $V^{3+}$ cation sites and (b) the angle between the $V^{3+}$ moments and the axis defined by $Fe^{2+}$ moments. (c) A sketch of the collinear ferrimagnetic state in the FCO phase, as seen along the cubic (001) direction and (d) a similar sketch of the canted state seen in the LTT phase; (e) A view of $V^{3+}$ moments in a low-temperature ordered state, clearly demonstrating the two-in-two-out spin structure on the pyrochlore sublattice. Adapted from Ref.[4]

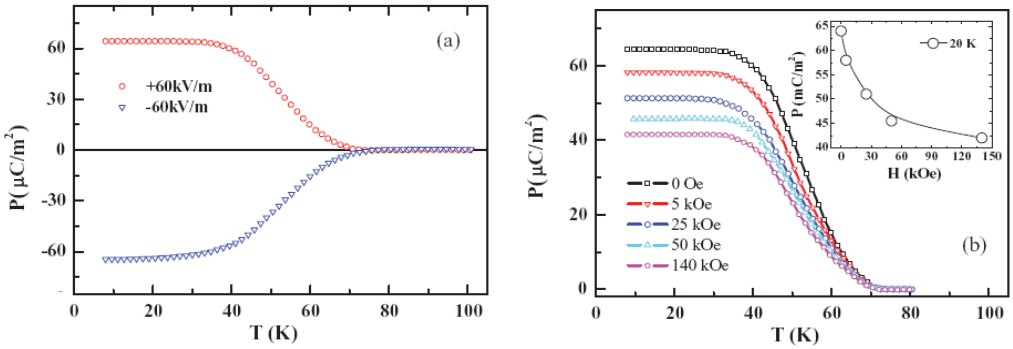


**Figure 1.7** (a) Temperature dependences of the zeroelectric-field polarization in $Fe_{1.18}V_{1.82}O_4$, recorded during warming (5 K/min) after using a static electric poling field of +60 or -60 kV/m. (b) Temperature dependence of the polarization in different magnetic fields on the polarization at T = 20 K. Adapted from Ref.[6]

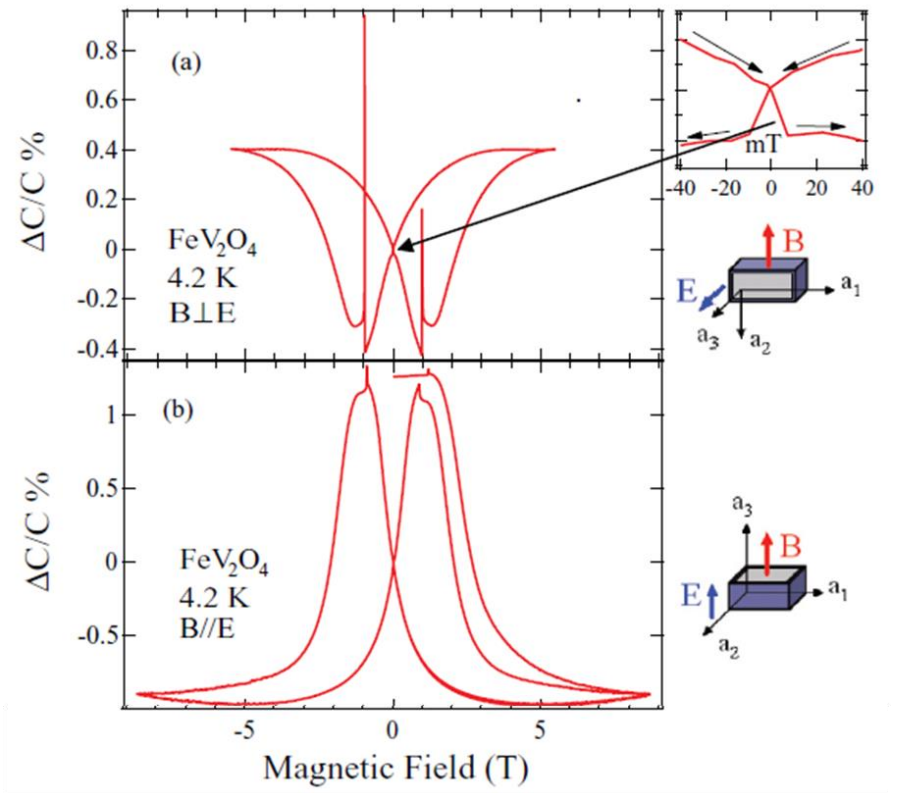


**Figure 1.8** Magnetic field dependent capacitance signal of FVO for $\mathbf{B} \perp \mathbf{E}$ (a) and $\mathbf{B} || \mathbf{E}$ (b) at 4.2 K; Inset in (a): low-field coercive feature $\mathbf{B}_c$ in capacitance signal. Adapted from Ref.[16]

Compared to other non-collinear multiferroic materials, FVO has relatively larger polarization and a higher phase transition temperature. Its intrinsic magnetoelectric coupling has also been reported by many researchers, which opens the way for new design in functional devices. In modern device design, thin film is an important form of material that allows people to further engineer the properties of the device by manipulating defects, strain, interface effect and orientation, among other factors. However, all the reported studies on FVO so far have been based on the study of bulk material, either poly crystalline or single crystal. Successful fabrication of FVO thin films has been a challenge, probably due to the instability of the valence states of $Fe^{2+}$ which tend to form trivalent $Fe^{3+}$,[17] leading to a $Fe_2O_3$ secondary phase.

**Synopsis of Iron Vanadate Thin Film Studies in this Thesis**

In this thesis, the optimum conditions to synthesise chemically phase pure epitaxial FVO film on perovskite $SrTiO_3$ substrate were found by carefully controlling the growth conditions of the FVO film deposition in the pulsed laser deposition (PLD) process. Moreover, the integration of the epitaxial FVO film with a buffer layer ($SrTiO_3$ and $(La,Sr)MnO_3$) which can act as the bottom electrode in the following property measurements, is achieved. The valence states of iron and vanadium ions were probed by X-ray absorption spectrum (XAS) which shows mainly divalent $Fe^{2+}$ and trivalent $V^{3+}$ states, while a small amount of $Fe^{3+}$ was also found, which may substitute for the $V^{3+}$ in the octahedral site. The local magnetic moments arrangement of the FVO film was measured by X-ray magnetic circular dichroism (XMCD), showing that $Fe^{2+}$ and $V^{3+}$ moments are antiparallel to each other and are strongly coupled, while $Fe^{3+}$ ions which are detected by XAS make very little contribution to the magnetization of the sample. The $\mathbf{M}$-$\mathbf{H}$ loops acquired by the magnetic properties measurement system (MPMS) show a clear magnetic anisotropy, such that the magnetization of out-of-plane is much larger than that of in-plane associated with a larger coercive field as well. A small magnetization jump in the out-of-plane $\mathbf{M}$-$\mathbf{H}$ loops also reveals a phase fraction in the system which is a soft magnet (called phase 'B' in this thesis). It is very likely that this soft magnet phase is formed by the excess $Fe^{3+}$ in the system, possibly in the form of $Fe^{2+}(Fe^{3+}_xV^{3+}_{(2-x)})O_4$. Magnetic force microscopy (MFM) was employed to imaging the magnetic domains of the FVO films. The domain switching, which was achieved by an applied magnetic field, was captured by MFM. The electrical properties of the FVO films were tested on a Pd/FVO/Nb:STO sample where Pd and Nb doped STO were used as top and bottom electrodes. Using a dynamic pyroelectric effect measuring method, the pyroelectric effect of the sample was observed, indicating the asymmetric charge structure and polarization of the sample. The polarization was estimated by the integration of the pyroelectric current. The dielectric property was observed by measuring the capacitance and $tan\delta$ of the sample as a function of temperature and frequency. By simulating the data with a 2 $\mathrm{RC}$ elements model, we found that, at temperatures higher than 40 K,

the capacitance is dominated by an extrinsic Maxwell-Wagner relaxation, which is induced from the Schottky barrier at the interface between FVO and Nb:STO, while the intrinsic relaxation is in dominant at a temperature regime lower than 40 K. The magneticelectric coupling of the FVO film was observed by measuring the capacitance of the sample as a function of applied magnetic field. However, a clear hysteresis loop is acquired only when the magnetic field is parallel to the electric field. This anisotropy of the magnetocapacitance effect is similar to that of the magnetic jump in the OOP **M**-**H** loop which corresponds to the phase 'B'.

## 1.4 Cobalt Chromite

Not long after Katsura[18] and Tokura[19] had theoretically predicted a model of a new type of multiferroics, with canted spiral magnetic ordering based on the spin current model, Yamasaki[20] reported the direct observation of magnetoelectric coupling in a multiferroic spinel, cobalt chromite, $CoCr_2O_4$ (CCO), which had exactly the same magnetic arrangement as Tokura had proposed.

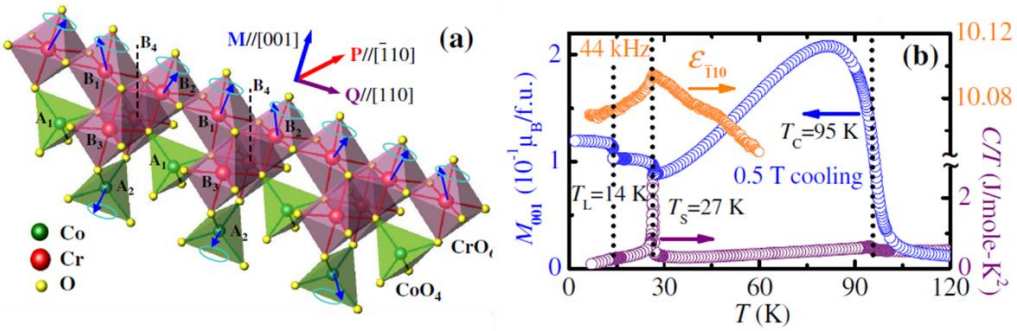


**Figure 1.9** (a) Crystallographic and low-T magnetic structure of spinel CCO. (b) T dependence of magnetization, **M**, specific heat divided by temperature and dielectric constant. The existence of three phase transitions is evident, and $T_C$, $T_S$, and $T_L$ denote temperatures for ferrimagnetic transition, conical spin ordering, and lock-in transition, respectively. Adapted from Ref.[21]

The structure of CCO is shown in **Figure 1.9**(a). Oxygen atoms in spinel have a cubic close-packed structure, $Co^{2+}$ and $Cr^{3+}$, with cations located in the interstitial sites in the ratio of 1:2, in such a way that the $Co^{2+}$ cations are coordinated in a tetrahedral manner, and the $Cr^{3+}$ cations show an octahedral coordination. **Figure 1.9**(b) shows the temperature dependence of the physical properties of CCO,[21]

indicating that the compound undergoes three phase transitions at low temperature. At $T_c$ = ~ 95 K, it transfers from a paramagnetic to ferrimagnetic; at $T_s$ = ~27 K, the compound transfers from ferrimagnetic to a conical spin configuration; and at $T_L$ = 14 K, a lock-in transition occurs. Choi [21] reported a reversing of the polarization at $T_L$ due to the sign change of the spin wave $\boldsymbol{Q}$ at the lock-in transfer temperature, as shown in **Figure 1.10**.

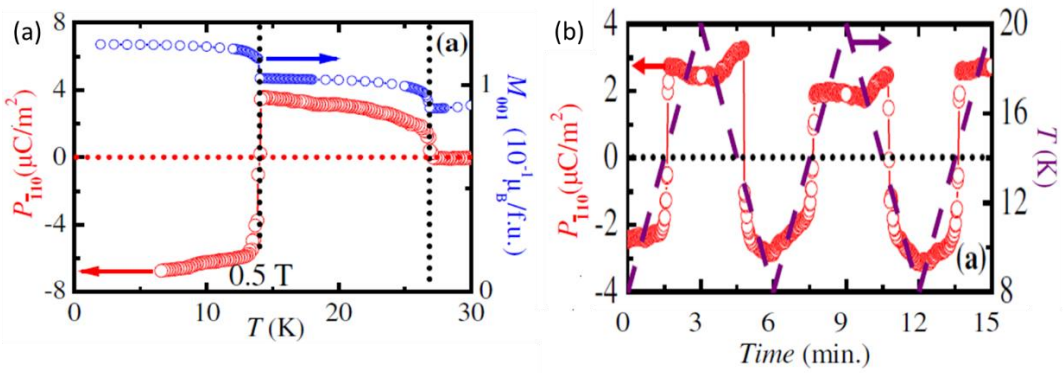


**Figure 1.10** (a) Temperature dependence of polarization and magnetization of CCO. (b) Temperature reversal of polarization in CCO. Adapted from Ref.[21]

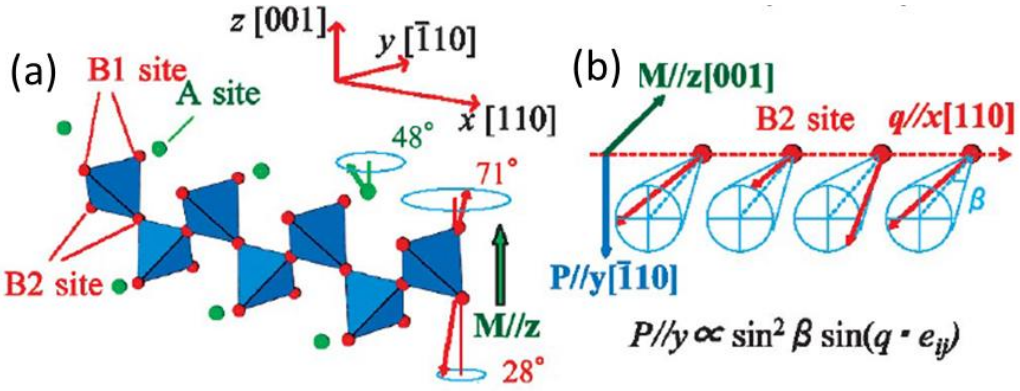


**Figure 1.11** (a) The structure viewed along the conical spin modulation direction [110] (denoted as the x axis). The circles with slanted arrows indicate the spiral plane of the respective spins with conical structure. Adapted from Ref.[22] (b) The relation among the net magnetization $\boldsymbol{M}$, the spiral spin modulation vector $\boldsymbol{q}$, and the induced polarization $\boldsymbol{P}$, as represented for the case of the B2-site chain in CCO .Adapted from Ref.[20]

The most exciting finding of CCO as a multiferroic material is the strong coupling between polarization and magnetization, and the special relationship between the magnetization $\boldsymbol{M}$ and polarization $\boldsymbol{P}$ is shown in **Figure 1.11**. As shown in **Figure 1.11**(a), the polarization only appears at temperatures lower than 27 K, in

its conical spiral phase, indicating the magnetic origin of polarization, but since the coupling is intrinsic, it is very strong. As shown in **Figure 1.12**(c), the polarization reverses instantly as the magnetic field reverses. This demonstrates the ferroelectricity induced in non-collinear magnetics, and opens the potential for creating new types of functional materials. However, there are two distinct weaknesses of CCO as a candidate for multiferroic applications; a) the magnitude of polarization (~2μC/m$^2$) is smaller by 5 orders than that of the prototypical ferroelectrics $BaTiO_3$, and b) the phase transition temperature (~25 K) is too low for realistic applications.

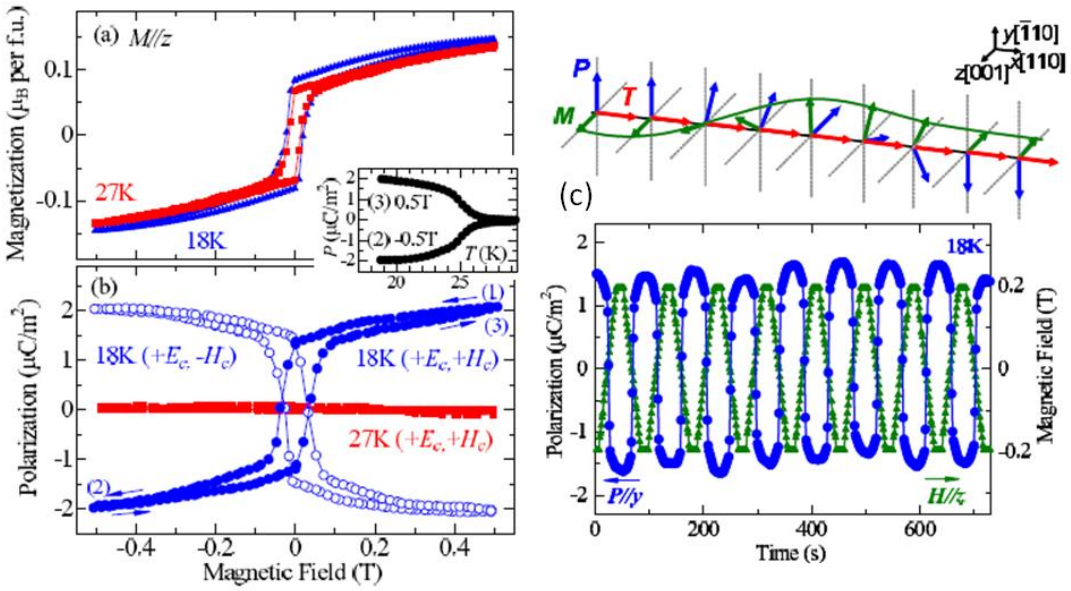


**Figure 1.12** Magnetic-field dependence of (a) magnetization and (b) electric polarization at temperatures above (27 K) and below (18 K) with the ferroelectric transition temperature ($T_S$ = 25 K). For measurements of the polarization (b), the magnetic field was scanned between +$H_c$ and -$H_c$, for each *ME* cooled state prepared with (+ $E_c$;+$H_c$) and (+$E_c$; -$H_c$), as represented by solid and open circles. Here, $E_c$(= 400 kV/m) and $H_c$(= 0.5 T), which stand for the cooling electric and magnetic fields, respectively. The inset shows the temperature dependence of the polarization ($\boldsymbol{P}$) in the warming runs, starting from the magnetic-field scan points (2) and (3) shown in (b). (c) The synchronized reversal of the polarization ($\boldsymbol{P}$ || $y$, solid circles) at 18 K with change of the external magnetic field ($\boldsymbol{H}$ || $z$) which periodically reverses the magnetization direction ($\boldsymbol{M}$ || $z$). The upper panel depicts the plausible clamping process of the ferromagnetic and polarization domain walls. Note that every toroidal moment, defined as $\boldsymbol{T} \propto \boldsymbol{P} \times \boldsymbol{M}$, is kept intact across the domain wall. Adapted from Ref.[20]

**Synopsis of Cobalt Chromite Thin Film Studies in this Thesis**

In this thesis, CCO thin films were synthesised on perovskite STO substrate with a $La_{0.67}Sr_{0.33}MnO_3$ (LMSO) buffer layer in between. Interestingly, the film shows a piezoresponse when probed by a piezoresponse force microscope (PFM) at room temperature, in the temperature regime at which that CCO is not expected to have ferroelectricity. Further measurements were carried out to clarify the origin of the piezoresponse in the samples, and the conclusion is that the piezoresponse is related to dipoles induced by ionic motion under an external electric field. The CCO/LSMO heterostructure also shows an interesting resistivity switching behaviour when a bias is applied. A model is proposed; that the switching behaviour is derived from the migration of oxygen vacancies in the LSMO layer close to the interface, which is pushed in to the CCO layer when bias is applied and induces the change in total resistivity of the heterostructure.

References

[1] S. Kawaguchi, H. Ishibashi, S. Nishihara, M. Miyagawa, K. Inoue, S. Mori, Y. Kubota,Anomalous magnetization behaviour in a single crystal of vanadium spinel FeV2O4, J Phys-Condens Mat 2013, 25.
[2] U. Luders, A. Barthelemy, M. Bibes, K. Bouzehouane, S. Fusil, E. Jacquet, J. P. Contour, J. F. Bobo, J. Fontcuberta, A. Fert,NiFe2O4: A versatile spinel material brings new opportunities for spintronics, Adv. Mater. 2006, 18, 131733.
[3] H. Tsunetsugu, Y. Motome,Magnetic transition and orbital degrees of freedom in vanadium spinels, Phys. Rev. B 2003, 68.
[4] G. J. MacDougall, V. O. Garlea, A. A. Aczel, H. D. Zhou, S. E. Nagler,Magnetic order and ice rules in the multiferroic spinel FeV2O4, Phys. Rev. B 2012, 86, 060414.
[5] S. Sarkar, T. Saha-Dasgupta,Orbital ordering in FeV2O4: Spinel with two orbitally active sites, Phys. Rev. B 2011, 84, 235112.
[6] Q. Zhang, K. Singh, F. Guillou, C. Simon, Y. Breard, V. Caignaert, V. Hardy,Ordering process and ferroelectricity in a spinel derived from FeV2O4, Phys. Rev. B 2012, 85, 054405.
[7] R. Takahashi, H. Misumi, M. Lippmaa,Pyroelectric detection of spontaneous polarization in magnetite thin films, Phys. Rev. B 2012, 86, 144105.
[8] J. S. Kang, J. Hwang, D. H. Kim, E. Lee, W. C. Kim, C. S. Kim, H. K. Lee, J. Y. Kim, S. W. Han, S. C. Hong, B. Kim, B. I. Min,Soft x-ray magnetic circular dichroism study of valence and spin states in FeT2O4 (T = V, Cr) spinel oxides, J. Appl. Phys. 2013, 113, 17E116.
[9] T. Kimura, Y. Sekio, H. Nakamura, T. Siegrist, A. P. Ramirez,Cupric oxide as an induced-multiferroic with high Tc, Nature Mater. 2008, 7, 291.
[10] T. Kimura,Spiral Magnets as Magnetoelectrics, Annu. Rev. of Mater. Res. 2007, 37, 387.
[11] S. W. Cheong, M. Mostovoy,Multiferroics: a magnetic twist for ferroelectricity, Nature Mater. 2007, 6, 13.
[12] Y. Yamasaki, S. Miyasaka, Y. Kaneko, J. P. He, T. Arima, Y. Tokura,Magnetic reversal of the ferroelectric polarization in a multiferroic spinel oxide, Phys. Rev. Lett. 2006, 96.
[13] K. E. Sickafus, J. M. Wills, N. W. Grimes,Structure of spinel, J. A. Ceram. Soc. 1999, 82, 3279.
[14] T. Katsufuji, T. Suzuki, H. Takei, M. Shingu, K. Kato, K. Osaka, M. Takata, H. Sagayama, T. H. Arima,Structural and magnetic properties of spinel FeV2O4 with two ions having orbital degrees of freedom, J Phys Soc Jpn 2008, 77.
[15] H. Takei, T. Suzuki, T. Katsufuji,Nonvolatile memory effect of capacitance in polycrystalline spinel vanadate, Appl Phys Lett 2007, 91.
[16] A. Kismarahardja, J. S. Brooks, H. D. Zhou, E. S. Choi, K. Matsubayashi, Y. Uwatoko,Dielectric properties of single crystal spinels in the series FeV2O4, MnV2O4, and CoV2O4 in high magnetic fields, Phys Rev B 2013, 87.
[17] P. P. Stander, C. P. J. Vanvuuren,The High-Temperature Oxidation of FeV2O4, Thermochim Acta 1990, 157, 347.
[18] H. Katsura, N. Nagaosa, A. V. Balatsky,Spin current and magnetoelectric effect in noncollinear magnets, Phys Rev Lett 2005, 95.
[19] Y. Tokura,Materials science - Multiferroics as quantum electromagnets, Science 2006, 312, 1481.
[20] Y. Yamasaki, S. Miyasaka, Y. Kaneko, J. P. He, T. Arima, Y. Tokura,Magnetic reversal of the ferroelectric polarization in a multiferroic spinel oxide, Phys Rev Lett 2006, 96.

[21] Y. J. Choi, J. Okamoto, D. J. Huang, K. S. Chao, H. J. Lin, C. T. Chen, M. van Veenendaal, T. A. Kaplan, S. W. Cheong,Thermally or Magnetically Induced Polarization Reversal in the Multiferroic CoCr2O4, Phys Rev Lett 2009, 102.
[22] K. Tomiyasu, J. Fukunaga, H. Suzuki,Magnetic short-range order and reentrant-spin-glass-like behavior in CoCr2O4 and MnCr2O4 by means of neutron scattering and magnetization measurements, Phys Rev B 2004, 70.

# CHAPTER TWO

# 2 THEORETICAL BACKGROUND & EXPERIMENTAL METHODS

## 2.1 Introduction

In last chapter, the structure of the spinel oxides ($FeV_2O_4$ and CCO), which were studied in this research, as well as their properties related to this thesis were introduced.

In the first half of this chapter, some basic concepts, which are important to the research, and the theories and models used to analyse the acquired data in the following chapters are explained. This starts with introducing the concepts of ferromagnetic and ferroelectric ordering and their origins. The combination of the two orderings, multiferroicity, is introduced. The origin of ferroelectricity in non-collinear magnetics is explained by the 'spin current' model.[1] Some general dielectric theories, such as the Debye model and the Cole-Cole model, are introduced, as the dielectric properties of FVO thin films, which are investigated in the following chapters, require those models for analysis.

In the second half of this chapter, synthesis and characterization methods are introduced including: Pulsed laser deposition, X-ray diffraction, the X-ray absorption spectrum, and X-ray magnetic circular dichroism, among others.

## 2.2 Theoretical Background

### 2.2.1 Ferromagnet

A ferromagnetic material has a spontaneous magnetic moment[2]-a magnetic moment even in the absence of an applied magnetic field, which is due to the alignment of the magnetic moments located on an atomic lattice[3](as shown in **Figure 2.1**(a)). Cooling from a temperature above a critical temperature known as the Curie point $T_C$, a ferromagnetic material undergoes a phase transition from a high-temperature phase, that has no macroscopic magnetic moment, to a low-temperature phase that has a magnetic moment.

#### 2.2.1.1 Hysteresis Loop

A ferromagnet is usually associated with a phenomenon known as hysteresis which was first studied and named by James Ewing in 1881.[3]

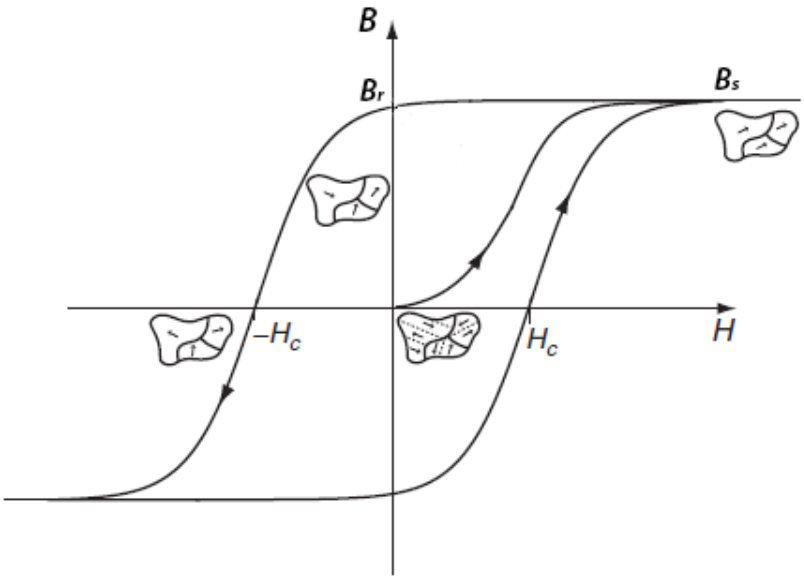


**Figure 2.1** The hysteresis loop of a ferromagnet.

The hysteresis loop is shown in **Figure 2.1**. The ferromagnetic material is initially in an unmagnetized state, as a result of the influence of domains with different magnetization directions. When the imposing magnetic field $\boldsymbol{H}$ is applied, magnetization appears, modifies and eventually reorientates and aligns the directions of the magnetized ferromagnetic domains, resulting in the saturation

induction $\boldsymbol{B_s}$. As the applied magnetic field is restored to zero, induction reduces to $\boldsymbol{B_r}$. To reduce the magnetization to zero, a reverse magnetic field of $\boldsymbol{H_c}$, known as a coercive field, is needed as marked on the loop.

The ferromagnetic materials can be divided into two categories, depending on their characteristics as shown on the hysteresis loops. Material with high saturation induction $\boldsymbol{B_s}$, and low coercivity $\boldsymbol{H_c}$, can be easily magnetized and demagnetized. Such materials are known as soft magnetic materials, and are suitable for transformer and inductor cores and recording heads, whereas materials possessing a square-shaped loop, known as hard magnetic materials, can be used as permanent magnets and recording media due to their stable magnetization states.

#### 2.2.1.2 Antiferromagnet and Ferrimagnet

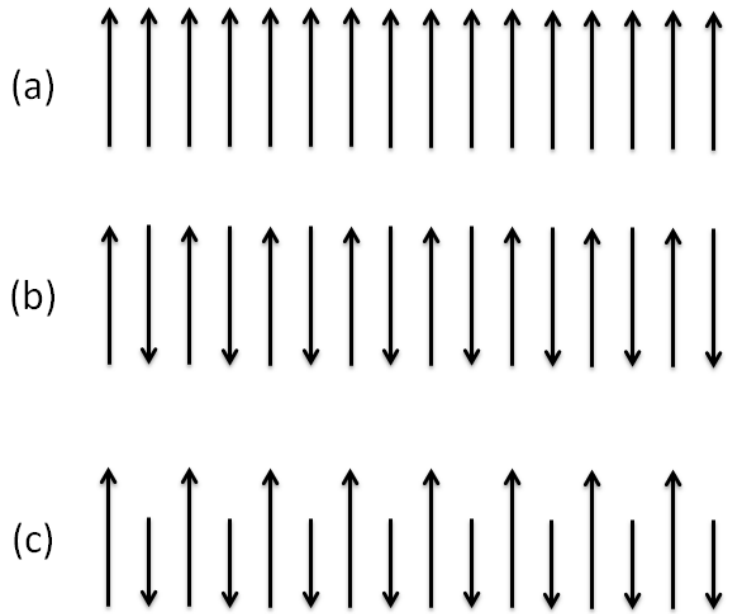


**Figure 2.2** Magnetic orders. (a)Ferromagnetic; (b)Antiferromagnetic; (c)Ferrimagnetic.

Materials display other types of magnetic orders as well as ferromagnetism namely antiferromagnetic and ferrimagnetic. In antiferromagnetic material, the crystal lattice is divided into more than one sub-lattice whose magnetizations are cancelled out by each other and show a zero macro magnetization (as shown in **Figure 2.2**(b)). Similar to the Curie point $T_c$ of ferromagnetic materials, an

antiferromagnet undergoes an antiferromagnetic ordering transition at Néel point $T_N$, cooling from a higher temperature, showing a small peak in the magnetization as well as a heat anomaly. Because antiferromagnets have no macro magnetization, they have no wide application in current magnetic technologies. In a ferrimagnet, the magnetizations of sub-lattices are unequal and cannot be cancelled out (as shown in **Figure 2.2**(c)). Like ferromagnets, a net macro magnetic moment is observed in ferrimagnets, which leads to a wide range of applications for this kind of material.

#### 2.2.1.3 Origin of Ferromagnetism

Ferromagnetism originates from the quantum mechanical exchange interaction between component atoms.[4] The mechanism of ferromagnetism of materials can be successfully explained by two theories: (1) the Curie-Weiss localized-moment theory[5] and (2) the Stoner band theory.[6] In the Curie-Weiss theory, the orientation of the magnetic moment is governed by the internal "molecular field" (also known as the "exchange field") and is opposed by thermal agitation.[5] Below a critical temperature (known as the Curie temperature $T_c$), the internal "molecular-field" of ferromagnetic materials becomes stronger than the thermal agitation. Thus, spin order (alignment of magnetic moments) occurs even in the absence of an applied magnetic field.

Although Weiss' theory successfully explained ferromagnetic behaviours, for example, a sharp upsurge of susceptibility at $T_c$ in ferromagnetic materials, it failed to explain the measured values of the magnetic moments per atom in several ferromagnetic materials.[4] According to the Stoner theory, the concept of band theory was introduced, where the driving force of magnetic properties of materials is the exchange of energy which is induced by the change in band energy.[6] In the ferromagnetic system, the energy is decreased by the parallel aligned spins, while oppositely aligned spins increase the energy. In both Weiss and Stoner models, tightly bound, localized electrons such as d-electrons of transition metals or f-electrons of rare-earth ions, are critical for magnetism.[4]

## 2.2.2 Ferroelectrics

Ferroelectrics are a group of materials that possess spontaneous electric polarization, which can be easily reversed by an application of an external electric field of some magnitude less than the dielectric breakdown of the material itself.[7] Thus, the two necessary conditions to classify a material as ferroelectric are (a) the existence of spontaneous polarization and (b) a demonstrated re-orienting of the polarization. Many properties analogous to those of ferromagnets, such as phase transaction at Curie temperature $T_c$, domains and hysteresis loops, can be found in ferroelectric materials. As ferroelectric materials have a large polarization in a low operating electric field, they have been widely applied for data storage and as capacitors for such purposes as ferroelectric dynamic random access memory (FE-DRAM).[8]

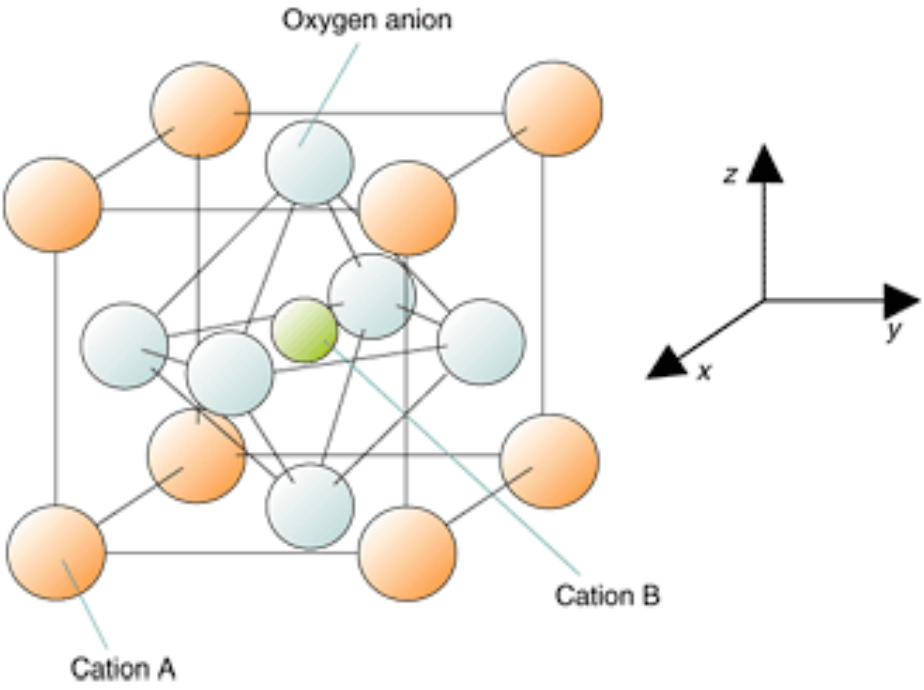


**Figure 2.3** Cubic $ABO_3$ perovskite-structure. The large cations sit at the cube corner positions, the small B cation sits at the centre of an octahedron of oxygen anions.

### 2.2.2.1 Perovskite Ferroelectrics

Ferroelectricity was first observed in Rochelle salts ($KNa(C_4H_4O_6)\cdot 4H_2O$) in 1921,[9] followed by the discovery of ferroelectricities in $KH_2PO_4$ in 1935 and $BaTiO_3$ in 1945. With the discovery of ferroelectricity in $BaTiO_3$, extensive studies

on the topic[10-11] led to a fundamental understanding of this subject. $BaTiO_3$ is an $ABO_3$ perovskite-structure oxide which is the most widely studied and used ferroelectric material today. The structure of perovskite oxide is shown in **Figure 2.3**. In a cubic perovskite structure, the type 'A' atom sits at cube corner positions, the type 'B' atom sits at the body centre position and oxygen atoms sit at face centred positions. The studies of ferroelectric perovskite offered an avenue to more theoretical studies, which in turn led to a thorough fundamental understanding of ferroelectricity, because of its simple structure and the small number of atoms per unit cell.

### 2.2.2.2 Origin of Ferroelectricity

It is well understood today that the spontaneous polarization of perovskite mostly arises from the electric dipole moments created by the off-centred shift of the B site cations. As shown in **Figure 2.4**, the shift of B site cations along two <111> directions can lower its energy below $T_c$. Above $T_c$, the spontaneous polarization disappears as the B site cations stabilize at non-polarization positions.

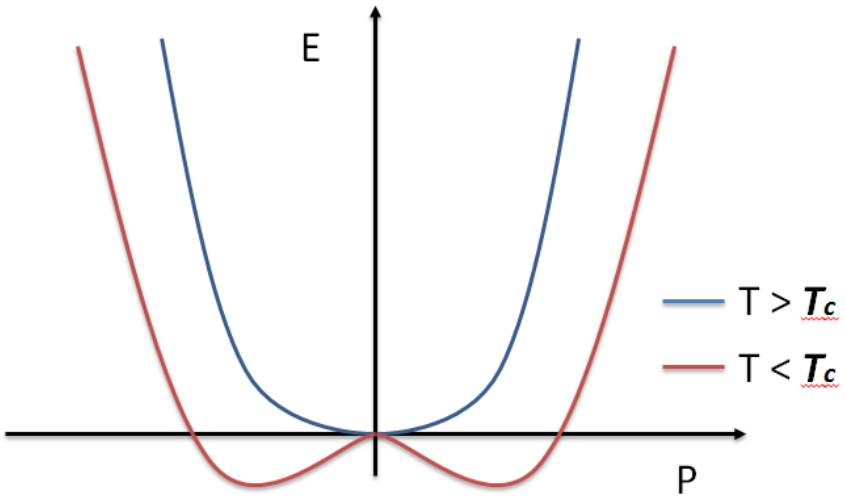


**Figure 2.4** Free energy versus polarization.

The distortion of the lattice caused by the shift of point charges destabilizes the lattice owing to short-range repulsion, but the additional bonding effects might stabilize the lattice. At high temperature, the short-range repulsion dominates and leads to a symmetric structure, the paraelectric state of a

ferroelectric material.[12-13] In 1992, in order to get a better understanding of the origin of perovskite ferroelectricity, Cohen, R. E. and H. Krakauer[13] investigated the ferroelectric properties of $BaTiO_3$ and $PbTiO_3$ by employing density functional theory. They found that the differences in ferroelectric behaviour between $PbTiO_3$ and $BaTiO_3$ come from the different electronic configurations. In both cases, hybridization of the Ti *3d* states with O *2p* is essential for the ferroelectric instability. In $PbTiO_3$, the hybridization between A site $Pb^{2+}$ cations leads to a larger polarizing ability, while $Ba^{2+}$ in $BaTiO_3$ has an ionic interaction with O.

## 2.2.3 Multiferroics

Multiferroics are understood as materials that simultaneously present more than one of the 'ferroic properties' in the same phase.[14] The term 'ferroic properties' primarily indicates ferroelectricity, ferromagnetism and ferroelasticity. In recent years, the term 'multiferroics' tends to include ferrotoroidic and antiferroic orders as well. The most fascinating feature of multiferroics is their magnetoelectric coupling, which offers the potential to manipulate the polarization by external magnetic fields and vice versa[15]. The relationship and interactions between multiferroics are shown in **Figure 2.5**(a) and (b) respectively. The properties of multiferroics lead to a promising avenue for new functional devices, such as data storage devices which can read and write the magnetization states by electric field.

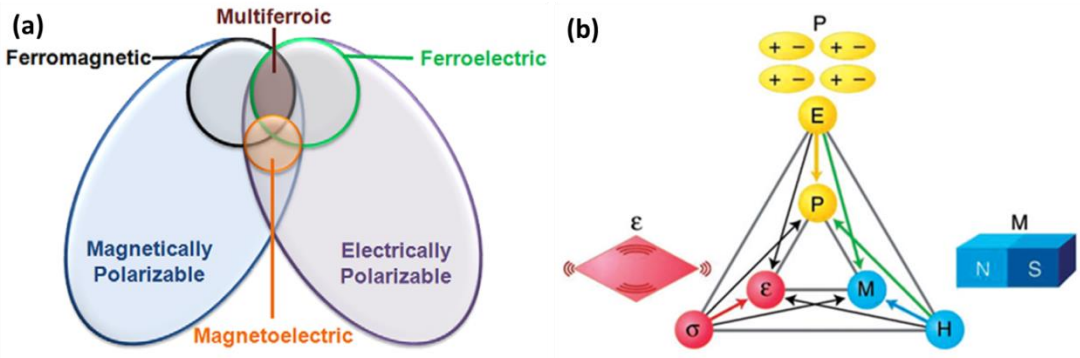


**Figure 2.5** (a) Relationship of multiferroics. Adapted from Ref.[16] (b) The interaction between multiferroics. Adapted from Ref.[17] The coupling of magnetic and electric orders has drawn much attention in recent years.

### 2.2.3.1 'Proper' and 'Improper' Multiferroics

Materials such as $BiFeO_3$ (BFO), whose ferroelectric and magnetic orders are associated with different ions, are known as 'proper' ferroelectrics. The spontaneous polarization is the primary order parameter. In such materials, the temperature scale for ferroelectric order is usually much larger than for the scale of magnetic order. For example, the ferroelectric transition temperature $T_{FE}$ of $BiMnO_3$ is ~ 800 K while the ferromagnetic transition $T_{FM}$ is ~ 110 K[18]. The coupling between magnetism and ferroelectricity is weak for these two orders because of they are originated from different ions, and it is this feature of 'proper' multiferroics which prevents them from being useful.

| | Mechanism of inversion symmetry breaking | Materials |
|---|---|---|
| Proper | Covalent bonding between $3d^0$ transition metal (Ti) and oxygen | $BaTiO_3$ |
| | Polarization of $6s^2$ long pair of Bi or Pb | $BiMnO_3$, $BiFeO_3$, $Pb(Fe_{2/3}W_{1/3})O_3$ |
| Improper | Structural transition<br>'Geometric ferroelectrics' | $K_2SeO_4$, $Cs_2CdI_4$, hexagonal $RMnO_3$ |
| | Charge ordering<br>'Electronic ferroelectrics' | $LuFe_2O_4$ |
| | Magnetic ordering<br>'Magnetic ferroelectrics' | Orthorhombic $RMnO_3$, $RMn_2O_5$, $CoCr_2O_4$ |

**Table 2.1** Classification of ferroelectrics. Adapted from Ref.[19]

In recent years, 'improper'[20] ferroelectrics, in which polarization is just a part or a by-product of a more complex lattice distortion, have drawn significant attention. As shown in **Table 2.1**, 'improper' multiferroics can be divided into three categories: (a) Geometric ferroelectrics, (b) Electronic ferroelectrics and (c) Magnetic ferroelectrics. One example of geometric ferroelectrics are hexagonal manganites $RMnO_3$, in which R stands for rear earth elements. The ferroelectricity of $RMnO_3$ stems from electric dipole moments induced by a nonlinear coupling to nonpolar lattice distortions.[21] Such lattice distortions can be R-O planes buckling or manganese-oxygen bipyramid tilts[22]. $LuFe_2O_4$ is an example of 'electronic

ferroelectrics'. As it crystallizes in a bilayer structure, the valence of Fe cations in each layer is different. Ratios of 1:2 and 2:1 are created with $Fe^{2+}$:$Fe^{3+}$ below ~ 350 K and induce a net polarization.[23] Another type of 'improper' ferroelectrics is 'magnetic ferroelectrics' in which the electric dipoles are induced by magnetic orders. In fact, this group of materials are the most promising candidates for multiferroics applications, as the polarization is quite tuneable with the applied external magnetic fields.

#### 2.2.3.2 Perovskite Multiferroics

Attempts to combine magnetic and ferroelectric properties in one material started in the 1960s when Landau[24] proposed his theory of the possibility of the coupling between magnetic and electric degrees of freedom. As discussed in the last two chapters, magnetism and ferroelectricity require different filling of the *d* shells, and this feature leads to a mutual exclusivity between these two ordered states.[12] However, researchers still found that some compounds possessed both magnetism and ferroelectricity. Amongst them, one particular material, namely $BiFeO_3$(BFO), has experienced enormous attention in the last decade,[25] when it was shown that it had both an unexpectedly large remnant polarization and very large magnetism. The perovskite $BiFeO_3$ was first found in the 1950s,[26] and its detailed structure of monodomain crystal was characterized by Kubel and Schmid in 1990.[27] The structure of BFO is shown in **Figure 2.6**(a-c). Two distorted perovskite blocks connect to each other along the body diagonal <111>, and build a rhombohedral unit cell. The oxygen octahedral in two perovskite blocks are connected along the <111>, and rotate clockwise and counter-clockwise around the <111> by a degree of ±13.8 °. The Fe-ion is shifted by 0.135 Å along the same axis away from the oxygen octahedron central position.

The magnetic properties of BFO were studied in detail in the 1980s. It was reported that BFO is a G-type antiferromagnet with a small rotating helical magnetic ordering of a ~620 Å rotation period.[28] The Néel temperature $T_N$ of BFO is 673 K.[29] Like other perovskite-type ferroelectrics, the magnetism comes from the B-site transition metal cation $Fe^{3+}$, while the polarization is mostly caused by

the A-site $Bi^{3+}$ long pair with 2 electrons on the *6s* orbital, which moves away from the centro-symmetric position in the surrounding oxygen octahedral.

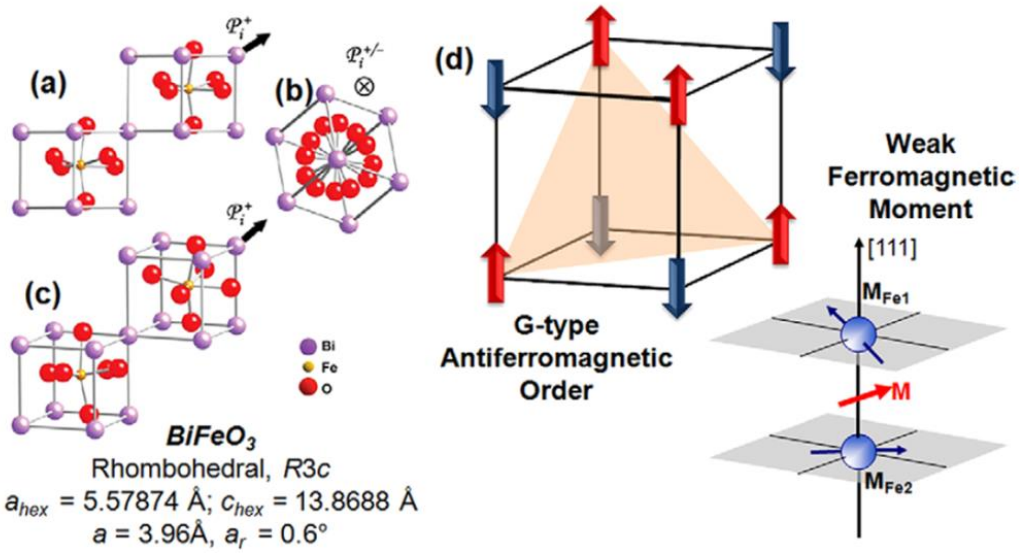


**Figure 2.6** (a-c) Structure of BFO shown looking down the [110], [111] and general 3D view. (d) The magnetic structure of BFO. Adapted from Ref.[30]

## 2.2.4 Ferroelectricity Induced by Magnetic Spirals

The polarization in cycloidal spiral structures was first predicted by Katsura et al.,[31] and a microscopic mechanism was also proposed. They considered that the ferroelectricity is generated by the spin current which is induced by the non-collinearly coupled spins. Sergienko and Dagotto[32] argued that the generation mechanism of ferroelectricity is an inversed effect of the Dzyaloshinskii-Moriya (D-M) interaction[33-34] where the non-collinearly coupled magnetic moments polarize the oxygen through the electron-lattice interaction. The relationships among non-collinear magnetic moments, displacements of oxygen and electric polarization are shown in **Figure 2.7**. In the configuration of cycloidal spiral magnetics, the direction of local electric polarization is uniform and the total electric polarization is finite. As shown in **Figure 2.7**(a,b), the sign of the polarization vector can be switched by reversing the spin helicity (shift between CW and CCW). In the case of canted antiferromagnetics, though, the D-M effect may induce local

polarization, such that the directions of the polarization are different and are cancelled out by each other macroscopically.

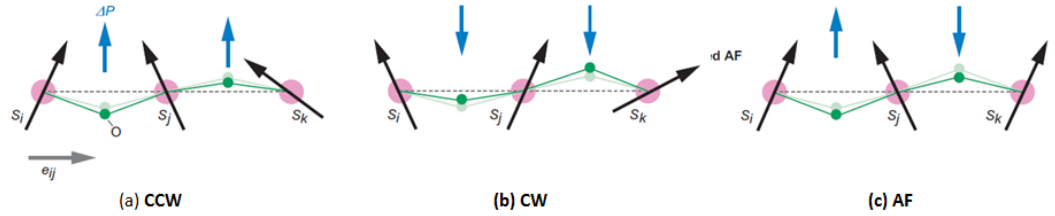


**Figure 2.7** Local electric polarization induced by spin canting (a) CCW cycloidal spiral, (b) CW cycloidal spiral and (c) AF structures. Adapted from Ref.[35]

The theoretical model of the relation between polarization $\boldsymbol{P}$ and magnetic moments can be described by Eq.2.1.

$$P \propto \gamma e_{ij} \times (S_i \times S_j) \tag{2.1}$$

Here, $\gamma$ is the proportional constant determined by the super-exchange interactions and spin-orbit coupling, $e_{ij}$ is parallel to the propagation vector and ($S_i \times S_j$) is parallel to the spin rotation axis. The equation indicates that when the propagation vector is not parallel to the spin rotation axis (as shown in **Figure 2.8**(c-e)) a polarization can occur. On the other hand, no local polarization is induced in the scenario that $S_i \| S_j$(($S_i \times S_j$)=0 as shown in **Figure 2.8**(a)) or $e_{ij} \| (S_i \times S_j)$(as shown in **Figure 2.8**(b)).

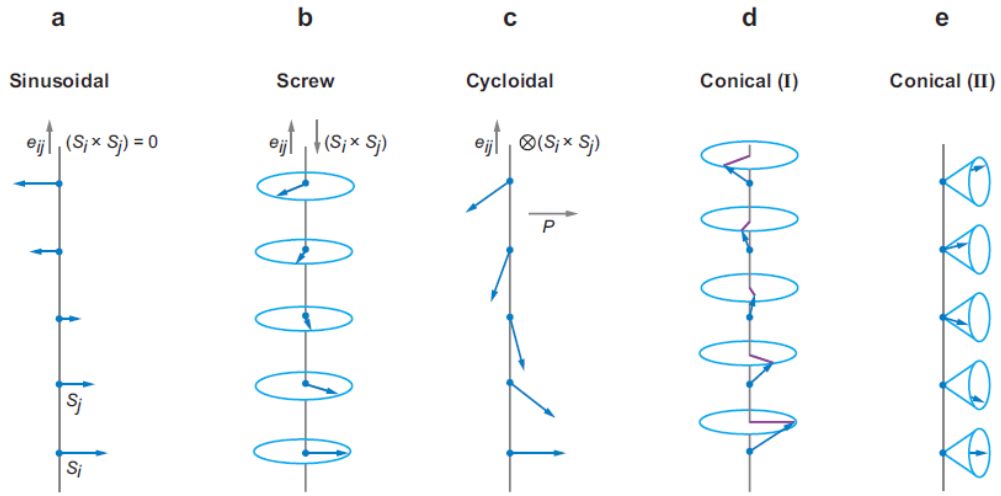


**Figure 2.8** Spiral Configurations (a) Sinusoidal, (b) Screw, (c) Cycloidal, (d) Conical (I) and (e) Conical (II).

### 2.2.5 General Dielectric Theories

In order to investigate the electric properties of FVO thin films, the dielectric properties of a Pd/FVO/Nb:STO junction is systematically measured and analysed later in this thesis. To have a better understanding of the results, the basic dielectric theories are introduced here.

#### 2.2.5.1 Complex Dielectric Permittivity

Insulators are materials which have a forbidden gap, usually larger than 5 eV, between their valence and conduction energy bands. If an insulator is placed between two conducting plates with a voltage source $V$ connected, it will store electrical charges *Q*. This phenomenon was called *dielectrics* by Michael Faraday in 1937. The charge stored in the material can be expressed as

$$Q = CV\,, \tag{2.2}$$

where $C$ is the capacitance, given as

$$\mathrm{C} = \varepsilon_r \varepsilon_0 \frac{A}{d}\,, \tag{2.3}$$

where $\varepsilon_r$ is the relative permittivity, $\varepsilon_0$ is the permittivity of a vacuum (with a value of $8.85\times10^{-12}$ F/m), $A$ is the area of the electrodes and $d$ is the distance between the electrodes. $\varepsilon_r$ is also called the relative dielectric constant and written as $\varepsilon'$.

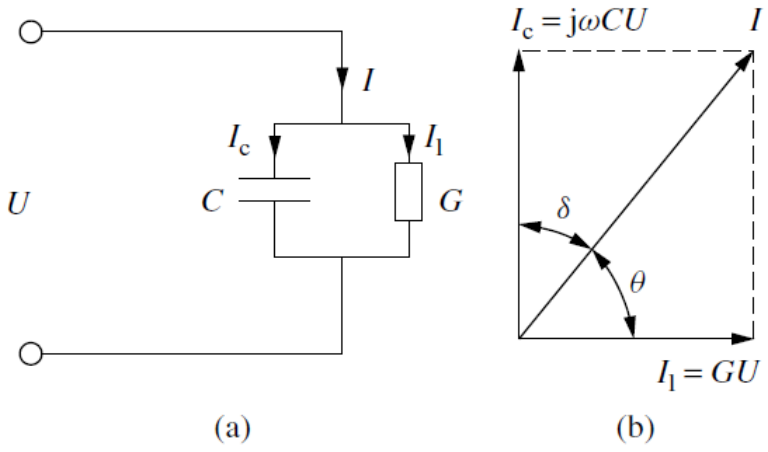


**Figure 2.9** The relationships between charging current and loss current. (a) Equivalent circuit; (b) complex plane showing charging current and loss current. Adapted from Ref. [36]

Generally speaking, permittivity is a complex number, and the imaginary part of permittivity is related to the conductivity of the material.

**Figure 2.9**(a) shows the equivalent circuit of a capacitor C connected to an AC voltage source $V = V_0 \exp(j\omega t)$. The current flowing in the circuit consists of two parts, the charging current ($I_c$) and loss current ($I_1$):

$$I = Ic + I1 = jC\omega V + GV = (jC\omega + G)V\,, \qquad (2.4)$$

where $G$ is the conductance of the dielectric material. As shown in **Figure 2.9**(b), the charging current ($I_c$) leads the source voltage $V$ by a phase angle of 90° and loss current ($I_1$) is in phase with $V$. So the total current $I$ leads $V$ with an angle $\theta$ ($\theta < 90°$). The phase angle between $I_c$ and $I$ is known as *loss angle* $\delta$ and the dielectric loss tangent is given by

$$tan\delta = \varepsilon''/\varepsilon'\,, \qquad (2.5)$$

and the complex permittivity can be expressed as

$$\varepsilon_r = \varepsilon' - j\varepsilon'' = \varepsilon'(1 - jtan\delta)\,. \qquad (2.6)$$

### 2.2.5.2 Electronic and atomic polarizations: The Lorentz model

Electronic polarization occurs in neutral atoms when an electric field displaces the nucleus with respect to the surrounding electrons. Atomic polarization occurs when adjacent positive and negative ions stretch under an applied electric field. These two polarizations have similar natures. In the late 19th century, Hendrik Larentz proposed a model of the dipole oscillator and calculated the frequency dependence of the complex permittivity, which can expressed as

$$\varepsilon_r(\omega) = 1 + \omega_p^2 \sum_j \frac{1}{(\omega_j^2 - \omega^2 - i\gamma_j\omega)}\,, \qquad (2.7)$$

where $\gamma$ is the coefficient of the friction.

According to the Larentz model, the real and imaginary part of the dielectric constant is plotted in **Figure 2.10**.

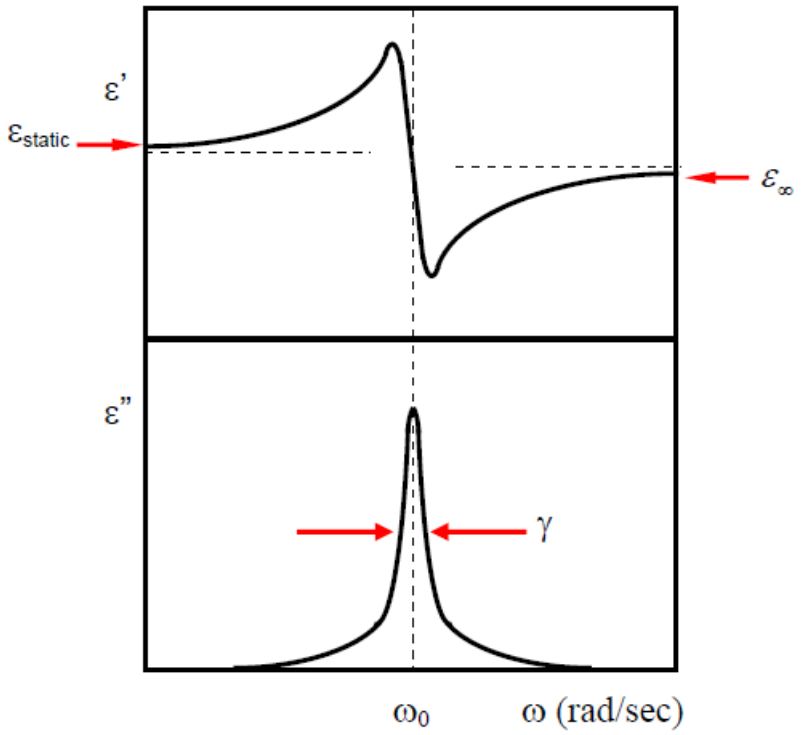


**Figure 2.10** The real and imaginary part of the dielectric constant from the Lorentz Model.

### 2.2.5.3 Dipolar polarization: The Debye model, Cole-Cole Model and the Davidson-Cole Model

In 1929, Peter Debye[37] proposed a model that explained the dipolar relaxation in dielectrics which can also be applied to various types of polarizations. According to the Debye Model, the complex permittivity of a dielectric can be expressed as:

$$\varepsilon^*(\omega) = \varepsilon_\infty + \frac{\varepsilon_0 - \varepsilon_\infty}{1 + j\omega\tau}, \tag{2.8}$$

with

$$\varepsilon_\infty = \lim_{\omega\to\infty} \varepsilon\,, \tag{2.9}$$

$$\varepsilon_0 = \lim_{\omega\to 0} \varepsilon\,, \tag{2.10}$$

where ω is the operating angular frequency, τ is the relaxation time and $\varepsilon^* = \varepsilon' + j\varepsilon"$. The Debye equation indicates that the permittivity of a dielectric is determined by 3 factors, $\varepsilon_0$, $\varepsilon_\infty$ and $\tau$.

According to Eq.2.7 we can determine the real and imaginary parts of the permittivity and the $tan\delta$ as:

$$\varepsilon'^{(\omega)} = \varepsilon_\infty + \frac{\varepsilon_0 - \varepsilon_\infty}{1 + \omega^2\tau^2} \tag{2.11}$$

$$\varepsilon"(\omega) = \frac{(\varepsilon_0 - \varepsilon_\infty)\omega\tau}{1 + \omega^2\tau^2} \tag{2.12}$$

$$tan\delta = \frac{\varepsilon"}{\varepsilon'} = \frac{(\varepsilon_0 - \varepsilon_\infty)\omega\tau}{\varepsilon_0 + \varepsilon_\infty\omega^2\tau^2} \tag{2.13}$$

From Eq. 2.12, the imaginary part $\varepsilon''$ becomes 0 as the frequency $\omega$ approaches both 0 and ∞. At high frequencies, as the relaxation time of the dipoles is larger than the switching period of the electric field, the dipoles are not responding to the electric field and keep randomly oriented. The $\varepsilon_\infty$ is a real number. Since the $\varepsilon_\infty$ is mainly due to electronic and atomic polarizations, it is independent of the temperature. At low frequencies, the phase difference between the electric field and polarization disappears and the $\varepsilon_0$ is a real number. As the disorder of the system increases with increasing temperature, the $\varepsilon_0$ decreases, and $\tau$ decreases as the movements of the dipoles become faster at higher temperatures.

The relationship between $\varepsilon'$, $\varepsilon''$ and $\omega$ is plotted in **Figure 2.11**. The maximum $tan\delta$ value is:

$$tan\delta_{max} = \frac{1}{2} \cdot \frac{\varepsilon_0 - \varepsilon_\infty}{\sqrt{\varepsilon_0\varepsilon_\infty}} \tag{2.14}$$

at the frequency

$$\omega_{max} = \frac{1}{\tau} \cdot \sqrt{\frac{\varepsilon_0}{\varepsilon_\infty}} \cdot \frac{\varepsilon_\infty + 2}{\varepsilon_0 + 2} \tag{2.15}$$

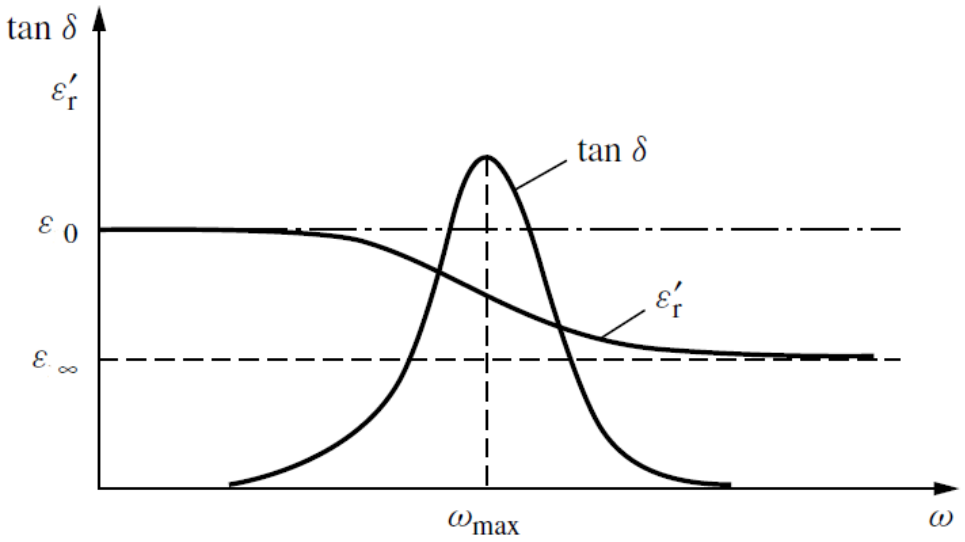


**Figure 2.11** The frequency dependence of the complex permittivity according to the Debye Model. Adapted from Ref.[36]

Although, the Debye Model is able to describe many dipolar relaxations, its approximation to some solids is not in good agreement with the results of actual experiments. Kenneth S. Cole and Robert S. Cole[38] refined the Debye Model. Based on the Debye Model, the relationship between the real and imaginary parts of permittivity can be expressed as

$$(\varepsilon' - \varepsilon_\infty)^2 + (\varepsilon'')^2 = (\varepsilon' - \varepsilon_\infty)(\varepsilon_0 - \varepsilon_\infty) \qquad (2.16)$$

which represents a circle in the real and imaginary axis, as shown in **Figure 2.12**, which is called the Cole-Cole diagram. Only the points at the top half of the circle have physical meaning. The intersection points on the real axis are $\varepsilon_0$ and $\varepsilon_\infty$, and the center of the arc is $(\varepsilon_0 + \varepsilon_\infty)/2$.

According to Eq.2.11 and Eq.2.12, we can derive

$$\varepsilon'' = \beta(\varepsilon' - \varepsilon_\infty) \qquad (2.17)$$

and

$$\varepsilon'' = -\left(\frac{1}{\beta}\right)(\varepsilon' - \varepsilon_0) \tag{2.18}$$

where

$$\beta = \frac{\varepsilon_0 + 2}{\varepsilon_\infty + 2}\omega\tau \tag{2.19}$$

To obtain the relaxation time $\tau$ from the Cole-Cole diagram, we can draw a line which passes through the corresponding point of the frequency and the point at $\varepsilon_0$ or $\varepsilon_\infty$. The slope of the line equals the value of $\beta$ or -1/$\beta$. We can then calculate the $\tau$ from Eq.2.18.

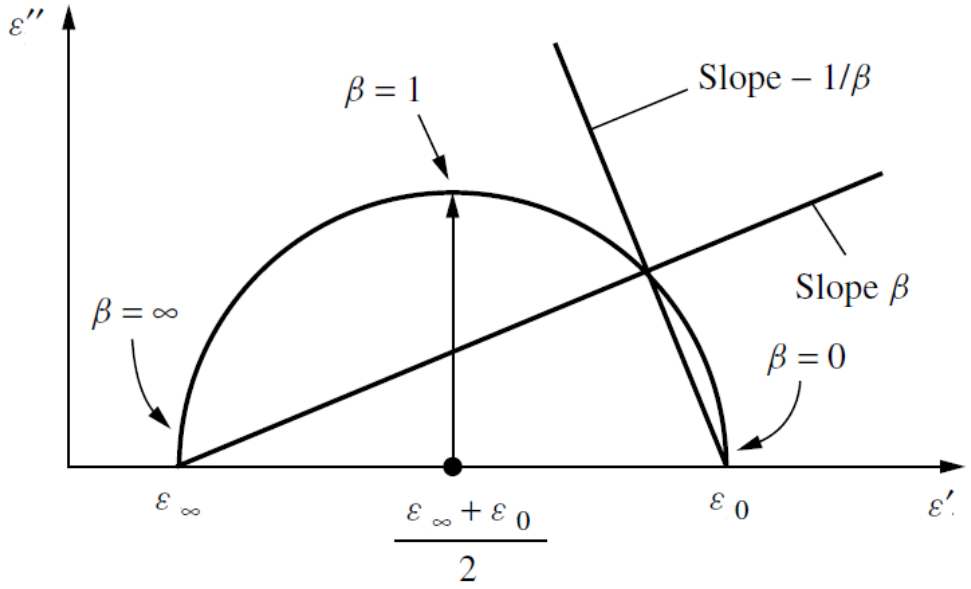


**Figure 2.12** The semicircular Cole-Cole plot of the Debye model. Adapted from Ref.[36]

For those materials which exhibit a distribution of relaxation frequencies, the spreading factor, $\alpha$ ( $0 < \alpha < 1$) is introduced, and Eq.2.7 is modified into

$$\varepsilon^*(\omega) = \varepsilon_\infty + \frac{\varepsilon_0 - \varepsilon_\infty}{1 + (j\omega\tau)^{1-\alpha}} \tag{2.20}$$

which is known as the Cole-Cole model for the complex dielectric constant. The larger $\alpha$ gives a broader curve and when $\alpha = 0$, the Cole-Cole model is reduced to the Debye model. If we plot the $\varepsilon''(\varepsilon')$ in the real and imaginary axes, as shown in **Figure 2.13**, we can also get an arc passing through $\varepsilon_0$ and $\varepsilon_\infty$, and the centre of the circle is below the imaginary axis with a distance d given by

$$d = \frac{\varepsilon_0 - \varepsilon_\infty}{2} tan\theta \tag{2.21}$$

where

$$\theta = \alpha \frac{\pi}{2} \tag{2.22}$$

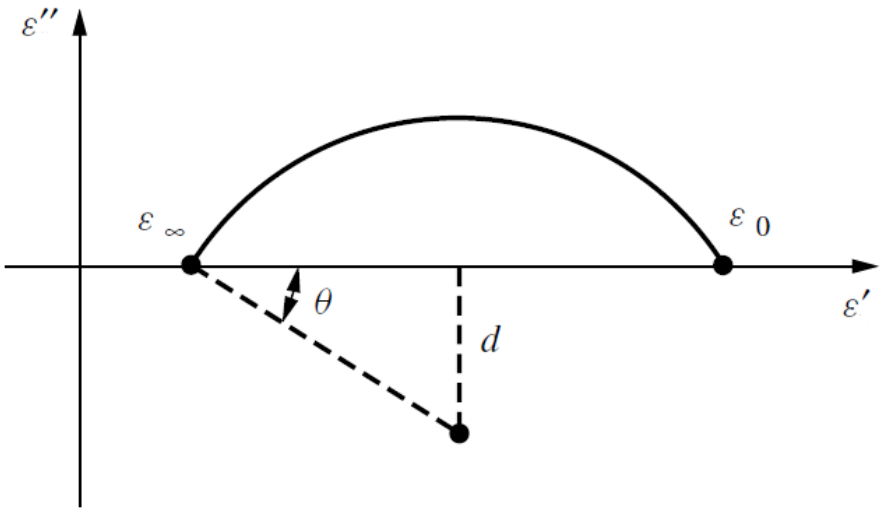


**Figure 2.13** The Cole-Cole diagram for a relaxation-time spectrum. Adapted from Ref. [36]

## 2.2.6 Resistivity

In a later section in this thesis, and to understand the nature of the dielectric properties of FVO thin films, the temperature dependence of the capacitance of the Pd/FVO/Nb:STO junction is simulated by a 2 RC element model in which the resistivity of the film plays an important role. Hence, it is important to measure and understand the transport mechanism of FVO.

At present, there are three models that are commonly used to fit the temperature dependence of the resistivity of the manganites, namely 1) a simple Arrhenius law, 2) a polaron model, and 3) a variable-range hopping model.

(1) Arrhenius law

The Arrhenius equation was first used by Svante Arrhenius to explain the dependence of the rate constant $k$ of a chemical reaction on the activation energy $E_a$ and temperature $T$

$$k = Aexp\left(-\frac{E_a}{RT}\right) \tag{2.23}$$

where $R$ is a gas constant. In general, the Arrhenius law can be used to model activated behaviour due to a band gap $E_a$ or a mobility edge and is expressed as:

$$\rho = \rho_0 \exp\left(\frac{E_a}{k_B T}\right) \tag{2.24}$$

where $Ea$ is the activation energy and $k_B$ is the Boltzman constant. The $E_a$ can be obtained from the slope of the $ln\rho$ v.s. $(1/T)$ curve, as shown in **Figure 2.14**.

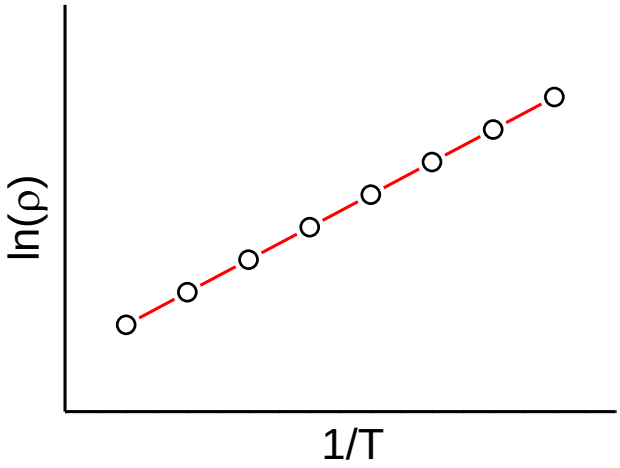


**Figure 2.14** *ln*($\rho$) versus ($1/T$) from the Arrhenius model. The activation energy $E_a$ can be obtained from the slope of the curve.

(2) Polaron Model

A thermally activated mobility can be induced by the nearest-neighbour hopping of small polarons. In the adiabatic regime, the charge-carrier motion is faster than the lattice vibration and the drift mobility is expressed as

$$\mu = \frac{3ea^2}{2}\frac{\omega_0}{2\pi kT} exp\left[-\frac{W_p}{kT}\right] \tag{2.25}$$

where $W_p$=$E_p$/2-$t$. $E_p$ is the polaron formation energy, t is the electronic transfer integral, $\omega_0$ is the longitudinal optical-phonon frequency, a is the hopping distance and e is the electronic charge.

In the nonadiabatic limit, the charge-carrier's motion is slower than the lattice vibrations and the drift mobility is expressed as

$$\mu = \frac{3ea^2}{2\hbar}\frac{t^2}{kT}\left(\frac{\pi}{4W_p kT}\right)^{\frac{1}{2}} exp\left[-\frac{W_p}{kT}\right] \tag{2.26}$$

where $W_p = E_p/2$, and the resistivity is obtained from $\rho = 1/(ne\mu)$.

(3) Variable Range Hopping Model

In 1969, Sir Nevill Mott[39] described the temperature dependence of the resistivity in systems in which the carriers are localized by random potential fluctuation, with variable-range hopping model.

Suppose there are two localized states with a distance of r, and the energies of the two states are $E1$ and $E2$. If the energy difference $W$=$E2$-$E1$>$0$, then by absorbing a phonon, the electron can jump from the first state to the second. If the potential energies of the two states are $\mu_1$ and $\mu_2$, the current can be expressed as

$$I = \frac{er\omega_0}{k_B T}(\mu_1 - \mu_2) exp\left(\frac{-W}{k_B T}\right) exp\left(\frac{-2r}{\xi}\right) \tag{2.27}$$

where $\xi$ is the localization length and $\omega_0$ is the frequency of the phonon. Given that $\mu_1 - \mu_2 = eV$, the resistance can be expressed as

$$R = \frac{k_B T}{e^2 r\omega_0}\left(exp\left(\frac{-W}{k_B T}\right) exp\left(\frac{-2r}{\xi}\right)\right)^{-1} \tag{2.28}$$

and the conductivity can be written as

$$\sigma = \sigma_0 exp\left(-\frac{2r}{\xi} - \frac{W}{k_B T}\right) \tag{2.29}$$

For $d$=3, the density N{E} is given as

$$N\{E\} = \frac{3}{4\pi r^3 w} \tag{2.30}$$

Hence

$$W = \frac{3}{4\pi r^3 N\{E\}} \tag{2.31}$$

By putting Eq. 2.31 into Eq. 2.29 and maximizing $\sigma$, we obtain

$$r = \left(\frac{9\xi}{8\pi N\{E\} k_B}\right)^{\frac{1}{4}} \left(\frac{1}{T}\right)^{\frac{1}{4}} \tag{2.32}$$

Substituting Eq. 2.32 into Eq. 2.29, we obtain

$$\sigma = \sigma_0 exp\left[-\left(\frac{T_0}{T}\right)^{\frac{1}{4}}\right] \tag{2.33}$$

or

$$\rho(T) = \rho_0 \exp\left(\frac{T_0}{T}\right)^{\frac{1}{4}} \tag{2.34}$$

in which $T_0$ is the characteristic barrier energy parameter. By plotting $ln\rho$ against $(1/T)^{0.25}$, we can obtain the value of $T_0$ as the slope of the curve, shown in **Figure 2.15**(a). The relationship between the characteristic parameter $T_0$ and the localization length $\xi$ can be expressed as:

$$T_0 \propto \frac{1}{N\{E\}\xi^3} \tag{2.35}$$

In a localized system, the smaller the localization length $\xi$ is, the more localized the system is, as shown in **Figure 2.15**(b).

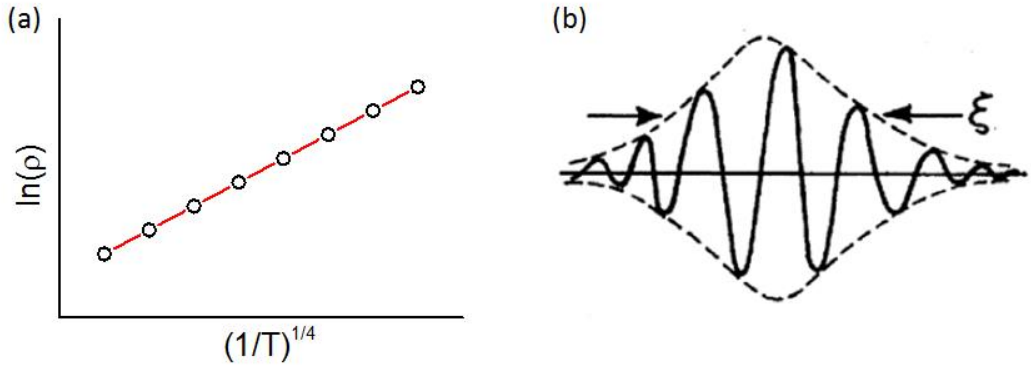


Figure 2.15 (a) *ln*($\rho$) as a function of $(1/T)^{0.25}$. The barrier energy parameter $T_0$ can be obtained as the slope of the curve. (b) A physical interpretation of the localization length $\xi$ in a localized system.[40]

## 2.3 Experimental Methods

### 2.3.1 Thin Film Deposition Methods

Dozens of different deposition technologies have been utilised over time to achieve the growth of electrical and optical thin films.[41] They can be categorised into two foremost groups: physical and chemical deposition. And some of them, such as Reactive sputtering and MBE, are the combination of the two as shown in **Figure 2.16**.

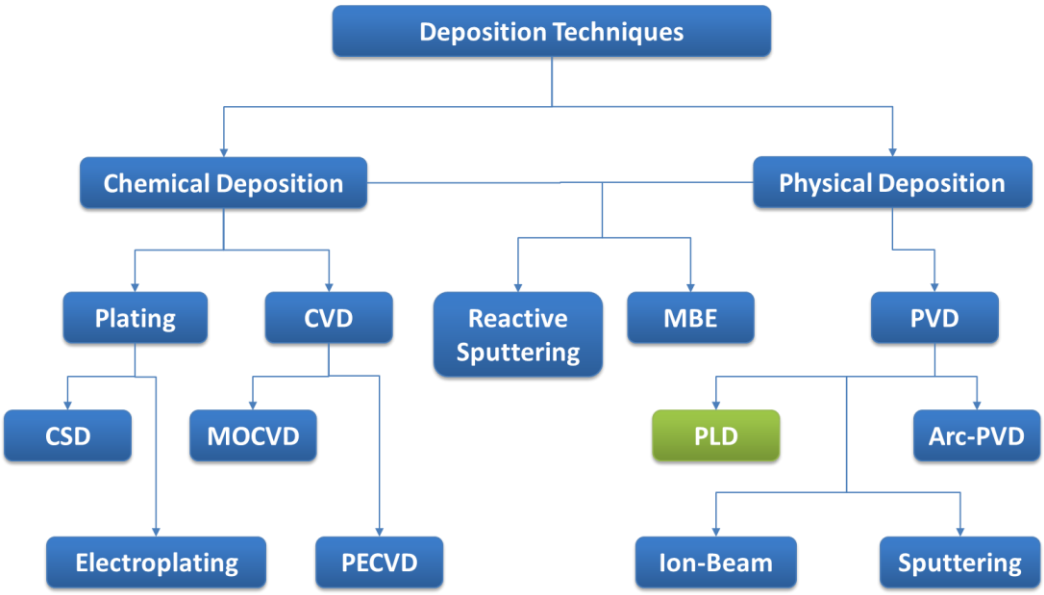


**Figure 2.16** Categories of deposition techniques.

Chemical vapour deposition (CVD) is one of the main classes of chemical deposition. This method involves chemical reactions between precursor gases occurring on and near hot surfaces, resulting in the deposition of a thin film on the surface.[42] The primary advantage of CVD films is that they are quite conformal, in comparison to physical deposition which is less conformal.

The physical deposition techniques such as sputtering, ion beam, cathodic arc and pulsed laser deposition (PLD) are all physical vapour deposition (PVD) techniques.

#### 2.3.1.1 Pulsed Laser Deposition

The first pulsed laser deposition (PLD) was carried out in the 1960s, but it was not popularized until the late 1980s. Compared to other thin film growth methods, PLD has several unique characteristics that make it remarkable in the research area of complex oxide compound thin-film growth. The advantages of the PLD method in the application of complex material film growth are:

(1) The stoichiometric transfer of target material.

(2) The generation of energetic species.

(3) The hyperthermal reaction between the ablated cations and the background gas in the ablation plasma.

(4) Its compatibility with background pressures.[43]

A PLD system consists of several main parts: a laser source, a vacuum chamber, a target holder module and a substrate heating/holder module.

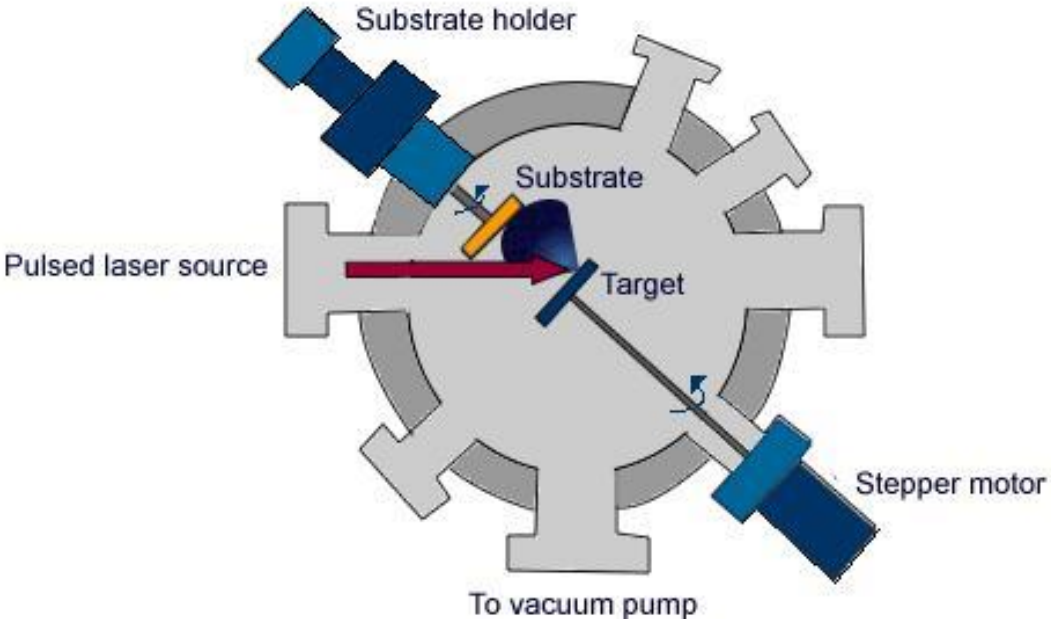


**Figure 2.17** Schematic of the PLD process.

During the deposition, a high-energy pulsed laser beam is focused on the target inside a vacuum chamber. A very high temperature is generated at the point

where the laser strikes and the material of the target is vaporized, which forms a plasma 'plume'. The plume provides a flux of material from the target for thin film deposition on a heated substrate. When the 'plume' hits the substrate, the ablation material is deposited on the substrate. As the 'plume' keeps hitting the substrate, the material starts to nucleate and grow on the surface of the substrate. Compared to other deposition techniques, the main advantage of PLD is that the composition of the plume depends only on the target material, and it is generally easier, in our case, to obtain the desired film stoichiometry for multi-element materials such as complex oxides, FVO and CCO.

### 2.3.2 Reflection high-energy electron diffraction

Reflection high-energy electron diffraction (RHEED) is a technique that is widely used in surface structural analysis because it is very simple to implement.[44] It only requires an electron gun, a phosphor screen and a clean surface (in our case, the FVO sample). As shown in **Figure 2.18**, the electron beam generated by the e-gun strikes the sample surface at a small angle. Incident electrons then diffract from the atoms at the sample surface, and a small fraction of the diffracted electrons interfere constructively at specific angles and form regular patterns on the detector screen. Because of the small glancing angle of the incident beam, the penetration depth is very small. RHEED is primarily sensitive to the atomic structure of the first few layers of the crystal lattice of the sample.

RHEED oscillations can be used as a very fast and accurate method of growth rate monitoring during the growth process of the film. A smooth surface provides intense and coherent spots, whilst a rough surface provides weak and incoherent spots. The degree of the roughness corresponds to each fraction of the growth of one monolayer. A maximum roughness, and hence the lowest intensity of the spots, is achieved at the level of half monolayer growth, while a maximum smoothness, and hence the highest intensity of the spots, is achieved after a full monolayer growth. This is represented in **Figure 2.19**. With this method the

epitaxial growth of a film, within a precision of less than a monolayer, can be achieved.

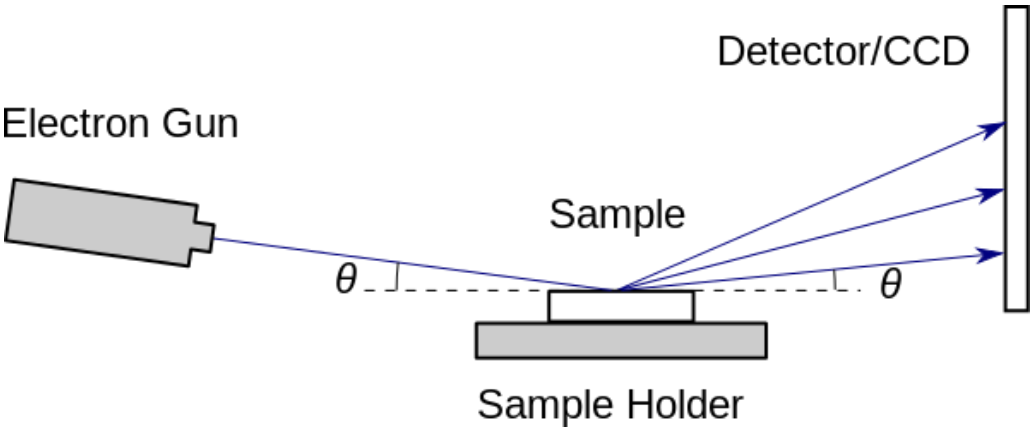


**Figure 2.18** Setup of the electron gun, sample and detector/CCD components of a RHEED system. Electrons follow the path indicated by the arrow and approach the sample at angle θ. The sample surface diffracts electrons, and some of these diffracted electrons reach the detector and form the RHEED pattern.

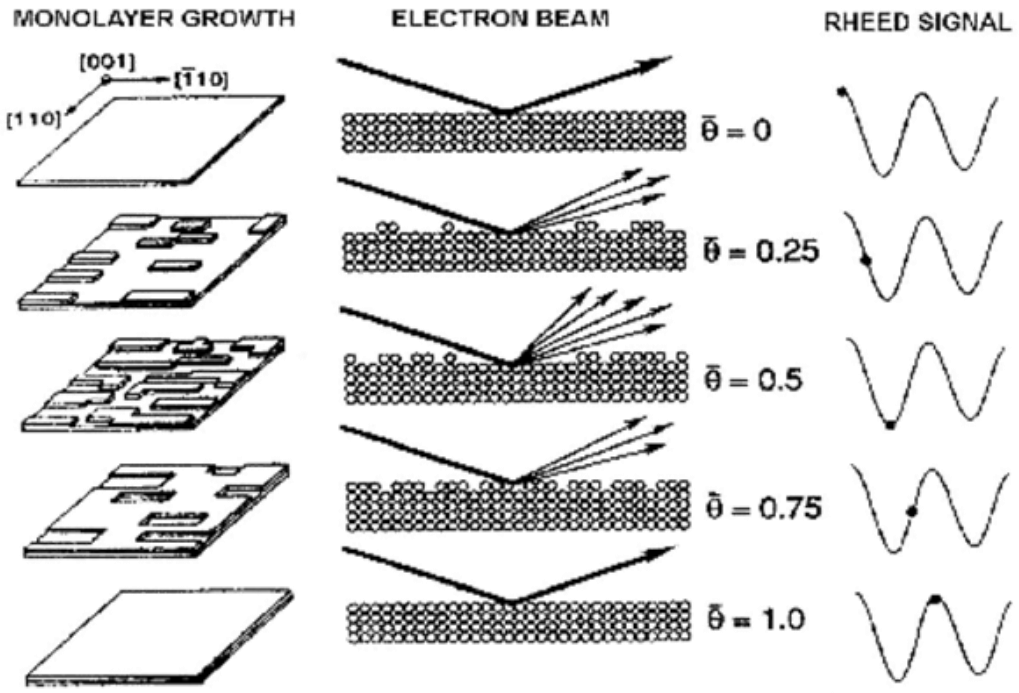


**Figure 2.19** Schematic diagram of RHEED oscillations. Adapted from Ref. [45]

### 2.3.3 X-ray Diffraction

X-ray diffraction is widely used to determine the structure of crystals. When an X-ray hits a crystal, the regular array of electrons in the crystal scatters the X-ray and produces a regular array of secondary spherical waves. According to Bragg's Law:

$$2dsin\theta = n\lambda \tag{2.36}$$

where d is the spacing between diffracting planes, $\theta$ is the incident angle, $n$ is any integer and $\lambda$ is the wavelength of the beam, as illustrated in **Figure 2.20**. The scattered waves will add constructively when Bragg's law is satisfied and produce a reflection spot in the diffraction pattern. With a known $\lambda$, the d spacing of the crystal planes of the sample can be calculated by measuring the $\theta$, which will further determine the structure of the crystal.

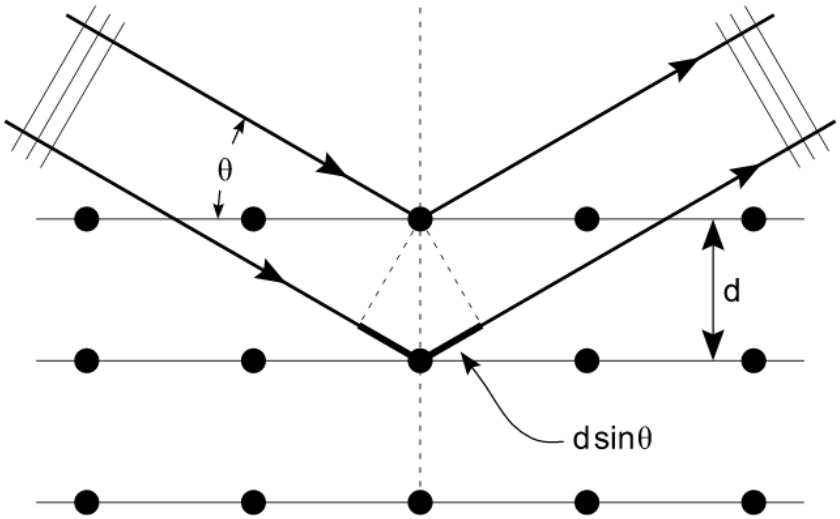


**Figure 2.20** Illustration of Bragg's law. The incoming beam (coming from upper left) causes each scatterer to re-radiate a small portion of its intensity as a spherical wave. If scatterers are arranged symmetrically with a separation d, these spherical waves will be in sync (add constructively) only in directions where their path-length difference $2d$ sin $\theta$ equals an integer multiple of the wavelength $\lambda$. In that case, part of the incoming beam is deflected by an angle $2\theta$, producing a reflection spot in the diffraction pattern.

### 2.3.4 Scanning Probe Microscopy

Scanning probe microscopy (SPM) is a branch of microscopy that acquires images of sample surfaces using a physical probe that scans across the specimen. The first SPM to be built was the scanning tunnelling microscope (STM) which earned it's inventors, Gerd Binnig and Heinrich Rohrer, the Nobel Prize in Physics. In this thesis, several types of SPM were used to measure the structural, magneto and electrical properties.

#### 2.3.4.1 Atomic Force Microscopy

Atomic force Microscopy (AFM) is a powerful tool for the characterization of the surface properties of thin films. It produces very high resolution images of the morphology of the samples. A typical configuration of an AFM is shown in **Figure 2.21**.

The working flow of an AFM is described thus. A small spring-like cantilever with a sharp tip at its free end is mounted to the support, which has a piezoelectric element for oscillating the cantilever at, or slightly below its resonance frequency during the scan. The sample is mounted on the sample stage which is driven by a piezoelectric scanner. As the tip approaches the surface, the attractive force between the surface and the tip causes the cantilever to deflect towards the surface. When the cantilever is brought even closer, repulsive force takes over and causes the cantilever to deflect away from the surface. A laser beam is shot on the back of the cantilever and the reflected beam is sensed by a position-sensitive photo diode. If an AFM tip passes over a raised surface feature, the deflections of the cantilever can be detected by tracking the changes of the reflected beam, and then converted to the height information of the sample. As the tip scans along the x-y grid of the sample surface, the morphology of the sample is recorded and can be plotted as a pseudocolour image.

An AFM can be operated in three modes: contact mode, tapping mode and non-contact mode. In contact mode, the tip is "dragged" across the surface of the sample and a feedback loop, which changes the sample height and keeps the

deflection of the cantilever constant, is used. In tapping mode, the cantilever is oscillating at or near its resonance frequency. The frequency and amplitude (which varies from several nm to 200 nm) of the oscillation will be changed as the tip gets close to the sample. The feedback loop adjusts the sample high and keeps the frequency and amplitude constant, so that the surface height information is acquired. Non-contact mode is similar to tapping mode, while the oscillation amplitude is much smaller in non-contact mode (from a few nanometers down to a few picometers). At this range the Van der Waals forces will decrease the resonance frequency of the cantilever. The feedback loop adjusts the sample height to keep the resonance frequency, and the height is recorded.

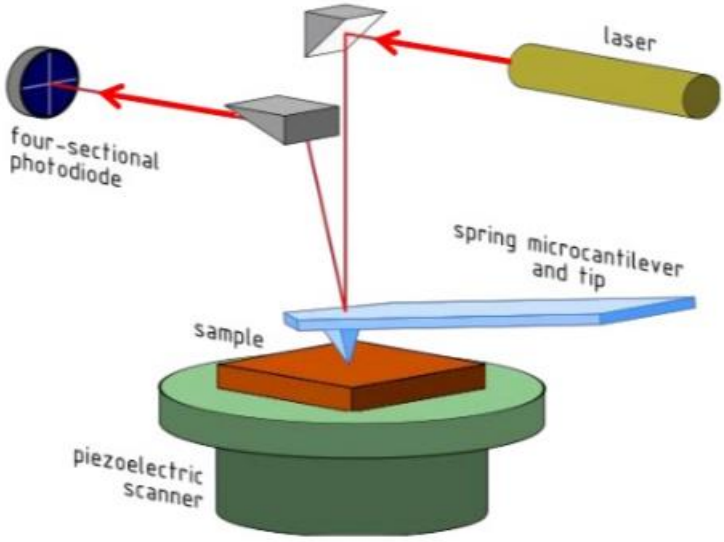


**Figure 2.21** A typical configuration of AFM. Adapted from Ref.[46]

### 2.3.4.2 Magnetic Force Microscopy

Magnetic force microscopy (MFM) is a special mode of operation of the AFM. It measures the surface magnetic field of the sample by incorporating a magnetic probe into an AFM, and is widely used to generate images of magnetic fields associated with small domains.

The principle of MFM is the same as that of AFM. A schematic diagram of the MFM setup is shown in **Figure 2.22**(a). As with AFM, two detection modes can

be used, static and dynamic, but because dynamic mode offers better sensitivity, it is the mode employed for most of this thesis. In a MFM measurement, a sharp tip coated with a magnetic film (such as Ni or Co) is used, as shown in **Figure 2.22**(b). The cantilever, incorporating the magnetic tip, is excited to vibrate at its resonance frequency, having a certain amplitude and phase shift in respect to the drive signal. The deflection sensor of the microscopy monitors the motion of the tip. Influenced by the probe-sample interaction, the spring constant of the cantilever is changed and leads to a shift in resonance frequency. Hence, the oscillation amplitude and its phase are changed by the probe-sample magnetic interaction force. An attractive force will soften the spring constant and decrease the resonance frequency. By scanning the probe through the sample surface, the magnetic information, such as the domain structure, of a certain sample area can be detected.

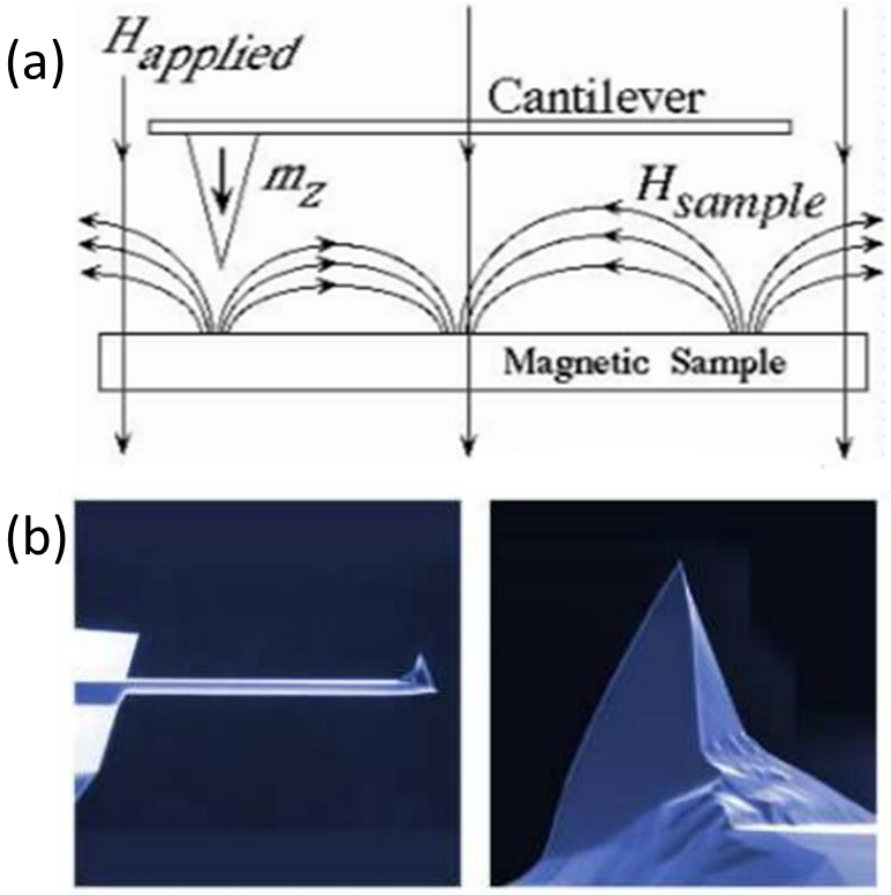


**Figure 2.22** (a) Schematic diagram of a magnetic force microscopy. (b) Scanning electron images of a MFM tip. Adapted from Ref. [47]

### 2.3.4.3 Piezoresponse Force Microscopy

Like MFM, piezoresponse force microscopy (PFM) is also a special mode of AFM. It measures the mechanical response when an electrical voltage is applied to the sample with a conductive tip of an AFM. The local mechanical response, expansion or contraction, to the electrical stimulus is then detected by photo diode, and can be further interpreted in terms of the piezoelectric properties of the sample.[48]

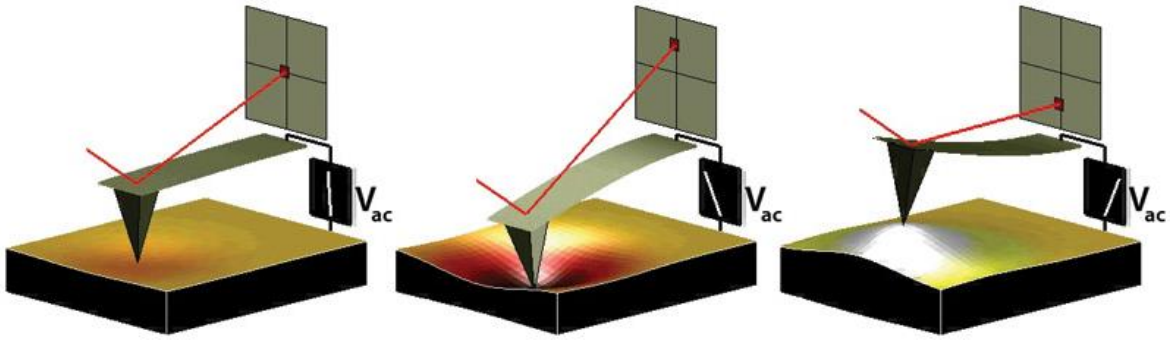


**Figure 2.23** Depiction of PFM operation. Adapted from Ref.[49]

When the tip is in contact with the surface and the local piezoelectric response is detected as the first harmonic component of the tip deflection, the phase $\varphi$, of the electromechanical response of the surface yields information on the polarization direction below the tip. For $c^-$ domains (polarization vector oriented normally to the surface and pointing downward), the application of a positive tip bias results in the expansion of the sample, and surface oscillations are in phase with the tip voltage, $\varphi = 0$, as shown in **Figure 2.24**(a). For $c^+$ domains, the response is opposite and $\varphi = 180°$, shown in **Figure 2.24**(b).

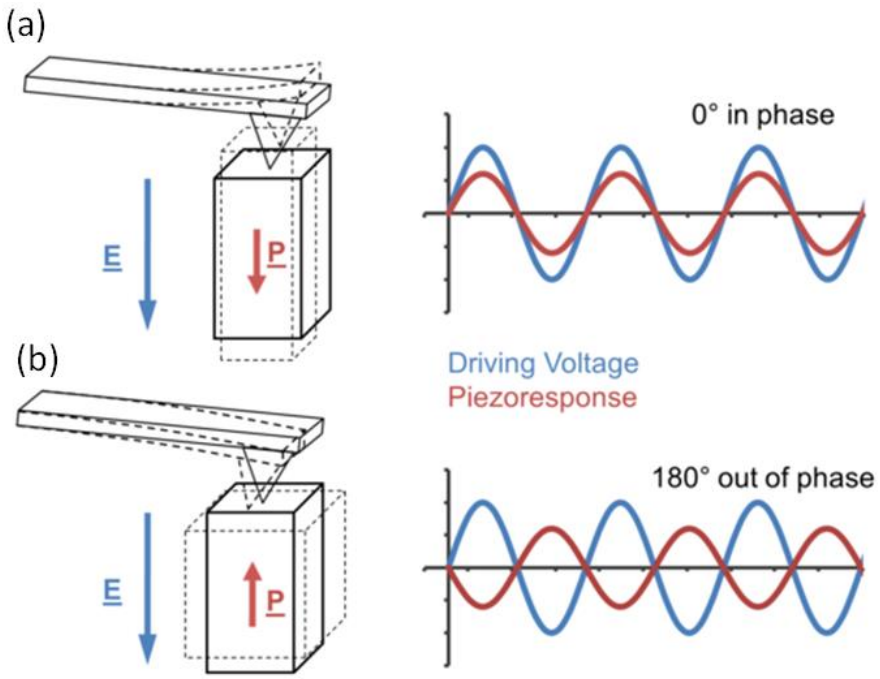


**Figure 2.24** In-phase (a) and 180° out-of-phase (b) piezoresponse. Adapted from Ref.[49]

### 2.3.5 X-ray Absorption Spectroscopy

X-rays are light with energies ranging from ~500 eV to 500 keV. In this regime, an X-ray photon is absorbed by an electron in a tightly bound quantum core level of an atom. This process is called the photo-electric effect.[50] To induce the absorption, the energy of the X-ray must be greater than the binding energy of a particular electronic core level, so that the electron may be perturbed from its quantum level. In this process, the X-ray is absorbed and any excess energy is given to a photon and ejected from the atom, as shown in **Figure 2.25**.

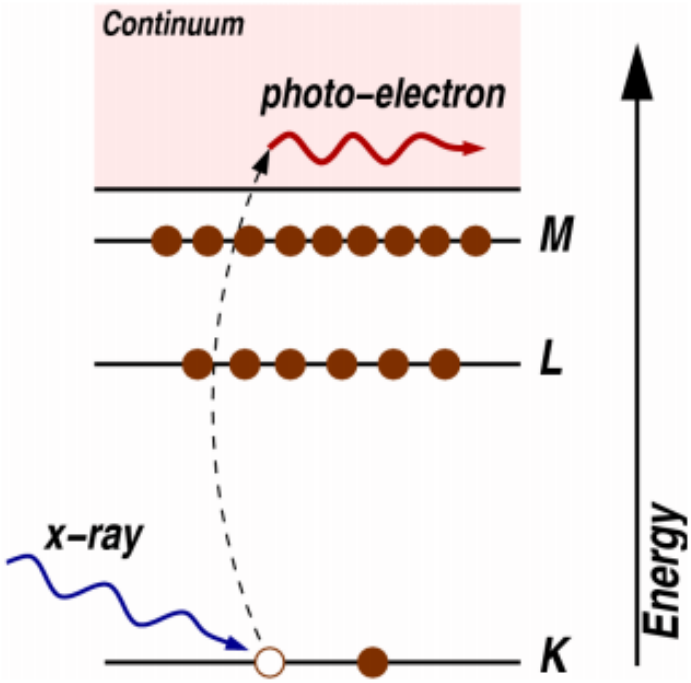


**Figure 2.25** The photoelectric effect, in which an x-ray is absorbed and a core-level electron is promoted out of the atom. Adapted from Ref.[50]

In an XAS measurement, the absorption of X-ray photons is recorded as the photon energy is scanned through the electronic core-level binding energy of a specific element. When the incident X-ray has energy equal to that of the binding energy of a core-level, there is a sharp rise in absorption which is called the absorption edge. The absorption edge corresponds to the promotion of this core-level to the continuum. The "name" of the absorption edge depends on the core electron which is excited: the principal quantum numbers n = 1, 2, and 3, correspond to the *K*-, *L*-, and *M*-edges, respectively. For instance, excitation of a 1*s* electron occurs at the *K*-edge, while excitation of a 2*s* or 2*p* electron occurs at an *L*-edge. Since the core-level binding energy and the absorption coefficient of every atom are distinctively different, the element to be measured can be selected by tuning the energy of an X-ray to an appropriate absorption edge. The region of the XAS spectrum between the absorption edge, and the ~ 30 – 100 eV limit above it, is typically referred to as the near-edge X-ray absorption fine structure (NEXAFS) for measurements in the soft X-ray regime.

The *K* absorption edges of 3*d* transition metal compounds are usually used to determine bond distance and ligand co-ordination numbers because of the scattering of the excited electron by the potential field of the neighbouring atoms. The L absorption edges, on the other hand, contain completely different information. The dipole transitions from the core 2*p* level to the empty 3*d* states, which depend on the local electronic structure, are the origins of the absorption. Thus, the $L_{2,3}$ absorption spectrum can be used to analyse the oxidation state and the symmetry of the 3d transition metal ions. The 2*p* (*L* edge) spectra consist of a $2p_{3/2}$ (L3) and $2p_{1/2}$ ($L_2$) structure with an energy separation, whereby the heavier elements show more distinct separation into two structures than the lighter elements show. The spectra of different $d^n$ configurations are quite different, and this can be used to identify the valency of an element.[51]

### 2.3.6 X-ray Magnetic Circular Dichroism

While XAS is widely used in the study of local structure and oxidation states in different matters, such as metal complexes, X-ray magnetic circular dichroism (XMCD) has been developed to probe for detailed information regarding the electronic and magnetic structure of materials since 1986, when the synchrotron radiation based XMCD technique was first being proofed experimentally.[52] The principle of XMCD is the same as for those of the techniques of magneto-optical phenomena, such as the Faraday effect. While a valence electron is excited in the Faraday effect, the XMCD originates from the excitation of a core electron into the unoccupied conduction states. The XMCD spectrum is the difference between the two XAS spectra, with the circular polarization vector either parallel, or antiparallel to the external magnetic field. The XMCD effect is strong because it arises from electric dipole transitions which have a large core spin-orbit coupling.

There are 2 levels, $2p_{3/2}$ ($L_3$ edge) and 2*p*1/2 ($L_2$ edge), in the 2*p* core state of a 3*d* metal. In each level, the spin and orbit are coupled parallel and antiparallel, respectively. In a XMCD process, the 2*p* core electron of preferred spin up, or down, direction is excited by a light with a helicity vector parallel, or antiparallel, to the

orbital moment. Then, the excited electron with a certain spin direction has to find its place in the unoccupied 3*d* valence band, and if the amount of available holes with different spin direction is different, the sing of the $L_3$ and $L_3$ peak in the XMCD spectrum will be different. **Figure 2.26** (a) shows a two-step process of the excitation in the XMCD and (b) shows a XMCD spectrum of a typical 2*d* metal (Co). Due to the element-specific nature of XAS, XMCD can be used to detect the spin and orbital structure of a specific element in a material.

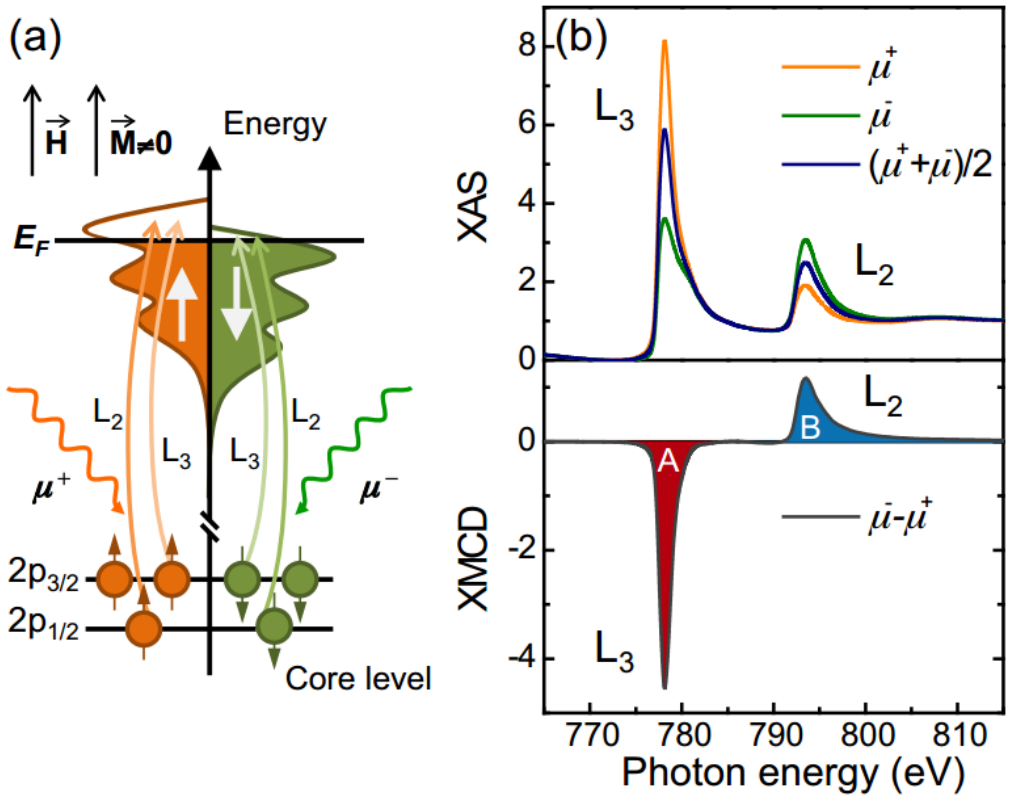


**Figure 2.26** (a) Diagram of the two-step picture of XMCD for a single-electron in the resonant excitation process for a magnetic material. In the first step, a circularly polarized photon excites a spin polarized electron from the spin–orbit split 2*p* level (Fano-effect). From the $2p_{3/2}$ level ($L_3$ edge) X-rays with positive helicity ($q$=+1) excite 62.5% spin up electrons and those with negative helicity ($q$=−1) excite 37.5% spin-up electrons, while the $2p_{1/2}$ level ($L_2$ edge) $q$=+1 gives 25% spin-up and $q$=−1 gives 75% spin-up. Note that the minority spin direction (=majority hole spin direction) is the same as that of the sample direction. In the second step the spin polarized electrons have to find a place in the unoccupied 3*d* band, resulting in a difference if the 3*d* electrons are spin polarized. (b) XAS at the Co $L_{2,3}$ for right (+) and left (−) circular polarization together with the difference spectrum: the XMCD. Adapted from Ref.[53]

Sum rules, developed in the early 1990's, [54] allow us to directly extract the spin and orbital moments of the ground state from XMCD spectra by integrating the intensities over the absorption edges. The sum rules are:

$$M_L = -\frac{4}{3}\frac{\int_{L_{3,2}}(\mu_+ - \mu_-)d\omega}{\int_{L_{3,2}}(\mu_+ + \mu_-)d\omega}N_h \tag{2.37}$$

$$M_S = -\frac{6\int_{L_3}(\mu_+ - \mu_-)d\omega - 4\int_{L_{3,2}}(\mu_+ - \mu_-)d\omega}{\int_{L_{3,2}}(\mu_+ + \mu_-)d\omega}N_h/(1 + \frac{7 < T_z >}{2 < S_z >}) \tag{2.38}$$

in which $M_L$ and $M_S$ represent the orbital and spin magnetic moments, in units of Bohr magnetons($\mu_B$). $\mu_+$ and $\mu_-$ denote the XAS signal at positive and negative helicities, respectively. $\mu_+ - \mu_-$ is the resulting XMCD signal. $\omega$ denotes the photon energy. The integration range is specified for each integral, whether done on the full spectrum ($L_{3,2}$) or through the $L_3$ edge only ($L_3$). $N_h$ is the total number of holes in the $3d$ valence band per unit. $<T_z>$ and $<S_z>$ are the expectation values of the magnetic dipole operator and spin operator, respectively.

### 2.3.7 Superconducting Quantum Interference Device

The superconducting quantum interference device (SQUID) is an extremely sensitive magnetometer used to measure very subtle magnetic fields. The device is a loop made of superconductor with a Josephson junction in each branch of the loop, as shown in **Figure 2.27**(a). An input current, $I$, splits into the two branches equally, if there is no external magnetic field. If an external magnetic field is applied to the loop, a current begins circulating in the loop and changes the current in the two branches in opposite directions. When either one of the currents in the branches exceeds the critical current, $I_c$, of the Josephson junction, a voltage with a phase difference, $\Delta\Phi$, appears across the junction and this phase difference has a periodic dependence on the intensity of the applied field. By measuring the circulating current, one can measure the magnetic field with SQUID. The typical configuration of a SQUID magnetometer is shown in **Figure 2.27**(b). The

magnetic field is picked up by the pickup loop and amplified in the input coil, and then the magnetic field generated by the input coil is detected by the SQUID.

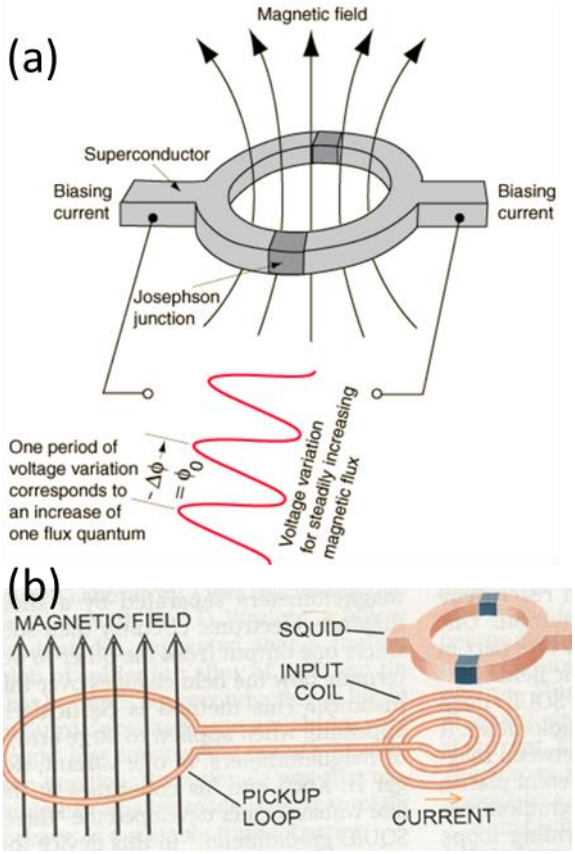


Figure 2.27 (a) Schematic diagram of a SQUID. (b) A typical configuration of a SQUID magnetometer. Adapted from Ref.[49]

### 2.3.8 A Dynamic Method of Measuring Pyroelectric Current

The Pyroelectric effect, known since ancient times[55], is a phenomenon of certain materials, displaying temporary voltage followed by external current, when subjected to a temperature gradient. Only those polar crystals with asymmetric crystal structures, which display spontaneous polarization, can generate pyroelectricity. The position of the atoms within the crystal changes under a temperature gradient, leading to a change of the spontaneous polarization. To compensate for the change in the spontaneous polarization, the depolarization charges, which are attracted to the crystal, cancel the internal

electric field, and the charges are redistributed and expressed as the pyroelectric current.

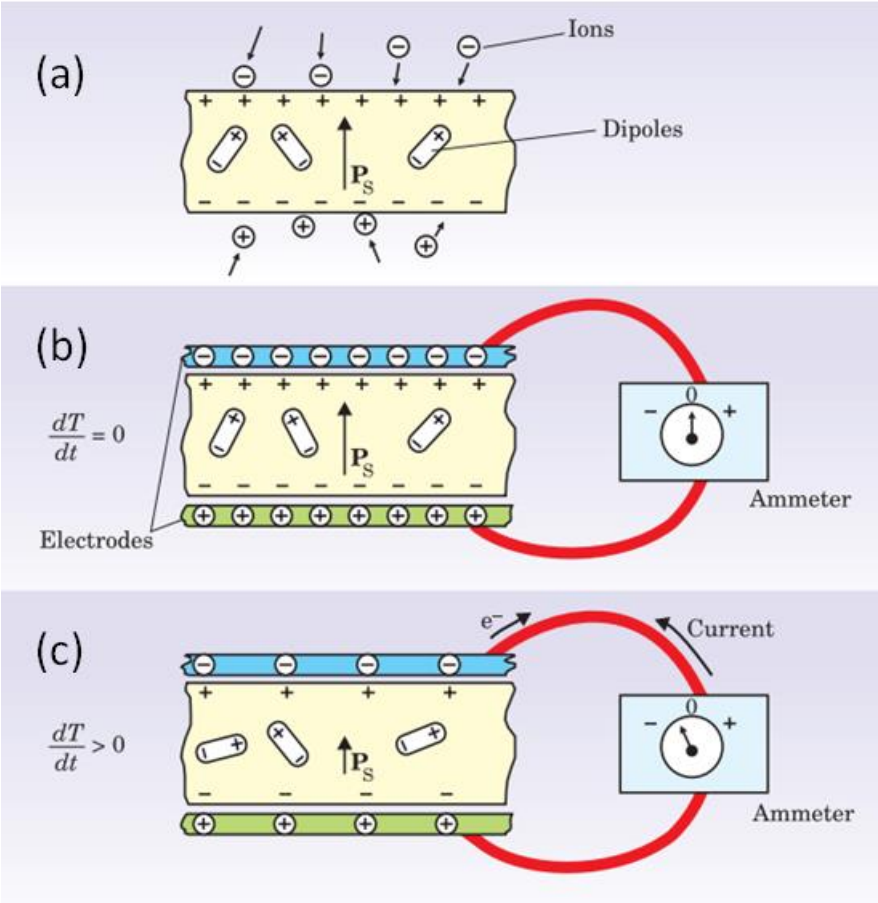


**Figure 2.28** If a pyroelectric crystal with an intrinsic dipole moment (a) is fashioned into a circuit with electrodes attached on each surface (b), an increase in temperature T prompts the spontaneous polarization Ps to decrease as the dipole moments, on average, diminish in magnitude. The horizontal tilting of the dipoles (c) signifies the effect. A current flows to compensate for the change in bound charge that accumulates on the crystal edges. Adapted from Ref.[56]

To measure the pyroelectric effect of our FVO thin films, a dynamic method was used.[57] Compared to static techniques, in which the charge on a crystal surface is measured by an electrometer immediately before and after an appreciable change in the temperature, the dynamic method is very convenient and is widely used to study the polarization behaviour in ferroelectrics[58]. In some situations, the polarization cannot be studied by the conventional methods. For example if the sample is too 'leaky' or the polarization is too small, the dynamic method shows its advantage.

The basis of the method is explained as follows. Take $P_s$ as the spontaneous polarization of the material per unit area at a temperature *T*. A small change $dP_s$ in $P_s$ will be induced by a small change of $dT$ in a time dt. Then, the rate of the changes of the polarization is ($dP_s/dt$) which is equivalent to a current, $i$, flowing in an external circuit. Hence, the current per unit area of the material can be expressed as

$$i = \left(\frac{dP_s}{dt}\right) = \left[\left(\frac{dP_s}{dT}\right)\left(\frac{dT}{dt}\right)\right]_{T=T} \tag{2.39}$$

For a small $\Delta T$, ($dP_s/dT$) can be regarded as constant for that temperature, so that the current depends only on ($dT/dt$), the range of change of the temperature.

In an experiment, a small piece of sample material is used in order to get a low thermal capacity. A light is used as the heating source. The experiment is made using a series circuit consisting of a voltage supply, the sample and a high resistance, which is connected to a sensitive electrometer. The variation of current with time is recorded when the sample is illuminated or after illumination.

At time $t = 0$, when the illumination of the crystal is commenced, the temperature rises initially at the maximum rate $(dT/dt)_{t=0}$. As T increases, $(dT/dt)$ decreases and becomes $0$ when $T$ reaches the equilibrium value. When the light is cut off, the sample starts to cool. Similarly to the heating process, the cooling starts at a maximum cooling rate and then gradually reduces to zero as the sample reaches the original temperature. The change of the $(dT/dt)$ is reflected in the pyroelectric current, with a spike when heating and cooling begin with opposite directions, as shown in **Figure 2.29**.

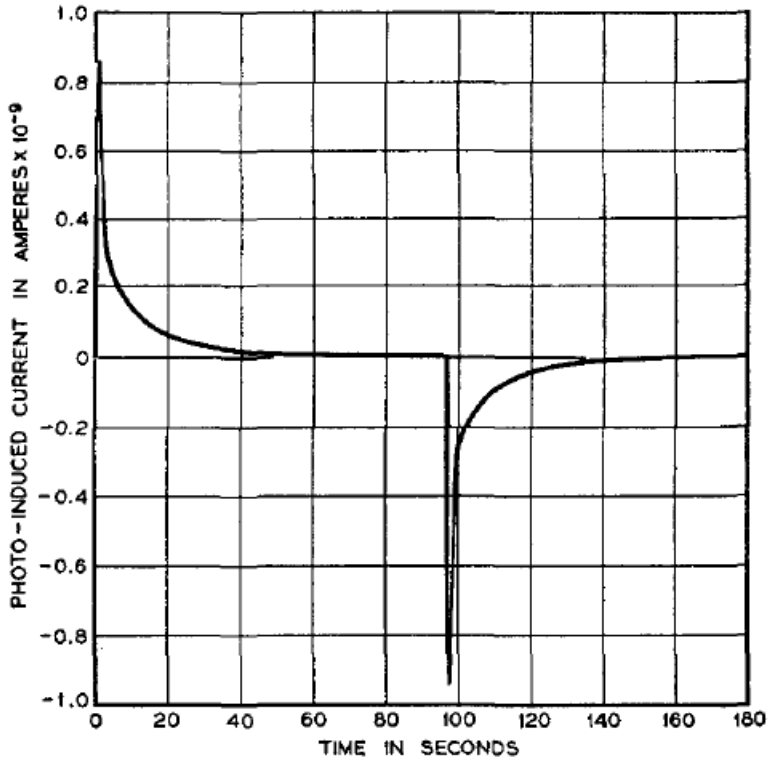


**Figure 2.29** The time variation of the pyroelectric current during a light-dark cycle. Adapted from Ref.[57]

### 2.3.9 Four Point Resistivity Measurement

In this study, the 4-point probe method was used, and the configuration of the measurement is shown in **Figure 2.30**(a). The advantage of four point contacts, as compared to a 2 contacts method, is that it can eliminate the resistance from the wires and contacts. In a 2 contacts configuration, as shown in Fig 2.30(b), the wires from the voltmeter and ammeter are connected together to the sample, so that the resistance of the wires and contacts are also measured together with the sample as:

$$V = i(R_s + R_{c1} + R_{c2} + R_{w1} + R_{w2}) \tag{2.40}$$

However, with a 4-point probe method only the resistance of the sample is measured:

$$V = iR_s \tag{2.41}$$

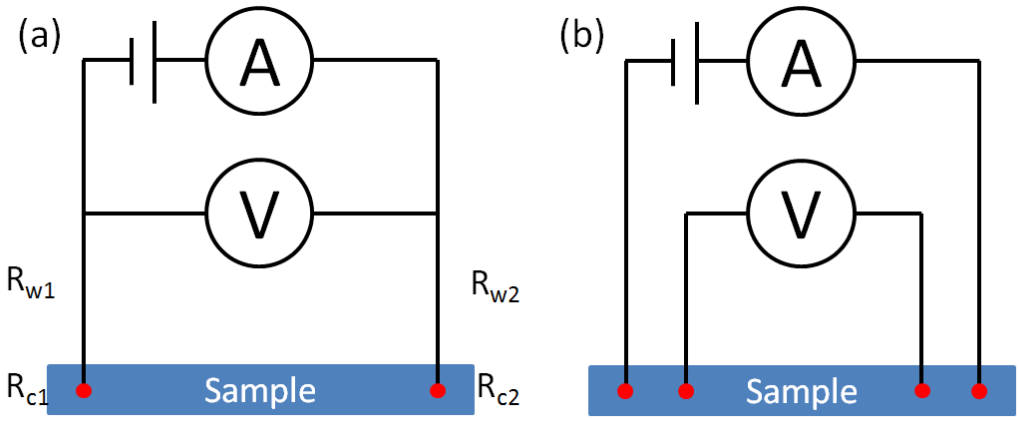


**Figure 2.30** The difference between 2-point (a) and 4-point (b) measurements.

### 2.3.10 Measurement of Impedance

Impedance ($Z$) is defined as the total opposition a device offers to the flow of an alternating current (AC) at a given frequency, and is a complex quantity. The real part is the resistance $R$ and the imaginary part is the reactance $X$, as shown in **Figure 2.31**(a). The relationships between $Z$, $R$, $X$ and the phase angle $\theta$ are

$$Z = R + jX = |Z| \tag{2.42}$$

$$R = |Z|cos\theta \tag{2.43}$$

$$X = |Z|sin\theta \tag{2.44}$$

$$|Z| = \sqrt{R^2 + X^2} \tag{2.45}$$

$$\theta = tan^{-1}\left(\frac{X}{R}\right) \tag{2.46}$$

Reactance has two forms: inductive ($X_L$) and capacitive ($X_C$). Here, $X_L = 2\pi fL$ and $X_C = 1/(2\pi fC)$, where $f$ is the frequency, $L$ is inductance and $C$ is capacitance.

Since impedance is a complex quantity, it is necessary to measure at least two values to acquire the impedance of a device/circuit. Most instruments we use today measure the real and imaginary parts of an impedance vector and then convert them into the parameters we are looking for, such as $|\mathrm{Z}|$, R, L, and C. In our case, we measured the capacitance and the conductance (loss) of the device using a capacitance bridge. A basic idea of the capacitance bridge is shown in **Figure 2.31**(b). The bridge is made of three known devices ($Z_1$, $Z_2$ and $Z_3$) and an unknown device $Z_x$. When the reading of the voltmeter is zero, the bridge is balanced. The $Z_x$ can be calculated by

$$Z_x = \frac{Z_1 Z_3}{Z_2} \tag{2.47}$$

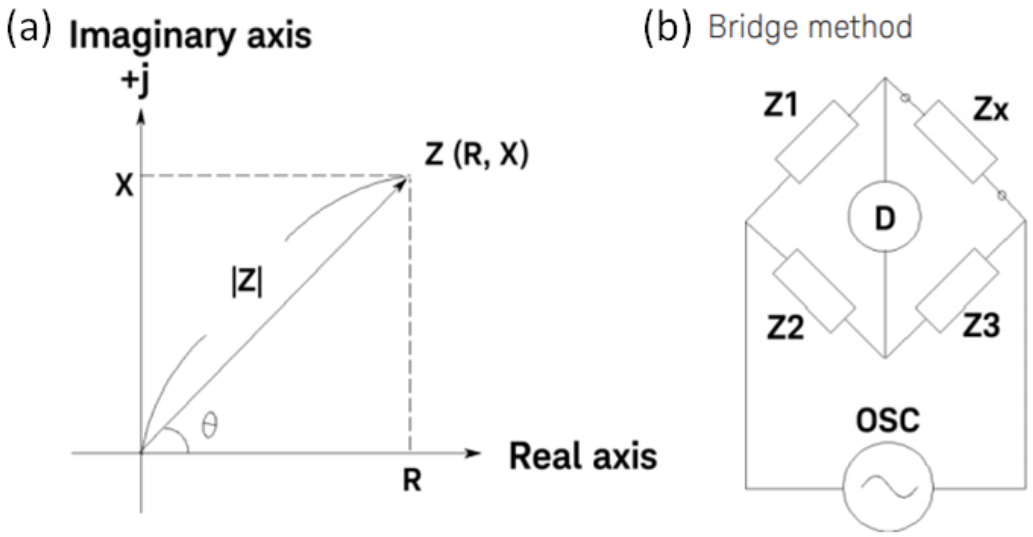


**Figure 2.31** (a) The complex diagram of impedance. (b) A simple capacitance bridge circuit.

References

[1] Y. Yamasaki, S. Miyasaka, Y. Kaneko, J. P. He, T. Arima, Y. Tokura,Magnetic reversal of the ferroelectric polarization in a multiferroic spinel oxide, Phys. Rev. Lett. 2006, 96.
[2] C. Kittel, *Introduction to solid state physics*, Wiley, Hoboken, NJ 2005.
[3] J. M. D. Coey, *Magnetism and magnetic materials*, Cambridge University Press, Cambridge 2010.
[4] N. A. Hill,Density functional studies of multiferroic magnetoelectrics, Annu. Rev. Mater. Res. 2002, 32, 1.
[5] P. Weiss,The specific heat and molecular field of ferromagnetic substances, Cr. Hebd. Acad. Sci. 1907, 145, 1417.
[6] E. C. Stoner,Atomic moments in ferromagnetic metals and alloys with non-ferromagnetic elements., Philos. Mag. 1933, 15, 1018.
[7] G. H. Haertling,Ferroelectric ceramics: History and technology, J. Am. Ceram. Soc. 1999, 82, 797.
[8] L. M. Sheppard,Advances in Processing of Ferroelectric Thin-Films, Am. Ceram. Soc. Bull. 1992, 71, 85.
[9] J. Valasek,Piezo-electric and allied phenomena in Rochelle salt., Phys. Rev. 1921, 17, 475.
[10] H. D. Megaw,Crystal Structure of Barium Titanate, Nature 1945, 155, 484.
[11] S. Miyake, R. Ueda,On Polymorphic Change of Batio3, J Phys Soc Jpn 1946, 1, 32.
[12] N. A. Hill,Why are there so few magnetic ferroelectrics?, J. Phys. Chem. B 2000, 104, 6694.
[13] R. E. Cohen, H. Krakauer,Electronic-Structure Studies of the Differences in Ferroelectric Behavior of BaTiO3 and PbTiO3, Ferroelectrics 1992, 136, 65.
[14] H. Schmid,Multi-ferroic magnetoelectrics, Ferroelectrics 1994, 162, 317.
[15] M. Fiebig,Revival of the magnetoelectric effect, J. Phys. D Appl. Phys. 2005, 38, R123.
[16] W. Eerenstein, N. D. Mathur, J. F. Scott,Multiferroic and magnetoelectric materials, Nature 2006, 442, 759.
[17] N. A. Spaldin, M. Fiebig,The renaissance of magnetoelectric multiferroics, Science 2005, 309, 391.
[18] T. Kimura, S. Kawamoto, I. Yamada, M. Azuma, M. Takano, Y. Tokura,Magnetocapacitance effect in multiferroic BiMnO3, Physical Review B 2003, 67.
[19] S. W. Cheong, M. Mostovoy,Multiferroics: a magnetic twist for ferroelectricity, Nature Mater. 2007, 6, 13.
[20] A. P. Levanyuk, D. G. Sannikov,Improper Ferroelectrics, Usp Fiz Nauk 1974, 112, 561.
[21] B. B. Van Aken, T. T. M. Palstra, A. Filippetti, N. A. Spaldin,The origin of ferroelectricity in magnetoelectric YMnO3, Nat. Mater. 2004, 3, 164.
[22] T. Katsufuji, S. Mori, M. Masaki, Y. Moritomo, N. Yamamoto, H. Takagi,Dielectric and magnetic anomalies and spin frustration in hexagonal RMnO3 (R = Y, Yb, and Lu), Phys.Rev. B 2001, 64.
[23] N. Ikeda, H. Ohsumi, K. Ohwada, K. Ishii, T. Inami, K. Kakurai, Y. Murakami, K. Yoshii, S. Mori, Y. Horibe, H. Kito,Ferroelectricity from iron valence ordering in the charge-frustrated system LuFe2O4, Nature 2005, 436, 1136.
[24] L. D. Landau, E. M. Lifshits, *Electrodynamics of continuous media*, Pergamon Press, Oxford, New York, 1960.
[25] J. Wang, J. B. Neaton, H. Zheng, V. Nagarajan, S. B. Ogale, B. Liu, D. Viehland, V. Vaithyanathan, D. G. Schlom, U. V. Waghmare, N. A. Spaldin, K. M. Rabe, M. Wuttig, R.

Ramesh,Epitaxial BiFeO3 multiferroic thin film heterostructures, Science 2003, 299, 1719.
[26] P. Royen, K. Swars,Das System Wismutoxyd-Eisenoxyd Im Bereich Von 0 Bis 55 Mol-Percent Eisenoxyd, Angew. Chem. Int. Edit 1957, 69, 779.
[27] F. Kubel, H. Schmid,Structure of a Ferroelectric and Ferroelastic Monodomain Crystal of the Perovskite Bifeo3, Acta. Crystallogr. B 1990, 46, 698.
[28] I. Sosnowska, T. Peterlinneumaier, E. Steichele,Spiral Magnetic-Ordering in Bismuth Ferrite, J. Phys. C Solid State 1982, 15, 4835.
[29] P. Fischer, M. Polomska, I. Sosnowska, M. Szymanski,Temperature-Dependence of the Crystal and Magnetic-Structures of Bifeo3, J. Phys. C Solid State 1980, 13, 1931.
[30] F. Zavaliche, S. Y. Yang, T. Zhao, Y. H. Chu, M. P. Cruz, C. B. Eom, R. Ramesh,Multiferroic BiFeO3 films: domain structure and polarization dynamics, Phase Transit 2006, 79, 991.
[31] H. Katsura, N. Nagaosa, A. V. Balatsky,Spin current and magnetoelectric effect in noncollinear magnets, Phys. Rev. Lett. 2005, 95.
[32] I. A. Sergienko, E. Dagotto,Role of the Dzyaloshinskii-Moriya interaction in multiferroic perovskites, Phys. Rev. B 2006, 73.
[33] I. Dzyaloshinsky,A Thermodynamic Theory of Weak Ferromagnetism of Antiferromagnetics, J. Phys. Chem. Solids 1958, 4, 241.
[34] T. Moriya,Anisotropic Superexchange Interaction and Weak Ferromagnetism, Phys. Rev. 1960, 120, 91.
[35] T. Kimura,Spiral magnets as magnetoelectrics, Annu. Rev. Mater. Res. 2007, 37, 387.
[36] L. F. Chen, C. K. Ong, C. P. Neo, V. V. Varadan, V. K. Varadan, in *Microwave Electronics: Measurement and Materials Characterization*, John Wiley & Sons, Ltd, 2004, 8.
[37] P. Debye, *Polar Molecules*, New York: Chemical Catalog, 1929.
[38] K. S. Cole, R. H. Cole,Dispersion and absorption in dielectrics I. Alternating current characteristics, J. Chem. Phys. 1941, 9, 341.
[39] N. F. Mott,Conduction in Non-Crystalline Materials 3. Localized States in a Pseudogap and near Extremities of Conduction and Valence Bands, Philos. Mag. 1969, 19, 835.
[40] P. A. Lee, T. V. Ramakrishnan,Disordered Electronic Systems, Rev. Mod. Phys. 1985, 57, 287.
[41] K. Seshan, *Handbook of thin-film deposition processes and techniques : principles, methods, equipment, and applications*, Noyes Publications, Norwich, N.Y. 2002.
[42] J.-H. Park, T. S. Sudarshan, *Chemical vapor deposition*, ASM International, Materials Park, OH 2001.
[43] R. Eason, *Pulsed laser deposition of thin films : applications-led growth of functional materials*, Wiley-Interscience, Hoboken, N.J. 2007.
[44] W. Braun, *Applied RHEED : reflection high-energy electron diffraction during crystal growth*, New York : Springer Berlin 1999.
[45] J. H. Neave, B. A. Joyce, P. J. Dobson, N. Norton,Dynamics of Film Growth of Gaas by Mbe from Rheed Observations, Appl. Phys. A-Mater. 1983, 31, 1.
[46] http://www.slideshare.net/joybiitk/atomic-force-microscope-fundamental-principles
[47] R. Proksch, G. D. Skidmore, E. D. Dahlberg, S. Foss, J. J. Schmidt, C. Merton, B. Walsh, M. Dugas,Quantitative magnetic field measurements with the magnetic force microscope, Appl. Phys. Lett. 1996, 69, 2599.

[48] P. Guthner, K. Dransfeld,Local Poling of Ferroelectric Polymers by Scanning Force Microscopy, Appl. Phys. Lett. 1992, 61, 1137.
[49] https://www.asylumresearch.com/Applications/PFMAppNote/PFMAppNote.shtml
[50] M. Newville,Fundamentals of XAFS, Rev. Mineral Geochem. 2014, 78, 33.
[51] C. T. Chen, F. Sette,High-Resolution Soft-X-Ray Spectroscopies with the Dragon Beamline, Phys. Scripta. 1990, T31, 119.
[52] G. Vanderlaan, B. T. Thole, G. A. Sawatzky, J. B. Goedkoop, J. C. Fuggle, J. M. Esteva, R. Karnatak, J. P. Remeika, H. A. Dabkowska,Experimental Proof of Magnetic-X-Ray Dichroism, Phys. Rev. B 1986, 34, 6529.
[53] G. van der Laan, A. I. Figueroa,X-ray magnetic circular dichroism-A versatile tool to study magnetism, Coordin. Chem. Rev. 2014, 277, 95.
[54] P. Carra, B. T. Thole, M. Altarelli, X. D. Wang,X-Ray Circular-Dichroism and Local Magnetic-Fields, Phys. Rev. Lett. 1993, 70, 694.
[55] J. Volger,The Specific Heat of Barium Titanate between 100 K and 410 K, Philips Res. Rep. 1952, 7, 21.
[56] S. B. Lang,Pyroelectricity: From ancient curiosity to modern imaging tool, Phys. Today 2005, 58, 31.
[57] A. G. Chynoweth,Dynamic Method for Measuring the Pyroelectric Effect with Special Reference to Barium Titanate, J. Appl. Phys. 1956, 27, 78.
[58] R. Takahashi, H. Misumi, M. Lippmaa,Pyroelectric detection of spontaneous polarization in magnetite thin films, Phys. Rev. B 2012, 86.

# CHAPTER THREE

# 3 SYNTHESIS AND STRUCTURAL CHARACTERIZATION OF IRON VANADATE FILMS

## 3.1 Synopsis

This chapter presents the work undertaken to produce high quality phase pure epitaxial spinal FVO films on perovskite STO substrates. It begins with an introduction of the experimental details. Next, the effect of PLD process parameters on the FVO film qualities and the optimized growth conditions are presented. Following this, the structural characterization is presented and the stress and epitaxial nature of the films are discussed, including how In-situ RHEED was employed to study the growth and stress release mechanism of the films. Lastly, the growth of electrode layers and the integration with FVO films is presented.

## 3.2 Growth of FVO film with PLD

### 3.2.1 Deposition System

The system used for the deposition is the Combination Vacuum System (Model: PA-LMLP-1001) produced by Pascal Co. Ltd., Japan, as shown in **Figure 3.1**. The excimer laser is a Compex pro 102F (Coherent Inc., USA) which produces a KrF (248nm) UV laser at a pulse rate from 1 to 10 Hz and energy up to 360 mJ. The sample was heated by a 980 nm IR Diode laser (Dual Signal Tech Corp., Taiwan) with a maximum power of 120 W which can heat the sample up to 1000°C in a vacuum.

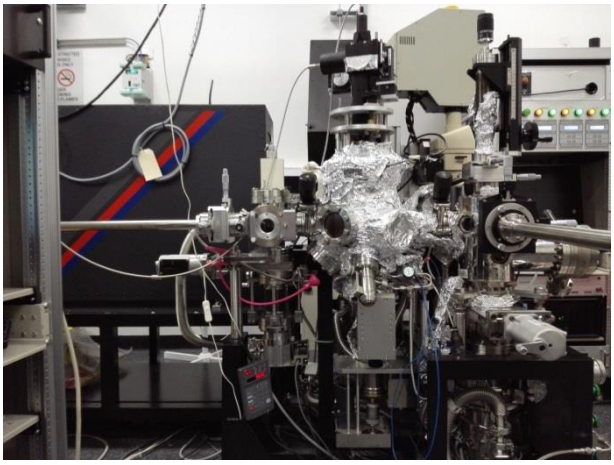

**Figure 3.1** Combination Vacuum System (Model: PA-LMLP-1001) produced by Pascal Co. Ltd., Japan.

### 3.2.2 Substrate Preparation

The substrate of the film is a single crystal of $SrTiO_3$ (Shinkosha, Japan) with a size of 15×15×0.5 mm. The (001) orientated substrates with a miscut angle of ~ 1 ° are polished and pre-etched to ensure the surface is flat and Ti-O terminated. The AFM image (**Figure 3.2**(a)) shows the stepped nature of the virgin surface. Each step in the AFM image represents one unit cell layer of the STO crystal. The substrate is cut into small pieces, usually 5×5mm, and is sonicated in 100 % isopropyl alcohol for 5 minutes to remove all the organic adsorbates on the substrate surface. After being dried in air, the sample is then mounted to a SiC block with silver paste and heated on a hot plate at about 80°C for more than 5

minutes to remove the solvent. The SiC block along with the attached substrate is then mounted to the sample holder and loaded into the chamber. The system is pumped to $10^{-6}$ Torr before it starts heating.

In order to obtain smooth steps on the surface of the substrate, a pre-annealing process is introduced. The substrate is heated (with a 980nm IR laser) to 800 °C and held in 100 mTorr Oxygen ambient for 30 mins. During the pre-annealing, the surface of the STO is reconstructed due to the rapid surface diffusion at high temperature and the steps are smoothened.[1] Near perfectly straight steps are accrued after the pre-annealing, as shown in **Figure 3.2**(b).

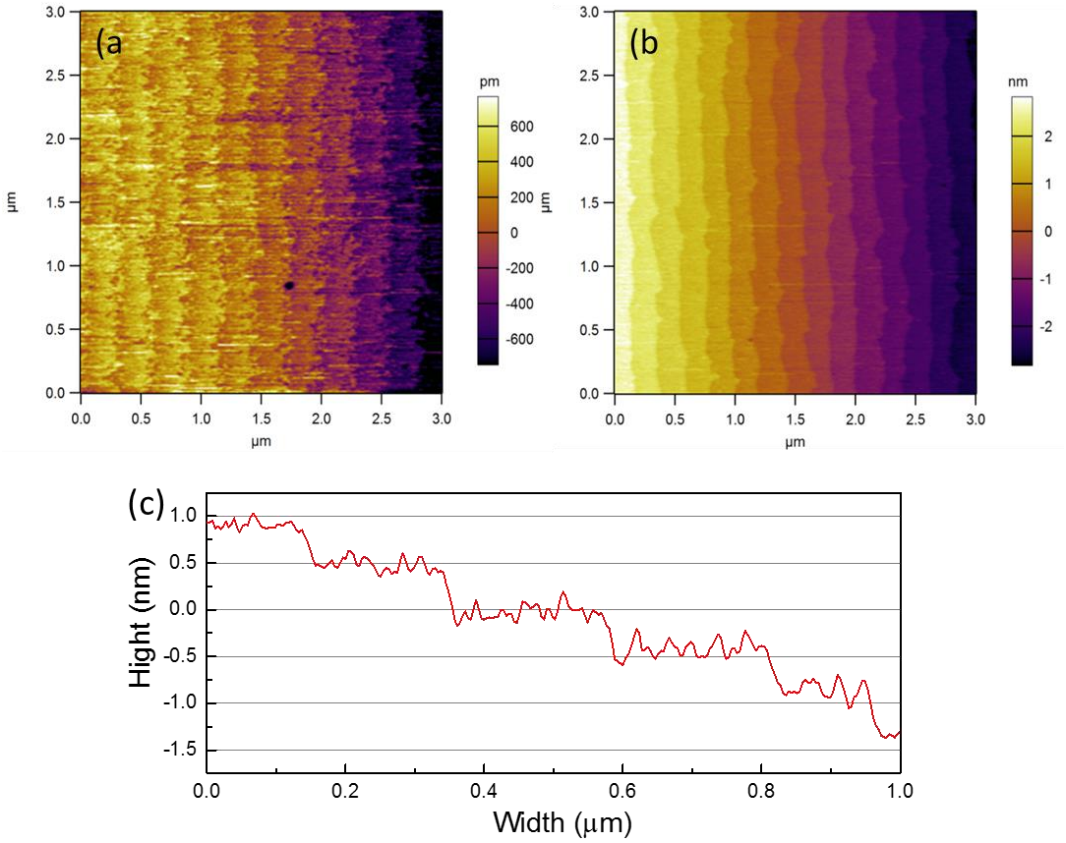


**Figure 3.2** AFM images of STO substrate (a) before annealing and (b) after annealing. (c) AFM Cross-section height of STO substrate after annealing.

## 3.2.3 FVO Film Growth and Optimization

The primary parameters of the PLD process requiring optimization are substrate temperature, ambient pressure, target composition (and density), laser fluence and the distance between target and substrate. The target we used in the

deposition is a mixed phase ($Fe_2O_3$ and $VO_2$) target, supplied by Kurt J. Lesker, USA, with a density of 2.9 g/cc and purity of 99.9 wt%. The target to substrate distance is about 50mm as set by the chamber geometry. The laser is focused on the target with a fluence of 2J/cm$^2$. The most critical parameters that influence the phase of the final product are ambient pressure and substrate temperature.

### 3.2.3.1 Ambient Pressure

The first step to determine the optimized growth condition is to find out the correct pressure. A test of the growth of a set of FVO films with different Oxygen pressures (400 mTorr, 200 mTorr, 100 mTorr and $10^{-5}$ Torr) is carried out. The other parameters are listed in **Table 3.1**.

| Oxygen Pressure | Substrate Temperature | Laser energy | Frequency | Number of Pulses | Cooling rate |
|---|---|---|---|---|---|
| $10^{-5}$Torr ~400mTorr | 500°C ~700°C | 200mJ | 2Hz | 2400 | 30°C/min |

**Table 3.1** Parameters of the growth.

As shown in **Figure 3.3**(a~c), the topographic images of the films grown in 100 mTorr, 200 mTorr and 400 mTorr show that the films are not uniform. At least two kinds of structures, streak like and block like, can be observed which indicated the phase separation of FVO. This is confirmed by the XRD θ-2θ scan data. As shown in **Figure 3.4**, the XRD patterns of the samples grown in Oxygen ambient show only peaks of secondary phases, such as $V_2O_5$, $V_2O_3$ and $Fe_2O_3$. Obviously, the $Fe^{2+}$ and $V^{3+}$ ions are oxidized and form oxides with higher valance status ions, $Fe^{3+}$ and $V^{5+}$.

The sample grown in vacuum ($10^{-5}$ Torr) has a uniformed surface, as shown in **Figure 3.3**(d), and a strong peak of FVO(400) in the XRD pattern with little evidence of a secondary phase. Hence, for the spinal FVO, the best

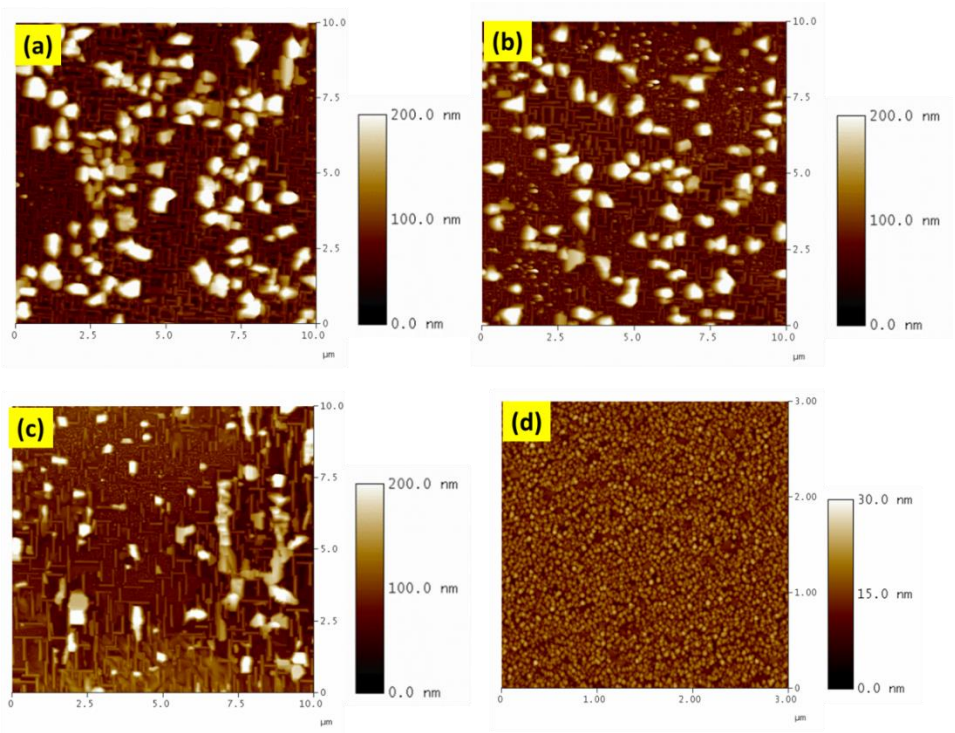


**Figure 3.3** Topographic images of FVO films grown under (a) 100 mTorr, (b) 200 mTorr, (c) 400 mTorr and (b)1E$^{-5}$ Torr Oxygen ambient.

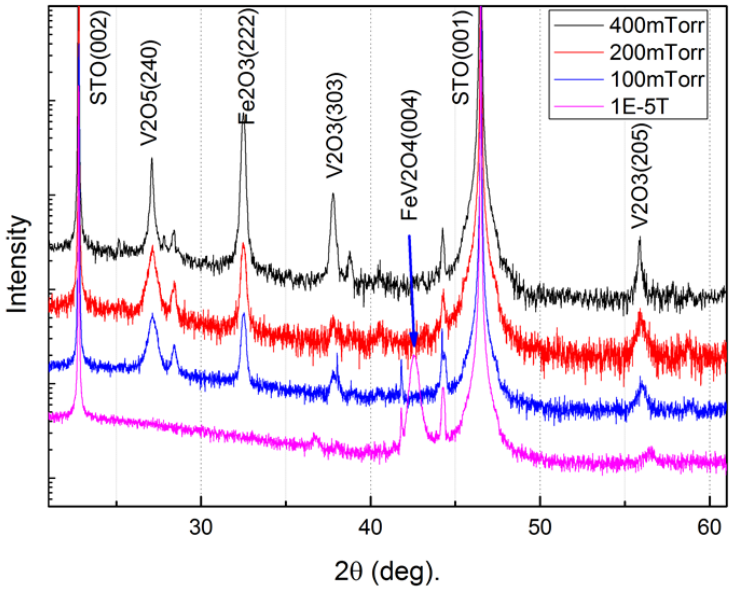


**Figure 3.4** XRD 2θ scan patterns of FVO films grown under different $O_2$ pressure.

deposition pressure in our system is $10^{-5}$ Torr (in vacuum). At this low pressure, the tendency of the change to higher valance status of the ions is suppressed, so that a pure phase FVO film is acquired.

### 3.2.3.2 Substrate Temperature

To further optimize the growth of the FVO film, the effect of the substrate temperature is studied. Three samples are synthesized at 700 °C, 600 °C and 500 °C under the pressure of $10^{-5}$ Torr. The topographic images of the samples are shown in **Figure 3.5** and the Rms of the samples is shown in **Table 3.2**. As we can see, the film grown at lower temperature is smoother than the others and the Rms drops down to 1.2 nm at 500 °C. At higher temperature, the grain growth rate is higher than the nucleation rate, hence larger grains are formed at higher temperature and lead to a higher roughness.

| Temperature(°C) | 700 | 600 | 500 |
|---|---|---|---|
| Rms(nm) | 8.869 | 3.392 | 1.246 |

**Table 3.2** Rms of the FVO film grown at different temperatures**.**

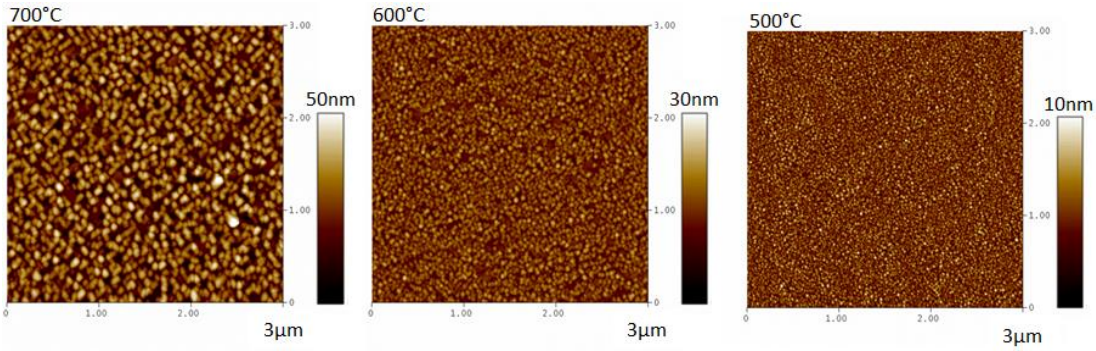


**Figure 3.5** Topographic images of FVO films grown at different temperature.

**Figure 3.6** shows the XRD pattern of the three samples. All samples show a strong FVO(004) peak and with the decreasing of the temperature, the little secondary phase peak around 57 ° disappeared. A clean pattern with only FVO(004) and substrate peaks is obtained from the 500°C sample. The impurity peak found in high temperature samples is suspected to be $V_2O_3$ which is caused by the oxidation of the V ion as previously discussed. The lower temperature suppressed the oxidation.

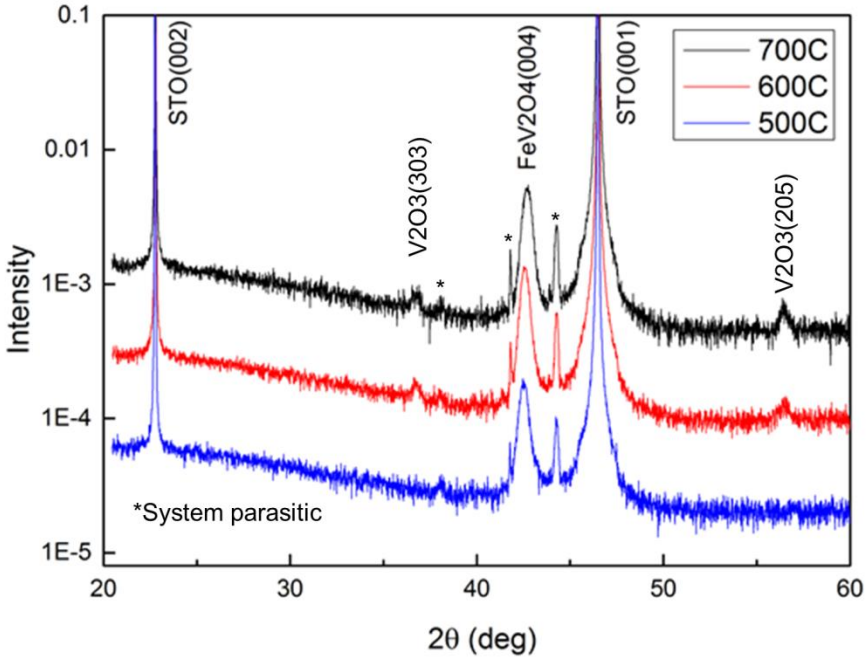


**Figure 3.6** XRD 2θ scan patterns of FVO films grown at different temperature.

## 3.3 Structural Characterization

In order to have a close study of the FVO films, an 80-nm-thick FVO is grown on STO(001) substrate with the optimized condition determined by previous experiments. The growth parameters are listed in **Table 3.3**. Note that to avoid the oxidation of Fe and V ions, the sample is rapidly cooled to room temperature within 5 mins after the deposition.

| Oxygen Pressure | Substrate Temperature | Laser energy | Frequency | Number of Pulses | Cooling rate |
|---|---|---|---|---|---|
| $10^{-5}$Torr | 500°C | 200mJ | 2Hz | 4800 | 100°C/min |

**Table 3.3** Parameters of the growth.

Local Energy-dispersive X-ray Spectroscopy (EDS) mapping were employed to investigate the chemical component of the film (Taken by Ms. Yanyu Zhou). The mapping images of the cross-section of the film are shown in **Figure 3.7**, which confirms the presence of Fe and V ion in the film area, as well as the clear interface between the film and substrate.

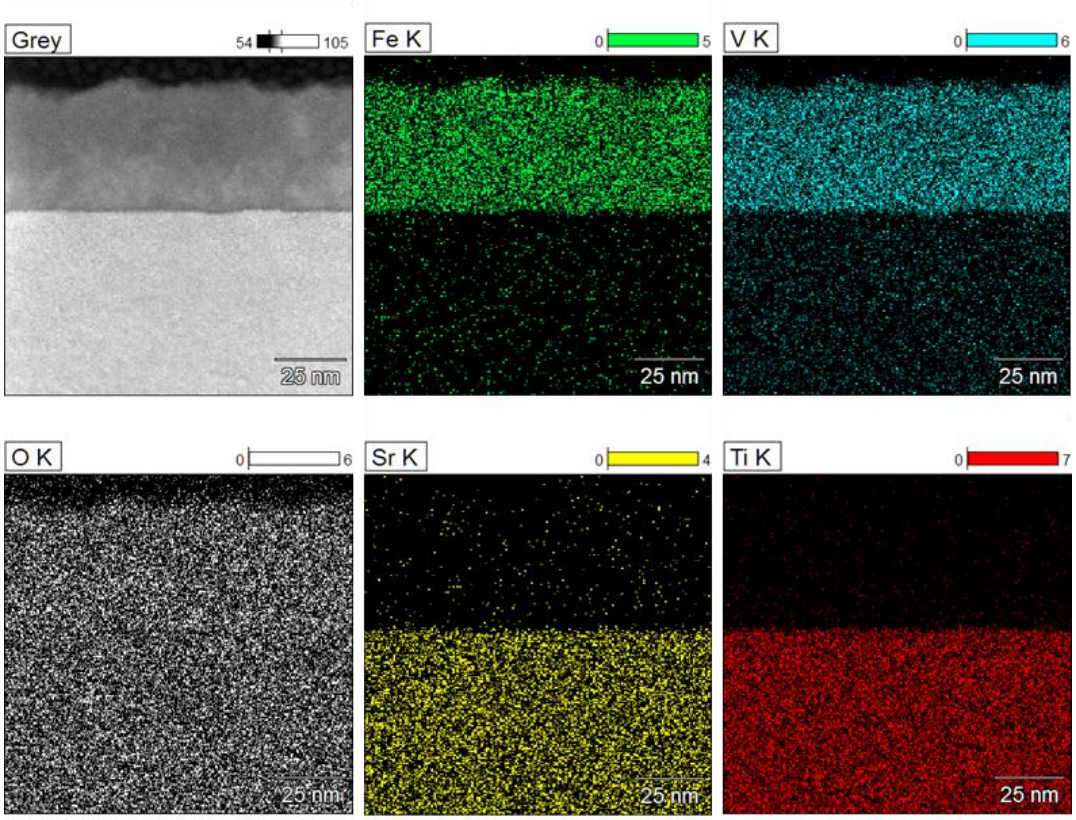


**Figure 3.7** Local Energy-dispersive X-ray spectroscopy (EDS) mapping of an 80-nm-thick FVO/STO film.

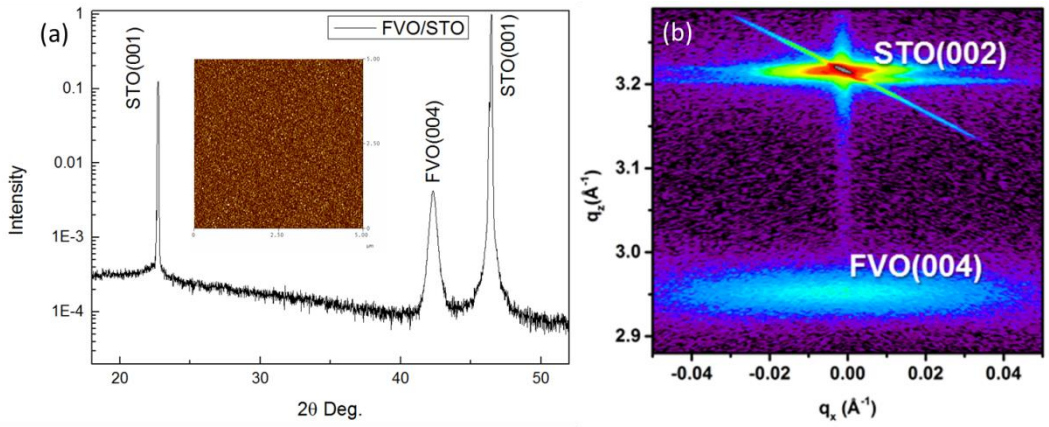


**Figure 3.8** (a) XRD θ-2θ pattern of an 80-nm-thick FVO/STO sample, inset: AFM image. (b) Reciprocal space map (RSM) of the sample around STO (002) peak.

The XRD θ-2θ pattern and reciprocal space map (RSM) of the sample are shown in **Figure 3.8**(a,b). As with previous samples, the θ-2θ scan shows a clear single phase pattern with a very intense FVO(004) peak without any secondary phase. We also find that the FVO(004) peak in the RSM is broadened along the $q_x$

axis, which indicates that the grains of the film are slightly tilted and probably form a mosaic-like texture. From the AFM figure, shown in the inset of **Figure 3.8**(a), low angle grain boundaries are observed which can support our assumption. The tilting of the grains is a stress relaxation mechanism, since the lattice mismatch between our film and substrate is large, about 8 % at room temperature, with bulk lattice parameters of STO and FVO at 3.906 Å[2] and 8.460 Å,[3-4] respectively.

To closely study the stress and its relaxation mechanism, the peak positions and calculated out-of-plane lattice parameters of the samples grown at different temperatures are listed in **Table 3.4**. A shifting of the FVO (004) peak position with decreasing temperature can be observed. The 700 °C sample has almost the same lattice parameter as the bulk material[5], indicating that the film is fully relaxed. However, the low temperature sample has a slightly larger out-of-plane lattice parameter, which indicates that the film is partially relaxed and has a compressive stress. This FVO film perhaps relaxes through the tilting of grains.

| Dep. Temps.(°C) | 2θ(deg) | d-spacing(Å) | Lattice parameter(Å) |
|---|---|---|---|
| **700** | 42.692 | 2.117 | 8.469 |
| **600** | 42.572 | 2.123 | 8.492 |
| **500** | 42.512 | 2.126 | 8.503 |

**Table 3.4** The 2θ deg. of FVO (004) plane and out-of-plane lattice parameters of FVO films grown at different temperatures.

In order to further study the stress relaxation mechanism, Transmission electron microscopy (TEM) was employed (Carried out by Ms. Yanyu Zhou). A cross-section TEM specimen was prepared by conventional focused ion beam (FIB) and tripod polishing methods. High-resolution STEM images were taken using a JEOL JEM-ARM200F. **Figure 3.9**(a) shows a STEM cross-sectional bright-field image of the 80nm thick FVO/STO sample oriented down at the [100]-zone axis. Strain contrast is visible both at the interface and within the film, although no grain boundary is observed. Higher resolution bright-field and HAADF images at the FVO/STO interface are shown in **Figure 3.9**(b,c). A slight tilting of the lattice can be found in the HAADF image. A reduced fast-fourier transform (FFT) image of a

selected area encompassing both the FVO and STO regions is shown in **Figure 3.9**(d), which indicates the cube-on-cube epitaxial nature of the film, in which the in-plane of the FVO film is parallel to that of the STO, and the out-of-plane of the FVO film and STO are also parallel to each other.

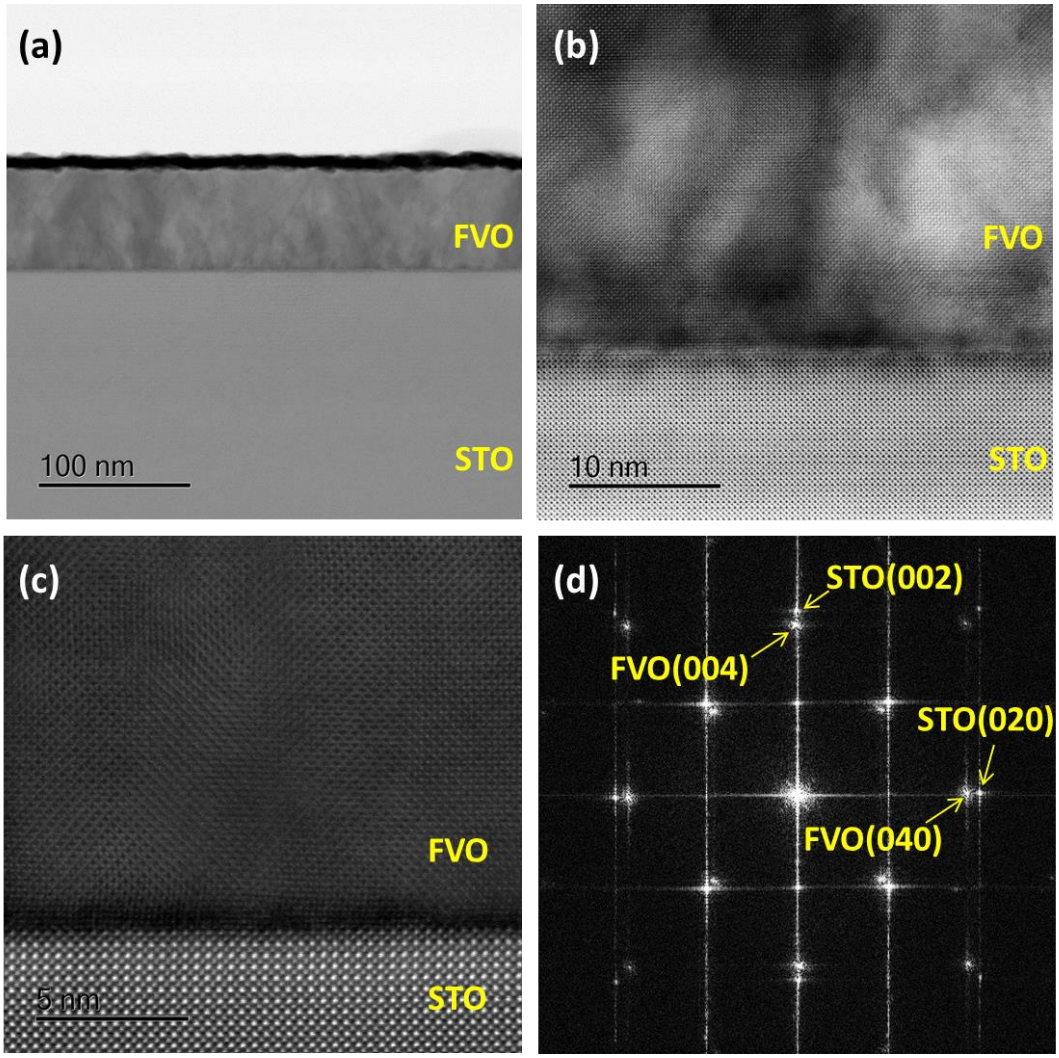


**Figure 3.9** Cross-sectional STEM bright-field images of FVO/STO at (a) low magnification and (b) high-magnification. (c) STEM HAADF image of FVO/STO at interface area. (d) Selected area electron diffraction image of the sample.

## 3.4 In-situ RHEED Study of the Growth Mechanism of FVO Films on STO Substrate

The nature of stress relaxation lies in the growth mechanism of the film. To study the growth mechanism, in-situ RHEED was employed during the deposition of the film. The RHEED patterns taken at different stages of the growth are shown in **Figure 3.10**. The growth of FVO on STO substrate can be summarised into 3 different stages:

First, growth following the perovskite structure as film is less than a few monolayers.

Second, the film reconstructs to spinel structure and relaxes the stress.

Third, the film keeps growing following the spinel structure. The details are explained below.

Before the start of the deposition, at the position marked (i), it shows a typical streak-like RHEED pattern of perovskite STO[6] with a maximum intensity. As the deposition starts, the intensity drops quickly accompanied with oscillations. This indicates that the film is growing layer by layer but the surface roughness increases quickly. At this stage, the position of the streaks in the RHEED pattern doesn't change, as shown in **Figure 3.10**(b,ii) which means that the film is following the perovskite structure and is still fully stressed. Because of the large lattice mismatch, a considerable amount of defects, such as dislocation and tilting, accumulate and increase the surface roughness. As the deposition continues and the thickness increases, the film can no longer hold a perovskite structure. Spinal structure starts to form and stress is relaxed, which can be proved by the shift of the RHEED pattern position, as shown in **Figure 3.10**(b,iii). The growth mode change from layer-by-layer (2D) to island growth (3D), evidence from the disappearing of the intensity oscillation and the spot-like RHEED pattern. The RHEED pattern, which changes to spots from streaks, is further evidence of the change of growth style. During this stage, the surface reconstructs and the smoothness increases leading to the increasing intensity. In the 3$^{rd}$ stage, the film keeps growing in a 3D

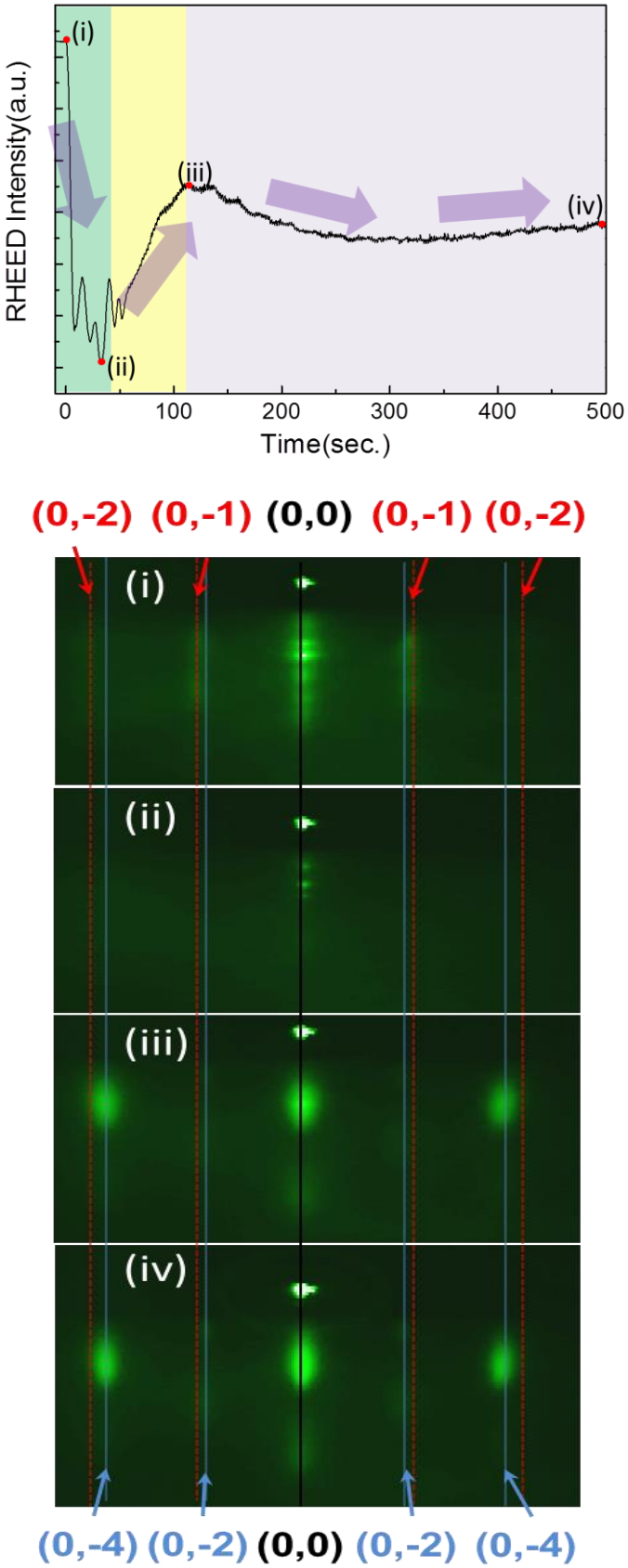


**Figure 3.10** (a) RHEED intensity vs time. (b) RHEED pattern taken at different stages during the deposition.

mode and the thickness increases, no significant change of the surface can be found.

The in-plane lattice parameter of the sample can be estimated with the equation as below,

$$a = \frac{\lambda L \sqrt{h^2 + k^2}}{t} \tag{3.48}$$

where $a$ is the lattice parameter, $\lambda$ is the wavelength of the electron beam, $L$ is the distance between the sample and phosphor screen and $t$ is the distance between the RHEED streaks/spots. Using the lattice parameter of the STO substrate as a reference, the in-plane lattice parameter of the FVO film is estimated to be 8.459 Å, which is almost the same as that of the bulk material. In this case, the film is fully relaxed.

## 3.5 Growth of Electrode Layer and the Integration with FVO Films

To investigate the electrical properties of the FVO film such as dielectric and ferroelectric properties, a conductive bottom electrode buffer layer is required. In this project, $SrRuO_3$ (SRO) is chosen for its high conductivity and excellent epitaxial growth[7] on STO substrate.

| Oxygen Pressure | Substrate Temperature | Laser energy | Frequency | Number of Pulses | Cooling rate |
|---|---|---|---|---|---|
| 100 mTorr | 680°C | 200mJ | 1Hz | 600 | 30°C/min |

**Table 3.5** Growth conditions of SRO film.

The growth conditions of SRO film are listed in **Table 3.5**. **Figure 3.11**(a) and **Figure 3.12** show the topographic image and XRD 2θ scan pattern of the SRO grown. The surface of the SRO thin film is very fine, such that clear and smooth steps can be observed; the XRD peaks of SRO (001) and (002) are sharp, and Laue fringes can be observed which indicate the high quality of the SRO film.

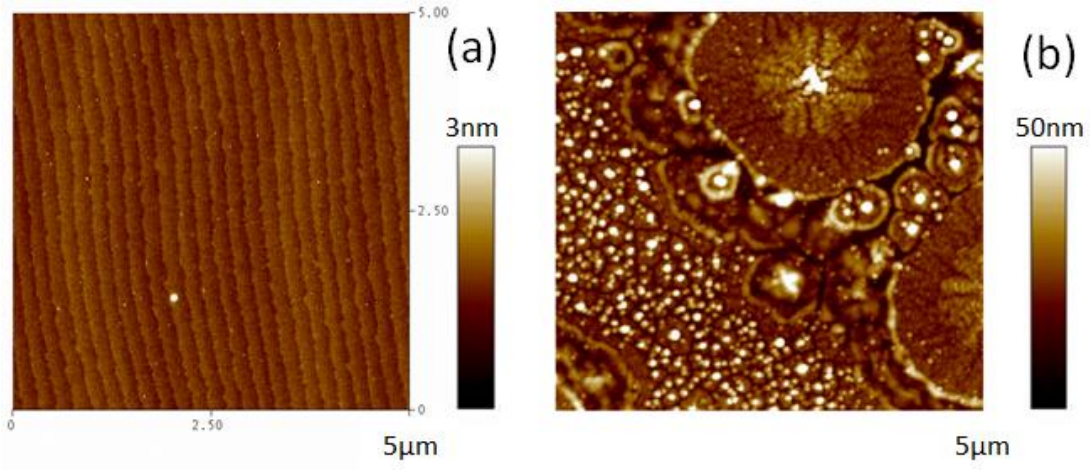


**Figure 3.11** Topographic images of SRO films (a) pre annealing, (b) post annealing.

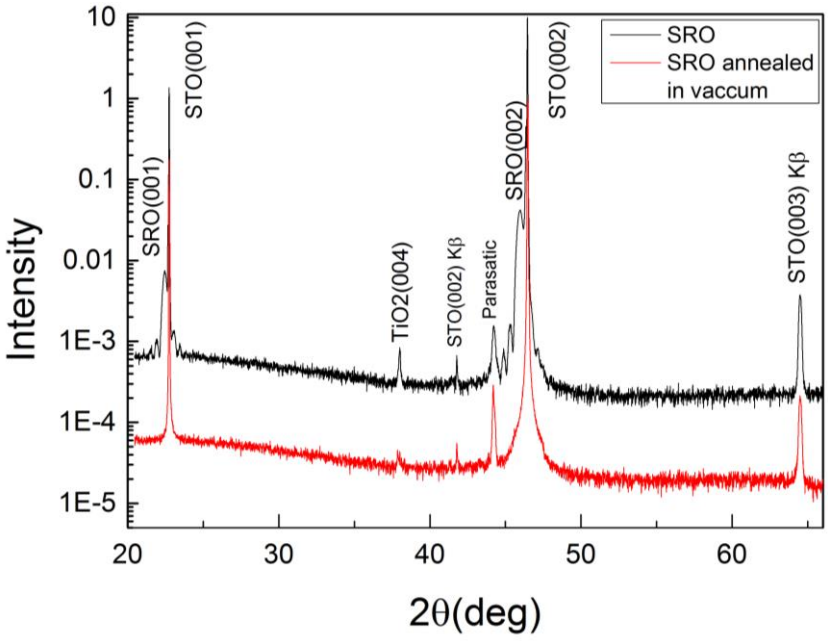


**Figure 3.12** XRD 2θ scan patterns of SRO film pre and post annealing in vacuum.

Although the SRO electrode buffer layer is successfully grown, the integration of SRO and FVO remains a problem as the two films need to be grown under different $O_2$ pressures. The process of FVO growth requires a vacuum environment, which may reduce the grown SRO film and make it decompose. To confirm this, the SRO sample is annealed in a vacuum at 500°C for 20 mins, which is the deposition time of FVO film, and then is checked by AFM and XRD. The results, in **Figure 3.11**(b) and **Figure 3.12**, show that the SRO film is completely decomposed and not a single peak can be found in the 2θ scan pattern.

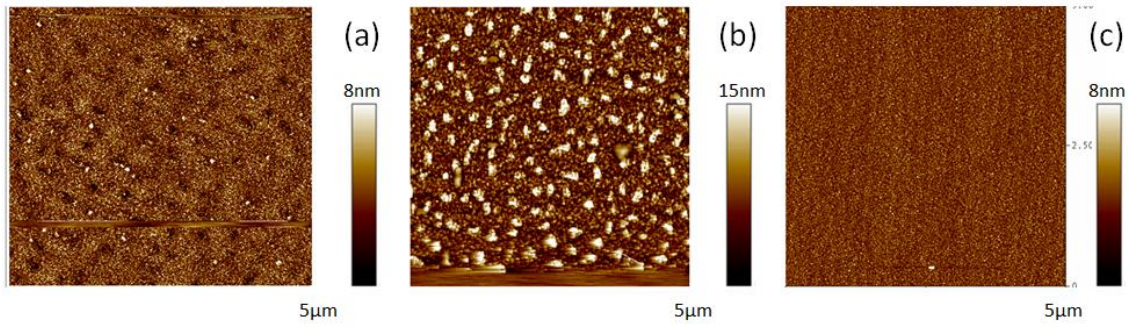


**Figure 3.13** Topographic images of FVO/SRO/STO films. (a) Cool down to 500 °C in 100 mTorr. (b) Cool down to 200 °C and then heat to 500 °C in 400 mTorr. (c) Cool down to 200 °C and then heat to 500°C in 100 mTorr.

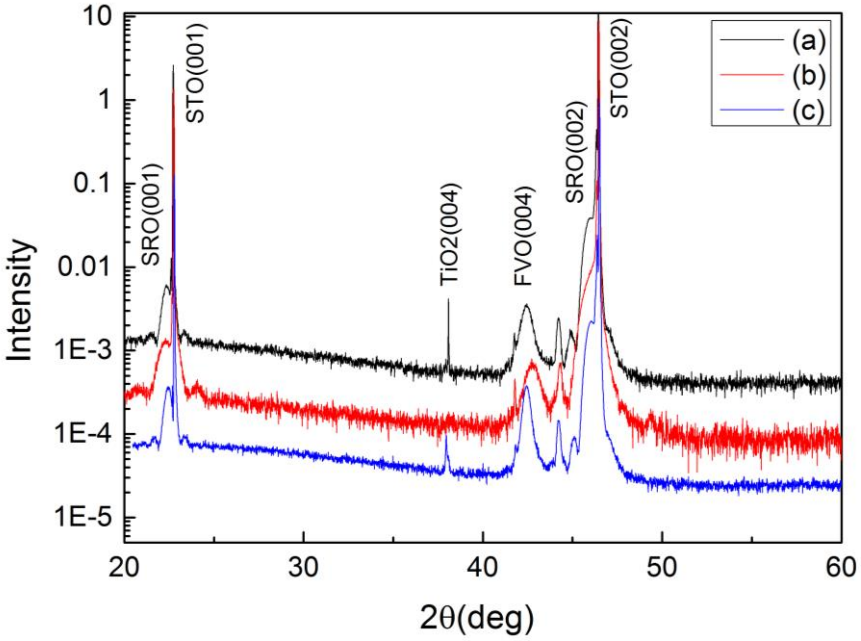


**Figure 3.14** XRD 2θ scan patterns of FVO/SRO/STO films. (a) Cool down to 500 °C in 100 mTorr. (b) Cool down to 200 °C and then heat to 500 °C in 400 mTorr. (c) Cool down to 200 °C and then heat to 500 °C in 100 mTorr.

To avoid the decomposition of SRO film, one needs to reduce the time that SRO is exposed in the vacuum. After the SRO is deposited, the sample is cooled from 700 °C (the deposition temperature of SRO) to 500 °C (the deposition temperature of FVO) in 100mTorr and pump down the chamber just before the growth of the FVO film. The result in **Figure 3.13**(a) shows that the SRO layer is slightly damaged and forms holes under the FVO layer. To stabilize the SRO layer, the cooling process is carried out as in the growth of single layer SRO film which is cool down the SRO film to 200 °C in 400 mTorr $O_2$ pressure. Then the temperature is raised to 500 °C, pump down the chamber and do the FVO deposition. As shown in **Figure 3.13**(b), secondary phase particles are observed, indicating that the FVO is slightly oxidized which may be caused by the excess oxygen in SRO film during the cooling process between the two depositions. Then the $O_2$ pressure of the cooling is changed to 100 mTorr, the same as the deposition pressure, so that there should be limited excess oxygen in SRO and it will not oxidize the incoming FVO film. As expected, the film is smooth and the XRD θ-2θ scan pattern shows both clear SRO [001] peaks and FVO (004) peak.

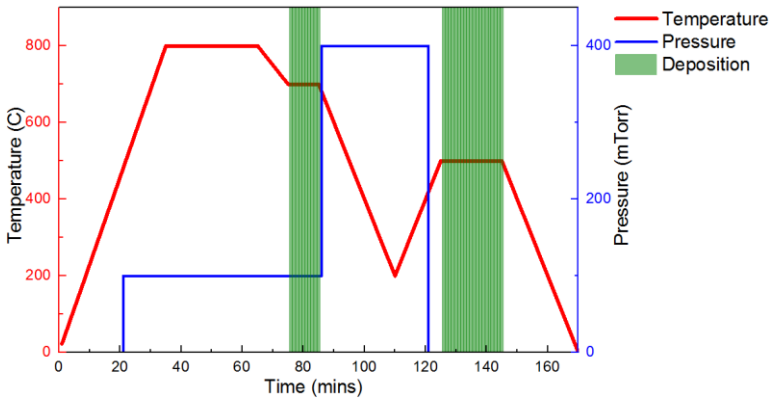


**Figure 3.15** Chart of temperature and pressure control during the film deposition.

By adding a cooling process under 100 mTorr $O_2$ pressure between two layers of deposition, the SRO electrode layer is successfully integrated with the spinel FVO layer.

LSMO, a widely used bottom electrode material, is also chosen in this project because it offers clean interfaces with high epitaxial quality, and additional magneto-resistance capability which may interact with FVO and possibly show interesting results.

The growth conditions of LSMO are: 100 mTorr $O_2$ pressure, 200 mJ laser energy, 750 °C deposition temperature and cooling down in 100mTorr. The X-ray θ-2θ scan and AFM topographic data are shown in **Figure 3.16**. The LSMO film shows clear [001] peaks with no secondary phase. And the surface of the film is stepped, with an Rms of 0.275 nm, which means that the film growth is step flowed with high epitaxial quality.

To integrate FVO and LSMO films, a strategy similar to that which we used on FVO/SRO film is applied. After the deposition of the LSMO film, the sample is cooled to 200 °C under 100 mTorr $O_2$ pressure, and then the chamber is pumped to $1E^{-5}$ T. After the pumping, the FVO is grown. **Figure 3.17** shows the X-ray θ-2θ scan and AFM topographic data of FVO/LSMO/STO. Both the FVO (004) peak and LSMO [001] peaks are clearly shown in the XRD pattern. The surface of the film is smooth with an Rms of 1.9 nm.

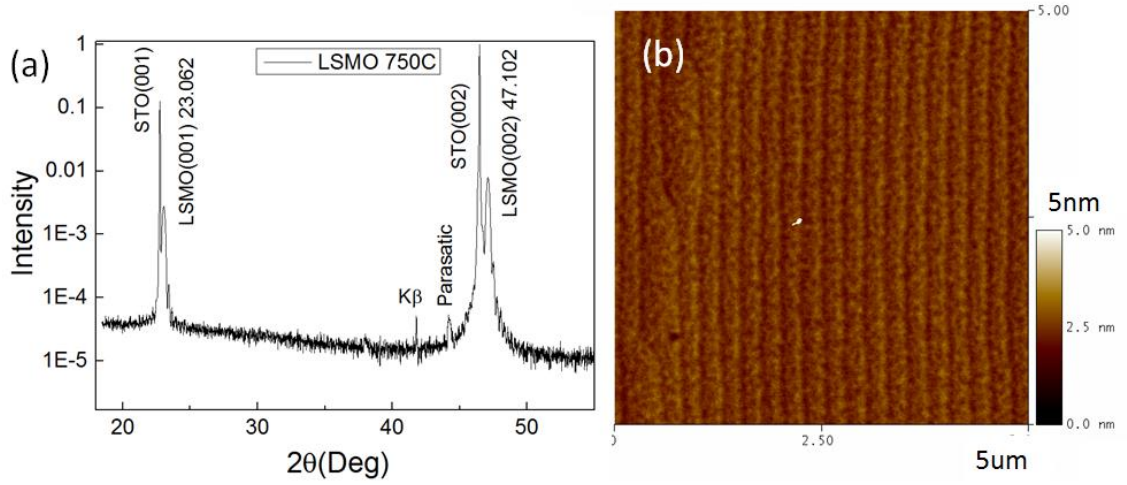


**Figure 3.16** (a) XRD θ-2θ scan pattern of LSMO/STO sample. (b) Topographic image of LSMO/STO sample.

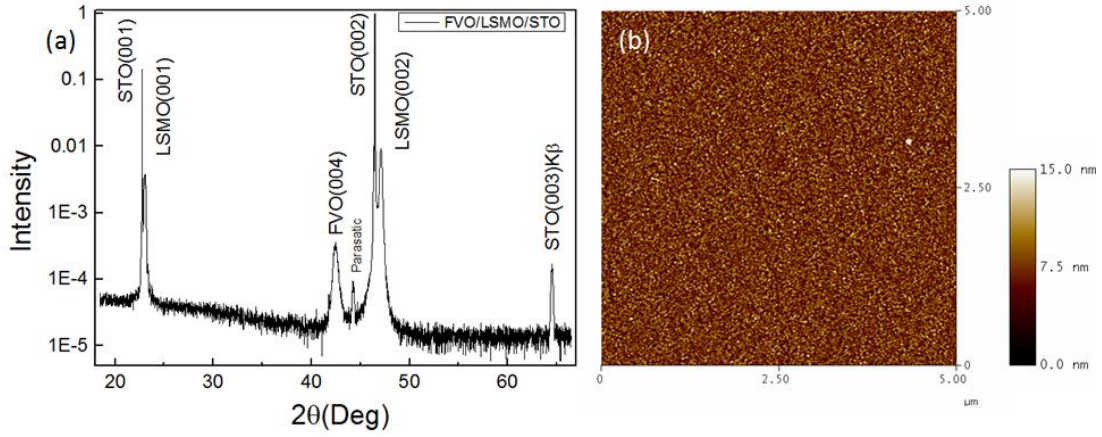


**Figure 3.17** (a) XRD θ-2θ scan pattern of FVO/LSMO/STO sample. (b) Topographic image of FVO/LSMO/STO sample.

## 3.6 Summary

In summary, this thesis has achieved the first successful synthesis of epitaxial FVO films on STO (001) substrate by reducing the ambient oxygen pressure during the deposition. The deposition temperature affects the grain size of the film as well as the residual strain. A higher deposition temperature leads to larger grains and lower strain, and a lower temperature smoothes the film surface and increases the compressive strain. By introducing a cooling step in between, the phase pure FVO films are also obtained on SRO and LSMO buffered substrates as well as Nb doped STO substrates. The cross-session TEM and SAED images show a cubic-on-cubic epitaxial relationship between the FVO film and the STO substrate, and the film is nearly fully relaxed through misfit at the interface and lattice tilting. The growth of the FVO film follows a 2D to 3D mode as observed by in-situ RHEED.

References

[1] M. Lippmaa, K. Takahashi, S. Ohashi, N. Nakagawa, T. Sato, M. Iwatsuki, H. Koinuma, M. Kawasaki,Dynamics of SrTiO3 surface during wet etching and high-temperature annealing, Ferroelectrics 1999, 224, 801.
[2] L. W. Martin, Y. H. Chu, R. Ramesh,Advances in the growth and characterization of magnetic, ferroelectric, and multiferroic oxide thin films, Mat. Sci. Eng. R 2010, 68, Iii.
[3] T. Katsufuji, T. Suzuki, H. Takei, M. Shingu, K. Kato, K. Osaka, M. Takata, H. Sagayama, T. H. Arima,Structural and magnetic properties of spinel FeV2O4 with two ions having orbital degrees of freedom, J. Phys. Soc. Jpn. 2008, 77.
[4] S. Kawaguchi, H. Ishibashi, Y. Kubota,Iron Excess Effect in Structural and Magnetic Properties of Vanadium Spinel FeV2O4, J. Phys. Soc. Jpn. 2014, 83.
[5] G. J. MacDougall, V. O. Garlea, A. A. Aczel, H. D. Zhou, S. E. Nagler,Magnetic order and ice rules in the multiferroic spinel FeV2O4, Phys. Rev. B 2012, 86.
[6] J. A. Moyer, R. Gao, P. Schiffer, L. W. Martin,Epitaxial growth of highly-crystalline spinel ferrite thin films on perovskite substrates for all-oxide devices, Sci. Rep.-Uk 2015, 5.
[7] C. B. Eom, A. F. Marshall, Y. Suzuki, T. H. Geballe, B. Boyer, R. F. W. Pease, R. B. Vandover, J. M. Phillips,Growth Mechanisms and Properties of 90-Degrees Grain-Boundaries in YBa2Cu3O7 Thin-Films, Phys. Rev. B 1992, 46, 11902.

# CHAPTER FOUR

# 4 MAGNETIC PROPERTIES OF IRON VANADATE FILMS

## 4.1 Synopsis

In the previous chapter, high quality epitaxial FVO films on $SrTiO_3$(001) were obtained by the PLD technique and the film structure was characterized by XRD and TEM. This chapter discusses the use of X-ray absorption spectroscopy (XAS) and X-ray magnetic circular dichroism (XMCD) to determine the electron and spin states of the FVO films. A normal spinel structure of the FVO films is confirmed by determining the valance states of Fe and V ions as measured by XAS, as the Fe ions are nearly divalent and the V ions are trivalent. A small amount of excess $Fe^{3+}$ is also found in the system, which possibly substitutes for the $V^{3+}$ located on the tetragonal site. The spin states, magnetic moments, of the two transition-metal ions were also measured by XMCD. The ferrimagnetic ordering of the film was found to be in good agreement with the ordering of the bulk materials.[1-2] Next, the magnetic hysteresis loops of film were taken at different temperatures. The M-H loops show that the film has a strong magnetic anisotropic with stronger coercive field and magnetization along the out-of-plane axis. Lastly, magnetic force microscopy (MFM) measurement to probe the magnetic domains and the switching behaviour of the films are discussed. By applying a magnetic field higher than 3 T, the domains can be switched. This is the first demonstration of direct visualization of the domains and their switching behaviour in FVO thin films.

## 4.2 Experimental Details

X-ray absorption spectroscopy (XAS) and X-ray magnetic circular dichroism (XMCD) were employed to investigate the electronic and spin structure of FVO thin films. As there is no need for an electrode layer in the XAS and XMCD measurements, a single layer of 100-nm-thick FVO/STO sample was used. The measurements were executed at the 11A Dragon Beamline of National Synchrotron Radiation Research Centre (NSRRC) with the total electron yield mode (Carried out by Dr. Qing He). The sample was measured at the temperature range of T = 80 ~ 220 K. The pressure of chamber was better than $1\times10^{-9}$ Torr. The XMCD spectra are analysed from the difference between the absorption spectra measured with 80 % right circularly polarized X-rays at ± 1 T of external magnetic fields.

A quantum design magnetic property measuring system (MPMS) Superconducting Quantum Interference Device (SQUID) dc magnetometer was employed to measure the **M-T** curves and **M-H** loops, OOP and IP at low temperatures (Carried out by Dr. Kumar Suresh).

In the Magnetic force microscopy (MFM) imaging, a 100-nm-thick FVO/STO sample was measured with a cryogenic scanning probe microscope (AttoDRY 1000, Attocube, carried out by Mr. Dohyung Kim). Commercial magnetic cantilevers (Multi75M-G, BudgetSensors) were used, as shown in **Figure 4.1**, to capture out-of-plane MFM images at 10K as a function of magnetic field after zero field cooling to ~ 4 K. The MFM signals were taken at a constant height (50 nm) mode at 75 kHz resonance frequency. Measurements were performed in 20 mbar of He exchange gas. The scan speed was 3 µm/s.

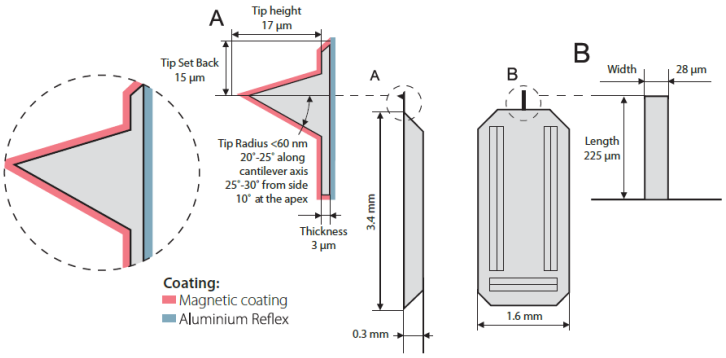


**Figure 4.1** Details of the MFM tips used in the measurements.

## 4.3 Results and Discussions

### 4.3.1 X-ray Absorption Spectroscopy

The XAS spectrum along the Fe $L_{3,2}$ edge, taken at 220 K, is shown in **Figure 4.2**. It is divided into two spin-orbit parts, namely $L_3(2p3/2)$ and $L_2(2p1/2)$. To determine the valance states of Fe ions, the XAS spectrum of our sample is compared to those of Fe ions in different states including FeO, $F_3O_4$, α-$Fe_2O_3$ and Fe metal. As we can see, although there are two peaks at the $L_3$ edge of the FVO spectrum, one is correlated to the $Fe^{2+}$ state and the other to the $Fe^{3+}$ state. The overall line shape of the FVO spectrum is more like the divalent FeO shape. Comparing to those of the well-known mixed valance $Fe_3O_4$ and trivalent $Fe_2O_3$, the $Fe^{2+}$ peak is stronger and the $Fe^{3+}$ peak of FVO film is quite weak, indicating that the Fe ions in our sample are mainly divalent. The $Fe^{3+}$ signal may come from some oxidised phase at the sample surface because $Fe^{2+}$ ions are very easily oxidised,[3] and the quantity is so small that it cannot be detected by conventional structure investigating techniques, such as XRD and TEM. Another possible situation is that some of the excess $Fe^{3+}$ ions in the system may substitute $V^{3+}$ ions and sit in the tetragonal site, forming a $Fe^{2+}Fe^{3+}_xV^{3+}_{(2-x)}O_4$ compound. We will further discuss the valance states of Fe ions in the following chapters. **Figure 4.3** shows the V $L_{3,2}$ edge XAS spectrum of FVO along with some other V XAS spectra of different V oxides. It is observed that the line shape of V $L_{3,2}$ edge XAS spectrum is very similar to that of $V_2O_3$[4] which has a trivalent V ion valance state, but is different from those of $VO_2$[5] and $V_2O_5$[4] with higher valance states. This suggests

that V ions in our FVO films are nearly trivalent. Considering the stoichiometry of the film, as there are $Fe^{3+}$ components observed but no $V^{2+}$ is found in the XAS spectra, it is likely that there are excess $Fe^{3+}$ ions in the sample, which consequently formed $Fe^{2+}(Fe^{3+}_xV^{3+}_{(2-x)})O_4$. This is consistent with the previously reported bulk materials. [6-8]

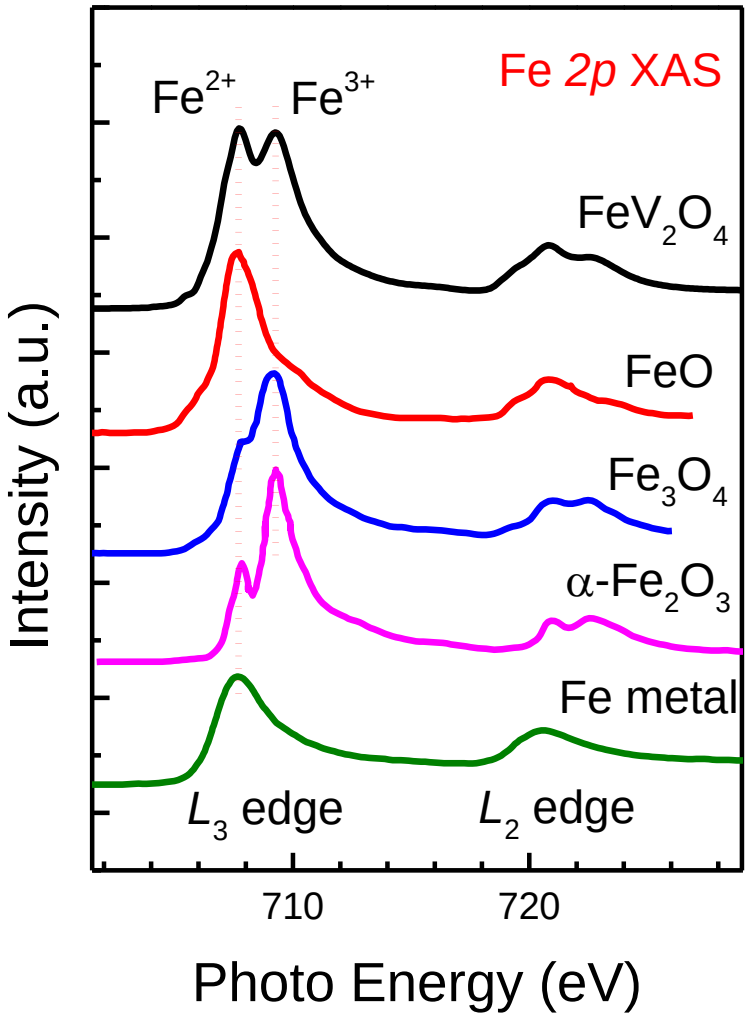


**Figure 4.2** The Fe $L_{3,2}$ edge XAS spectra of $FeV_2O_4$, FeO (Ref.[9]), $Fe_3O_4$(Ref.[9]), $Fe_2O_3$(Ref.[9]) and Fe metal(Ref.[9])

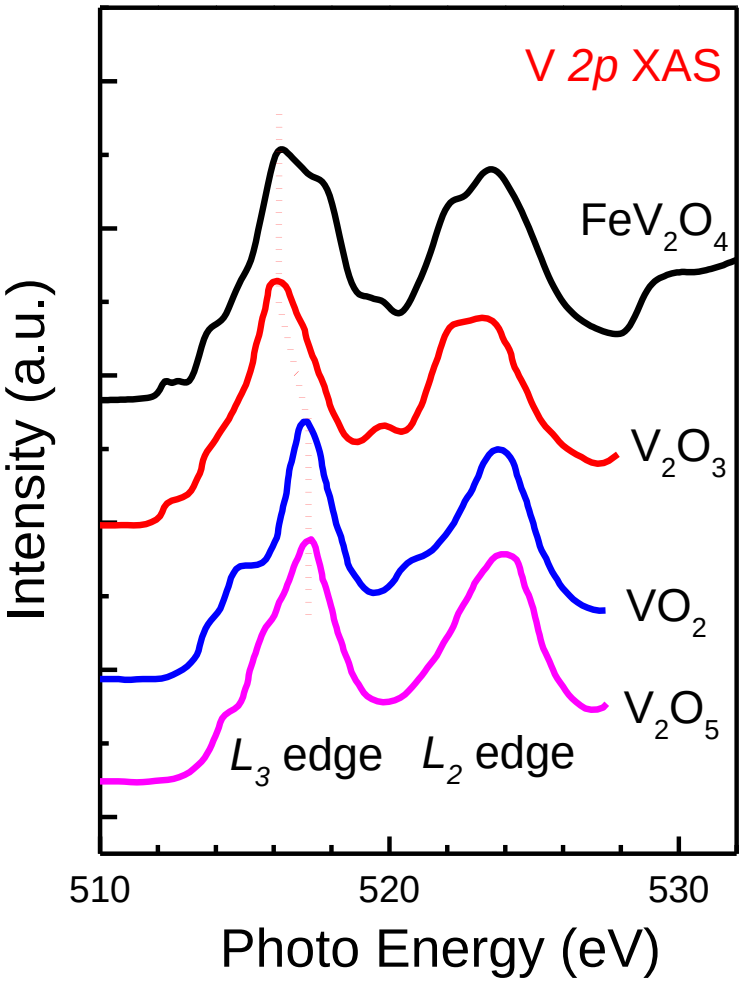


**Figure 4.3** The V $L_{3,2}$ edge XAS spectra of $FeV_2O_4$, $V_2O_3$[4], $VO_2$[5] and $V_2O_5$[4].

### 4.3.2 X-ray Magnetic Circular Dichroism

The XMCD spectra are analysed from the difference between the absorption spectra measured with 80 % right circularly polarized X-rays at ± 1 T of external magnetic fields. **Figure 4.4** shows the Fe $L_{3,2}$ edge XAS spectra taken with the magnetic fields parallel ($\mu_+$)(red line) and antiparallel ($\mu_-$)(black dots) to the helicity vector of the x-ray. The difference between the two spectra, which is the XMCD, is shown in the blue line alone with the integration of it (purple dots).

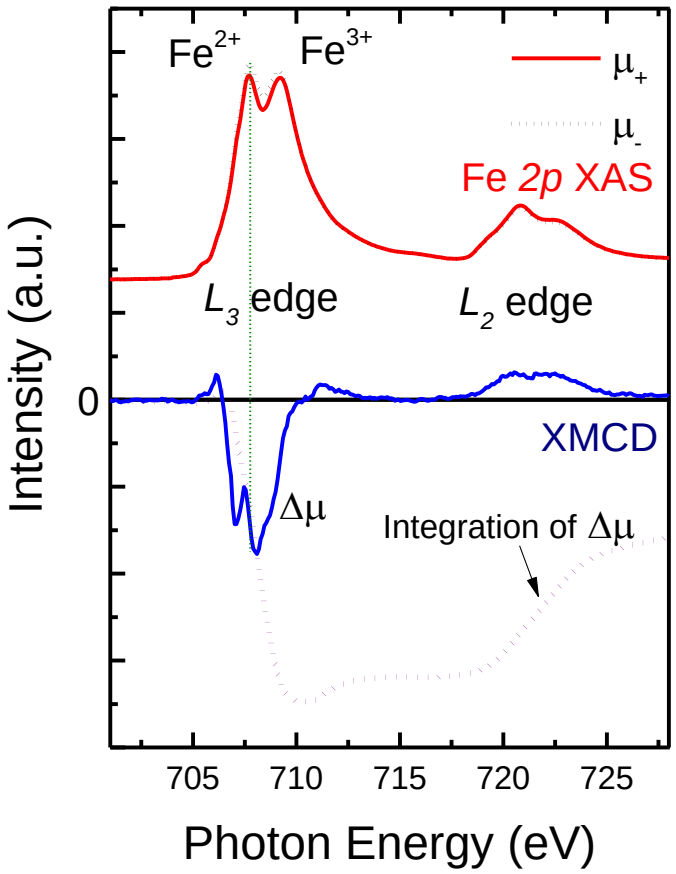


**Figure 4.4** The Fe $L_{3,2}$ edge XAS spectra ($\mu_+$ in red line and $\mu_-$ in black dots) taken with ±1T applied magnetic fields. The difference between the two XAS spectra ($\Delta\mu = \mu_+ - \mu_-$), is the XMCD spectrum.

The XMCD exhibits a double-peak structure at $h\nu = 706 \sim 708$ eV and a pre-edge peak, which makes it different from the single peak $L_3$ part in Fe metal as well as that of the mix-valanced $Fe_3O_4$. The multiple structures in our FVO sample reflect the localized nature of Fe cd electrons. The integration of $\Delta\mu$ is shown in the figure, the net negative value, and indicates a net magnetic moment of Fe ions.

As shown in **Figure 4.4**, the main contribution of the $\Delta\mu$ (XMCD) comes from the divalent $Fe^{2+}$ XAS peak, but not from the trivalent $Fe^{3+}$. This suggests that the origin of the magnetic moments of Fe ions arise mainly from the divalent $Fe^{2+}$ states, but not from the trivalent $Fe^{3+}$ states. However, a small shoulder at the right side of the main peak, which arises from the corresponding $Fe^{3+}$ XAS peak is

observed. This may be attributed to those $Fe^{3+}$ sitting in the tetragonal sites of the spinel crystal. To further examine the result, we compared the XMCD spectrum of our sample with that of the well-known mixed-valanced $Fe_3O_4$ data, shown in **Figure 4.5**. As we can see, the $L_3$ edge XMCD spectrum of $Fe_3O_4$[10] shows a triple peak structure originating from $Fe^{2+}$ (ochta.), $Fe^{3+}$(tera.) and $Fe^{3+}$(ochta.), respectively. The peak position in the XMCD spectrum of our sample is very close to that of the $Fe^{2+}$ peak of $Fe_3O_4$, while no evidence of any $Fe^{3+}$ peaks can be found, indicating that the XMCD signal in our sample originates from the $Fe^{2+}$ states.

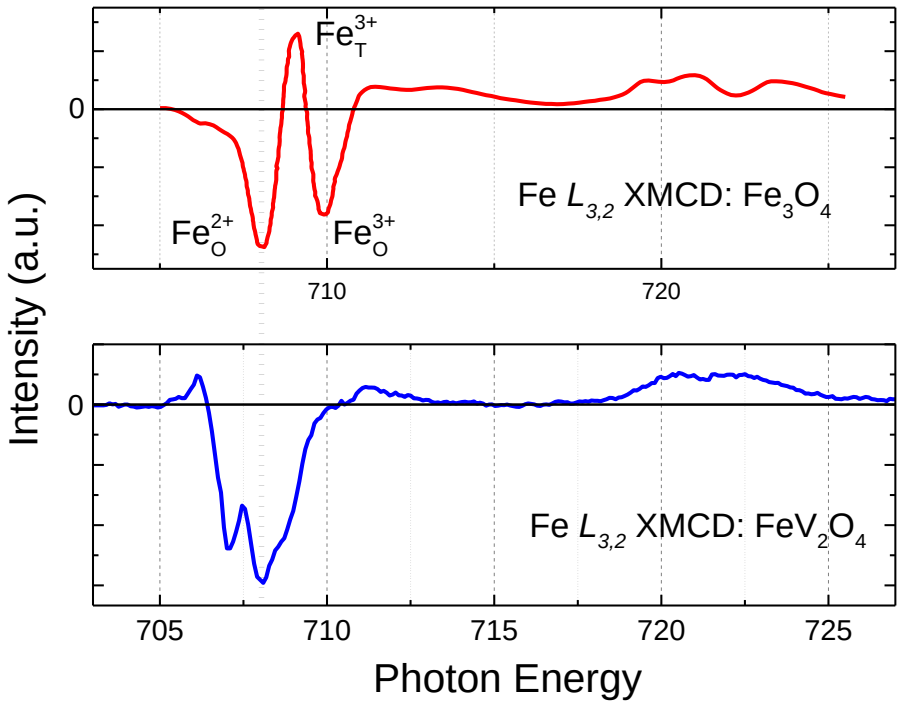


**Figure 4.5** Fe $L_{3,2}$ edge XMCD of $Fe_3O_4$ (adapted from Ref. [10]) and $FeV_2O_4$.

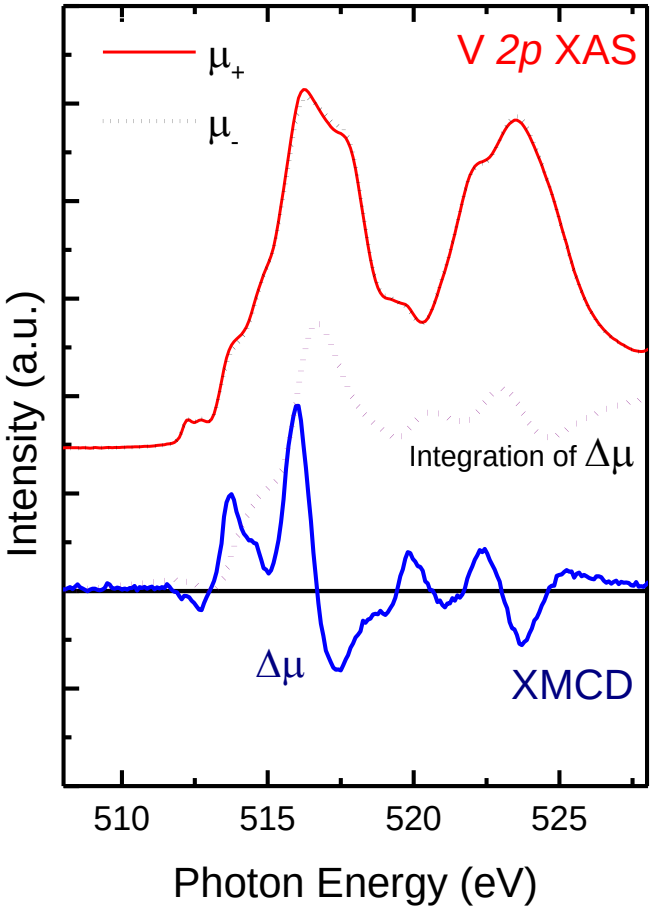


**Figure 4.6** The Fe and the V $L_{3,2}$ edge XAS spectra ($\mu_+$ in red line and $\mu_-$ in black dots) taken with ± 1 T applied magnetic fields. The difference between the two XAS spectra ($\Delta\mu = \mu_+ - \mu_-$), is the XMCD spectrum.

Similar to those of the Fe ions, the XMCD spectra of V $L_{3,2}$ edge is shown in **Figure 4.6** (blue line) as the difference between XAS spectra taken under different applied fields, $\mu_+$(red line) and $\mu_-$(black dots). The value of the main peaks of the XMCD is positive, resulting in a net positive integration of Δμ. Notice that the sign of the integrated Δμ is opposite as for Fe and V ions, which suggests that the direction of the magnetic moments of the two ions are antiparallel to each other, consistent to those which have been reported in other studies [1, 8].

The XMCD spectra were taken at different temperatures (80 K, 100 K, 140 K, 180 K and 220 K) to investigate the temperature dependence of the

magnetic moments of the FVO film. The spectra are shown in **Figure 4.7**. The line shape of the XMCD spectra are essentially similar at different temperatures while the intensity changes. The intensity of the main peaks of $L_3$ V (in red) and Fe (in black) XMCD signals as a function of temperature is shown in **Figure 4.8**. As the temperature decreases, the absolute values of the XMCD intensity increases from below 1% for Fe (0.5% for V) at 220 K to ~3.5% (1.8%) at 100 K, and then slightly decreases at 80 K for both Fe and V. The exact same shape (opposite sign) of temperature dependence XMCD intensity curve of Fe and V indicates a strong coupling between the Fe and V spins in the system, which share the same magnetic Curie temperature at ~250 K and Néel temperature $T_{N1}$ at ~120K. The magnetization vs. temperature curves, zero-field-cooled (ZFC) and field-cooled (FC), of the FVO film are shown in **Figure 4.9**. At the measured Néel temperature $T_{N1}$ (~ 120 K), which is slightly higher than that of the bulk material[1], magnetization increases sharply as temperature is decreased, and then decreases after reaching the maximum value at ~ 100 K. A small anomaly is observed at ~ 40 K, slightly lower than that of the bulk material, due to the ferrimagnetic-to-noncollinear ferromagnetic transition.[1] The shifting of $T_{N1}$ and $T_{N2}$ may be induced by the excess trivalent $Fe^{3+}$ in the system, as Fe doping in a $Fe_{1+x}V_{2-x}O_4$ will push $T_{N1}$ towards the high temperature side and $T_{N2}$ towards the low temperature side.[11] The trend of magnetization is in good agreement with our findings from the XMCD measurements.

In summary, the magnetic moments of Fe and V ions are antiparallel to each other, implying that the synthesized FVO thin film has the same magnetic ordering as the bulk spinel do.

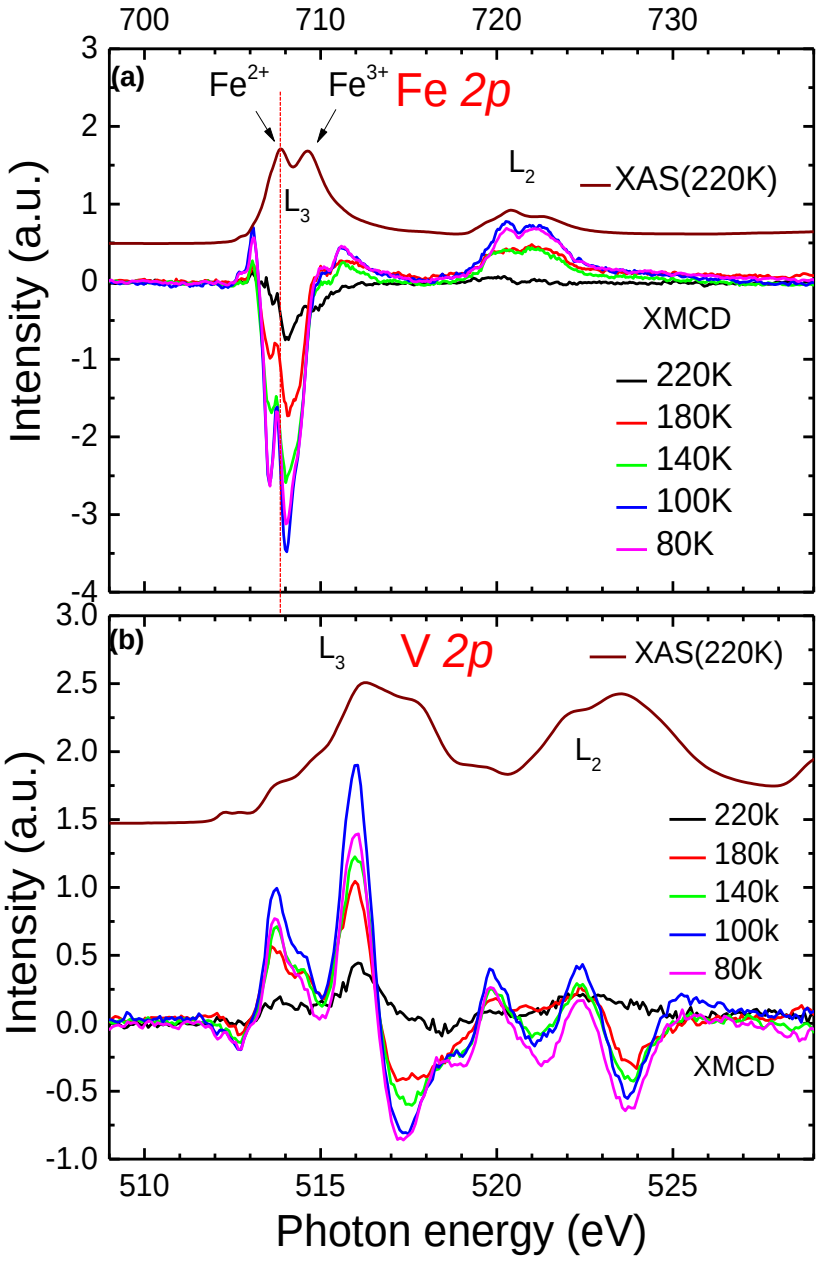


**Figure 4.7** XAS and XMCD spectra of Fe (a) and V (b) $L_{3,2}$ edge taken at 80 K, 100 K, 140 K, 180 K and 220 K.

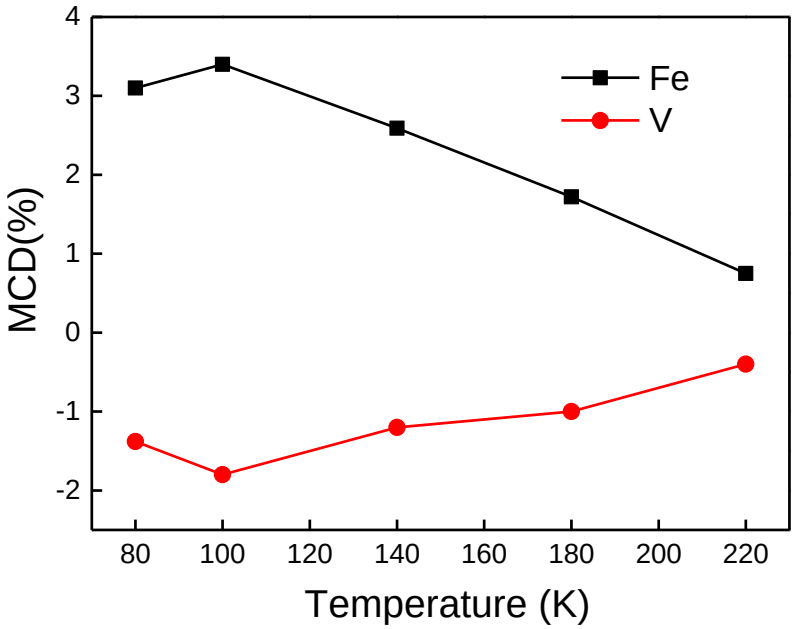


**Figure 4.8** The $L_3$ edge peak intensity of Fe (in black) and V (in red) as a function of temperature.

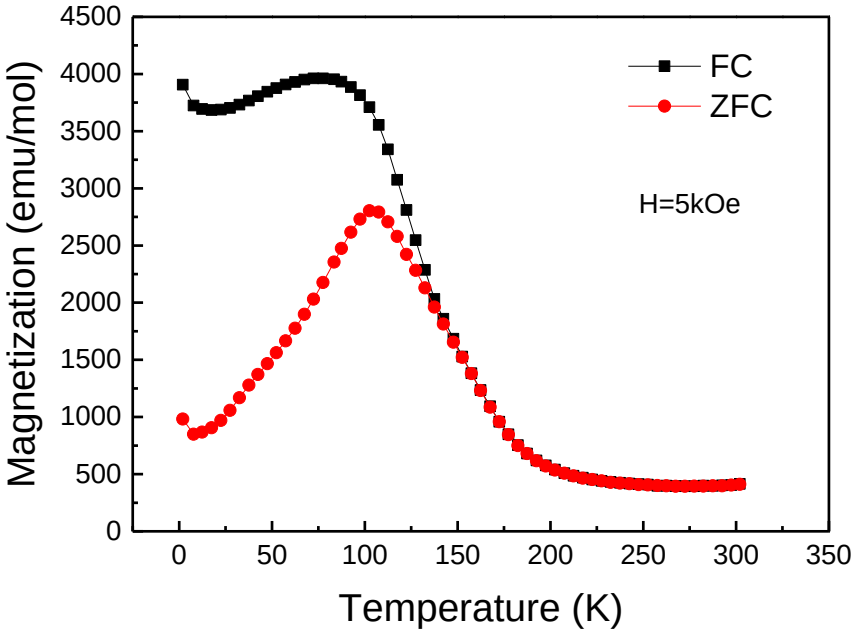


**Figure 4.9** The temperature dependence, field cooled (in black) and zero field cool (ZFC), of the magnetization of the FVO thin film.

### 4.3.3 Magnetic Hysteresis Loop

To further investigate the magnetic properties of the FVO thin film, M-H curves of a 100-nm-thick FVO/STO film were taken at various temperatures (10 K, 60 K and 100 K). Both in-plane and out-of-plane magnetizations were measured.

As shown in **Figure 4.10**(a), the intensities of the out-of-plane magnetization taken at different temperatures are similar, about 4300 emu/mol, which is consistent with that of the **M-T** curves discussed earlier. The coercive field $\mathbf{B}_c$ gets stronger as the temperature decreases. It changes from ~2 T at 100 K to ~4 T at 10 K which is much larger than those of polycrystalline[12] and single crystal samples[13]. This can be attributed to the size effect, as it is a well-known behaviour that $\mathbf{B}_c$ increases with decreasing sample size in conventional ferromagnets. In particular, small step-like jumps can be observed at $\mathbf{H}$ = 0 T in OOP curves. In general, this behaviour indicates that the magnetic coupling between two phases, one has a large $\mathbf{B}_c$ (phase A) and the other a small $\mathbf{B}_c$ (phase B), present in the system is decoupled. The volume of phase B is very small, since the change of $\mathbf{M}$ at 0 T is much smaller than that at the higher $\mathbf{H}$ (~2-4 T).

A large anisotropy of the **M-H** curve is observed: the in-plane magnetization, shown in **Figure 4.10**(b), is much smaller than those of out-of-plane magnetizations, indicating that the *c* axis is the easy axis of magnetization at low temperatures. It also shows a different trend for the magnetization as temperature drops: it decreases first (from 100 K to 60 K) and then increases (from 60 K to 10 K). This could correspond to the phase transition from the orthorhombic phase to the low temperature tetrahedral phase, which occurs at 40 K, accompanied by the tilting of V magnetic moments. On the other hand, the coercive field of the IP curves increases as the temperature decreases, following the same trend as in OOP curves. However, the values of the IP $\mathbf{B}_c$ are much smaller than those of the OOP curves, which can also be attributed to the size effect, as the scale of the film sample along the *a* and *b* axes is much larger than that of the *c* axis.

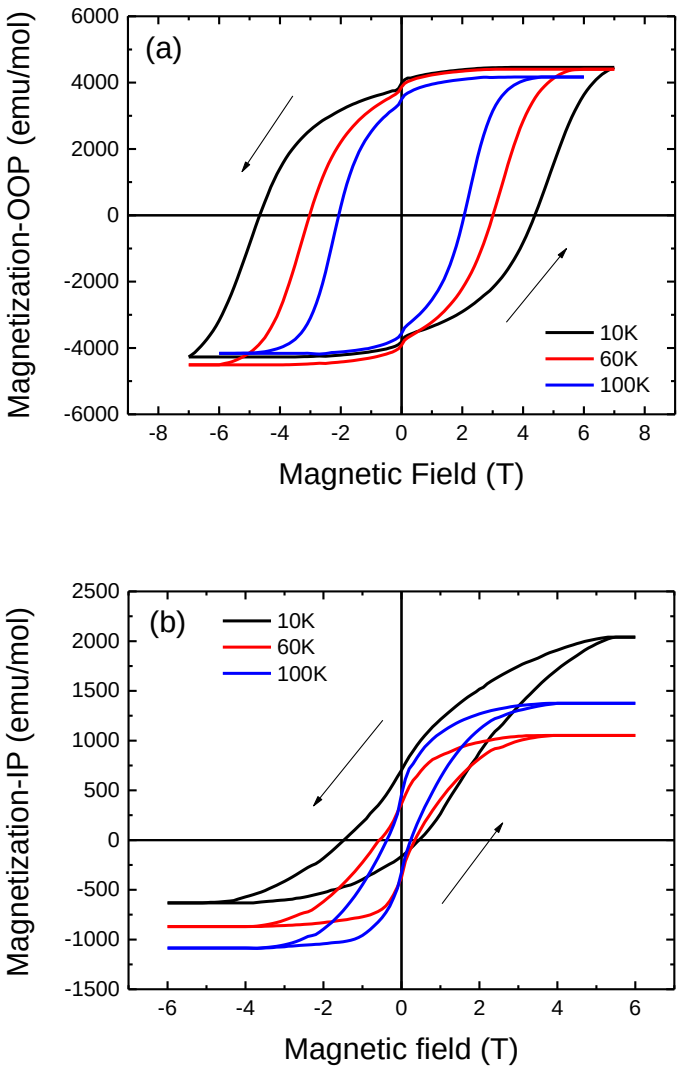


**Figure 4.10** Out-of-plane (a) and in-plane (b) magnetic hysteresis loop of a 100-nm-thick FVO/STO sample taken at various temperatures (10 K, 60 K and 100 K).

Interestingly, a vertical shift towards the positive side was presented in the IP **M-H** curves, especially at 10 K. Since we heated the sample up to 200 K after each measurement and cooled it down again for the next measurement, the vertical shift should not be attributed to the field being cooled or the remnant effect. We presume that the characteristically strong magnetocrystalline anisotropy arises because of the large spin-orbit coupling of V, leading to the vertical shift in the IP **M-H** loops. Moreover, unlike the OOP curves, we did not find magnetic jumps at the point that **H** = 0 T, indicating that 'the phase B' does not contribute to the IP magnetization.

### 4.3.4 Magnetic Force Microscopy

The MFM images of FVO thin films as a function of applied magnetic fields (out-of-plane) are shown in **Figure 4.11**. The dark and light areas represent the magnetic domains of the FVO thin film with different magnetization directions (pointing out/in). As can be seen, starting from 0 T, the contrast of the image increases as the magnetic field increases, indicating the enhanced probe-sample magnetic interaction due to the magnetisation of the sample. At 3 T, the highest contrast was achieved. As the magnetic field increased, we started losing the contrast, and at 9 T, the image became almost "flat". This is caused by the magnetic domain switching. As the magnetization directions of domains are all aligned to the applied magnetic field, this forms a uniformed probe-sample magnetic interaction across the sample surface. The pattern of the magnetic domains stayed the same while the magnetic field was lower than 3 T, however, the pattern changed and flipped at 3 T, as shown in the red and blue boxes in **Figure 4.11**.

The magnetic field was then reduced to zero and a magnetic field with the opposite direction was applied and gradually increased. The MFM images are shown in **Figure 4.12**. A similar trend in the contrast was observed: increasing with the magnetic field increasing, and then decreasing when the magnetic field was higher than 3 T. Interestingly, after carefully examining the images (9 T, 0 T, -0.2 T and 3 T), as shown in **Figure 4.13**, we found that the domains remained basically unchanged when the applied field was taken away. However, when a -0.2 T magnetic field was applied, the contrast of the image flipped, dark turned into bright and bright turned into dark. This may have been caused by the re-orientation of the magnetic domains of the 'phase B', as mentioned earlier in this chapter. In other words: the domains of 'phase B' were switched by applying a relatively low magnetic field, which is in good agreement with the weak coercive field $\mathbf{H}_c$ observed in the out-of-plane **M-H** loops. Another possibility is that the magnetic state of the tip changed, leading to an opposite signal output. Further experiments need to be undertaken to clarify the cause of this.

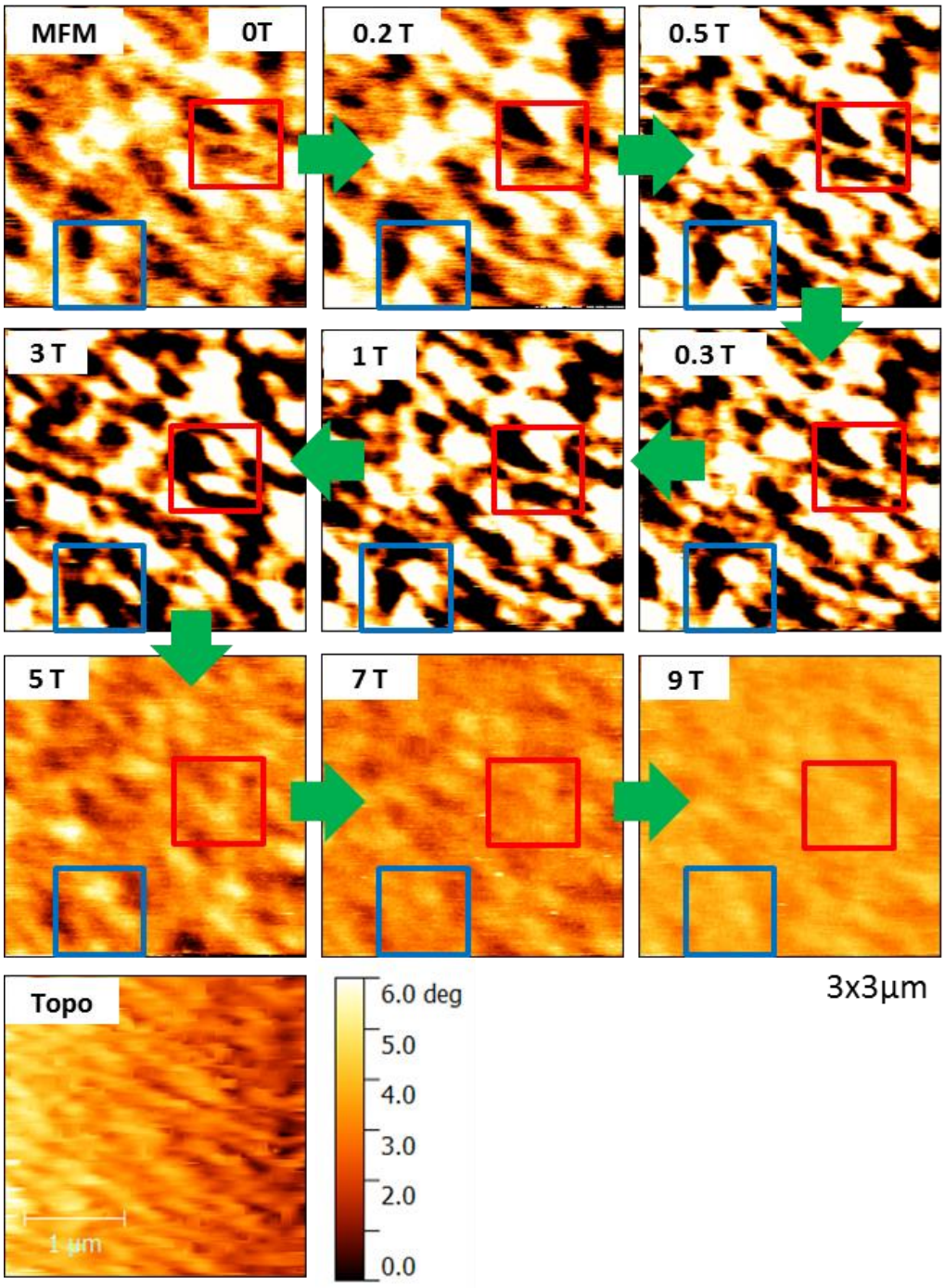


**Figure 4.11** Magnetic force microscopy images of the FVO film as a function of applied magnetic field (0 T~9 T).

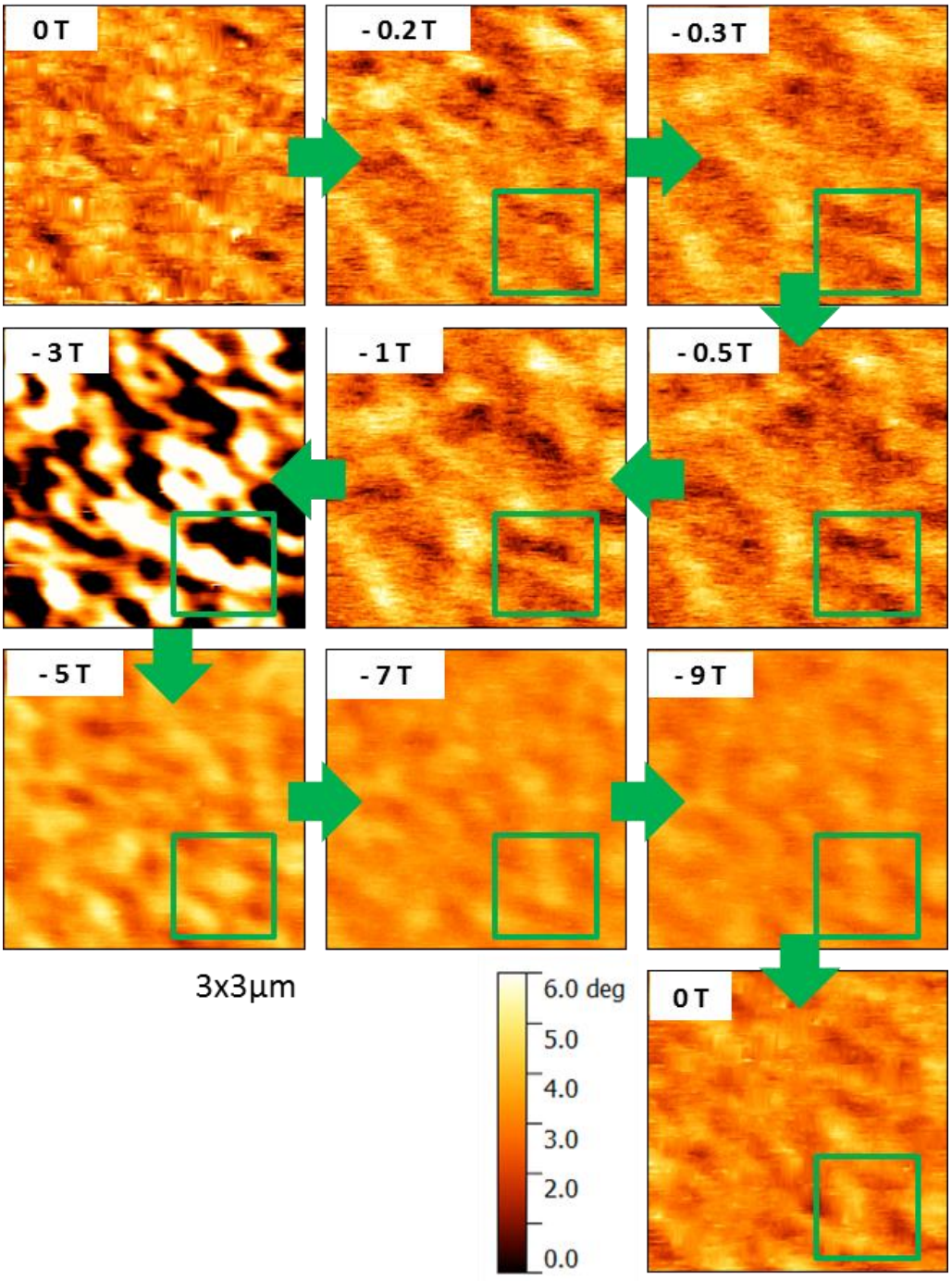


**Figure 4.12** Magnetic force microscopy images of the FVO film as a function of applied magnetic field (0 T~-9 T).

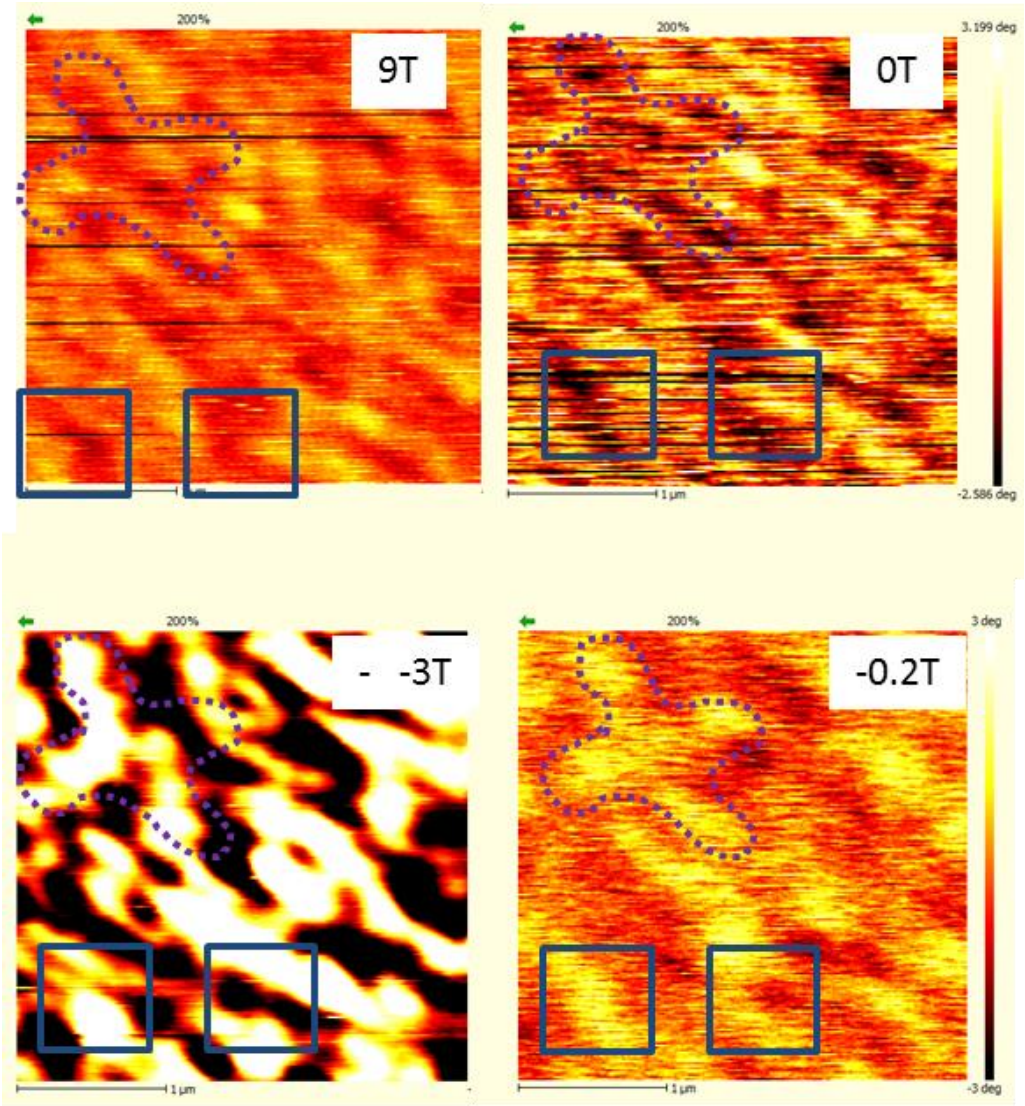


**Figure 4.13** Magnetic force microscopy images of the FVO film as a function of applied magnetic field (9 T, 0 T,-0.2 T and -3 T). The sign of the signal reversed from 0 T to -0.2 T.

## 4.4 Summary

This chapter presented the characterization of the magnetic properties of FVO thin film. The electric and spin states of the Fe and V ions were investigated by XAS and XMCD, respectively. The results show that the Fe ions in our FVO thin film are mainly divalent, whereas the V ions are trivalent, indicating that the synthesized FVO thin film is chemically analogous to the bulk spinel. However, a trace of trivalent $Fe^{3+}$ was found in the XAS and XMCD spectra, indicating that there might be excess $Fe^{3+}$ in the system sitting in the tetragonal site and forming $Fe^{2+}(Fe^{3+}_{x}V^{3+}_{(2-x)})O_4$. The magnetic moments of the film originate because the divalent Fe and trivalent V ions present an antiparallel arrangement. The temperature dependence of the XMCD signal of Fe and V show a strong coupling between the two ions, and the trend is consistent with the **M-T** measurement with a Nèel temperature of ~120 K. A shifting of $T_{N1}$ and $T_{N2}$ also suggests that there are excess $Fe^{3+}$ ions in the system. The M-H loops reveal the magnetic anisotropy of the FVO film, with larger magnetization and stronger coercive field along the *c*-axis. A small magnetic jump at $\mathbf{H}$ = 0 T gives a hint of the presence of a 'phase B' in the system, which is possibly related to the $Fe^{3+}$ excess phase. The MFM measurements thus give a direct visual impression of the magnetic nature of the FVO films at low temperature. Furthermore, the magnetic moments can be reorientated by applying an external magnetic field higher than 3 T, while a switching at a lower field was also observed.

References

[1] G. J. MacDougall, V. O. Garlea, A. A. Aczel, H. D. Zhou, S. E. Nagler,Magnetic order and ice rules in the multiferroic spinel FeV2O4, Phys. Rev. B 2012, 86, 060414.
[2] J. S. Kang, J. Hwang, D. H. Kim, E. Lee, W. C. Kim, C. S. Kim, H. K. Lee, J. Y. Kim, S. W. Han, S. C. Hong, B. Kim, B. I. Min,Soft x-ray magnetic circular dichroism study of valence and spin states in FeT2O4 (T = V, Cr) spinel oxides, J. Appl. Phys. 2013, 113.
[3] R. Takahashi, H. Misumi, M. Lippmaa,Growth temperature effect on the structural and magnetic properties of Fe3O4 films grown by the self-template method, J. Appl. Phys. 2014, 116, 033918.
[4] M. Abbate, H. Pen, M. T. Czyzyk, F. M. F. Degroot, J. C. Fuggle, Y. J. Ma, C. T. Chen, F. Sette, A. Fujimori, Y. Ueda, K. Kosuge,Soft-X-Ray Absorption-Spectroscopy of Vanadium-Oxides, J. Electron Spectrosc. 1993, 62, 185.
[5] M. Abbate, F. M. F. Degroot, J. C. Fuggle, Y. J. Ma, C. T. Chen, F. Sette, A. Fujimori, Y. Ueda, K. Kosuge,Soft-X-Ray-Absorption Studies of the Electronic-Structure Changes through the VO2 Phase-Transition, Phys. Rev. B 1991, 43, 7263.
[6] T. Katsufuji, T. Suzuki, H. Takei, M. Shingu, K. Kato, K. Osaka, M. Takata, H. Sagayama, T. H. Arima,Structural and magnetic properties of spinel FeV2O4 with two ions having orbital degrees of freedom, J. Phys. Soc. Jpn. 2008, 77.
[7] Q. Zhang, K. Singh, F. Guillou, C. Simon, Y. Breard, V. Caignaert, V. Hardy,Ordering process and ferroelectricity in a spinel derived from FeV2O4, Phys. Rev. B 2012, 85, 054405.
[8] J. S. Kang, J. Hwang, D. H. Kim, E. Lee, W. C. Kim, C. S. Kim, S. Kwon, S. Lee, J. Y. Kim, T. Ueno, M. Sawada, B. Kim, B. H. Kim, B. I. Min,Valence states and spin structure of spinel FeV2O4 with different orbital degrees of freedom, Phys. Rev. B 2012, 85, 165136.
[9] T. J. Regan, H. Ohldag, C. Stamm, F. Nolting, J. Luning, J. Stohr, R. L. White,Chemical effects at metal/oxide interfaces studied by x-ray-absorption spectroscopy, Phys. Rev. B 2001, 64, 214422.
[10] C. I. Pearce, C. M. B. Henderson, R. A. D. Pattrick, G. Van der Laan, D. J. Vaughan,Direct determination of cation site occupancies in natural ferrite spinels by L-2,L-3 X-ray absorption spectroscopy and X-ray magnetic circular dichroism, Am. Mineral 2006, 91, 880.
[11] N. Liu, K. H. Zhao, X. L. Shi, L. W. Zhang,Fe3+ doping effects on the structure and multiferroicity of Fe1+xV2-xO4 (0 <= x <= 0.4) spinels, J. Appl. Phys. 2012, 111, 124112.
[12] S. Nishihara, W. Doi, H. Ishibashi, Y. Hosokoshi, X. M. Ren, S. Mori,Appearance of magnetization jumps in magnetic hysteresis curves in spinel oxide FeV2O4, J. Appl. Phys. 2010, 107, 09A504.
[13] H. Takei, T. Suzuki, T. Katsufuji,Nonvolatile memory effect of capacitance in polycrystalline spinel vanadate, Appl. Phys. Lett. 2007, 91, 072506.

# CHAPTER FIVE

# 5 ELECTRIC PROPERTIES OF IRON VANADATE FILMS

## 5.1 Synopsis

In chapter 4, the magnetic properties of the FVO films were investigated using XAS, XMCD and MFM, and the results were consistent with those of the bulk material. In this chapter, the electric properties are explored, including resistivity, pyroelectricity and dielectricity, of the FVO films. The magneto-electric coupling effect of the FVO films is also investigated by the magnetocapacitance measurements. (The measurements in this chapter were carried out by Dr. Ryota Takahashi).

Firstly, the 4-point resistance measurement method was employed to measure the resistivity of the FVO films and the measured data were fitted with different models, including Arrhenius' Law,[1] the polaron model[2] and the variable-range hopping model.[3] Then, the pyroelectric effect was investigated by using a dynamic pyroelectric effect measuring method.[4] The polarization of the FVO films was estimated by the integration of the pyroelectric current. Furthermore, the capacitance of a Pd/FVO/Nb:STO device was measured as a function of temperature and frequency. A step-like curve shape was observed indicating two dielectric relaxation types: intrinsic and extrinsic Maxwell-Wagner relaxation. We simulated the data with a 2 RC equivalent circuit model, and it showed that at the temperature regime higher than ~40 K the capacitance of the device is dominated by the extrinsic interfacial Maxwell-Wagner relaxation. Finally, the magnetocapacitance of the device was investigated at 10 K, and the observed hysteresis loop indicated thee magneto-electric coupling of the FVO films.

## 5.2 Experimental Details

To measure the temperature dependence of the FVO thin film resistivity, a 100-nm-thick FVO/STO film with Ag electrodes and the 4-point probe method were used. The schematic diagrams of the sample and measurement setups are shown in **Figure 5.1**.

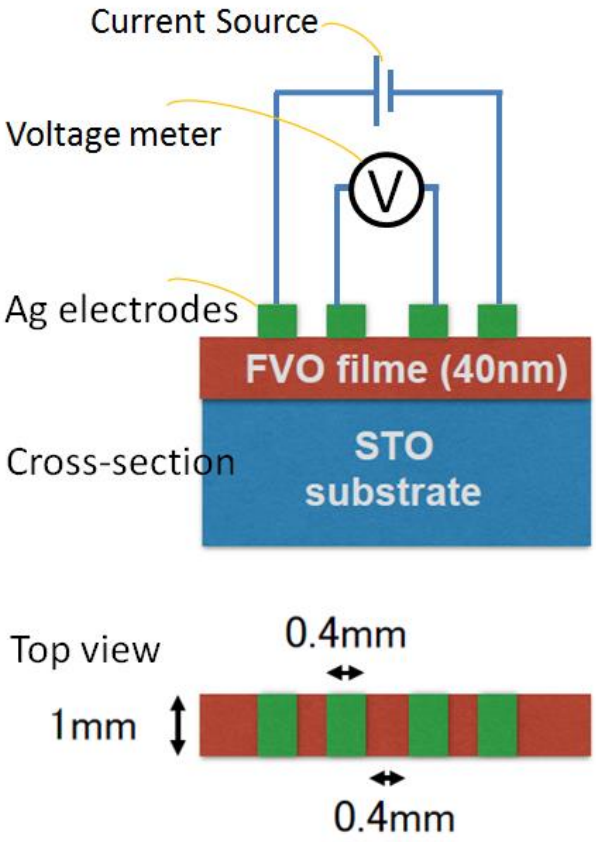


**Figure 5.1** Schematic diagrams of the sample and 4-point probe measurement setups.

For the measurements of pyroelectric effect of FVO thin films, 100-nm-thick FVO films were deposited on semiconducting Nb (0.05%wt) doped STO(001) substrates. 100-nm-thick Pd top electrodes with 1 mm diameter were deposited on the FVO/Nb:STO film surface by electron beam evaporation through a stencil mask. Aluminium wires were attached to the electrode pads by silver paste. The sample was cooled in a vacuum chamber using a two-stage cryo-cooler and was cooled from 300 K to 8 K. A diode laser with a wavelength of 1.31 μm and power of 130 mW was used to modulate the device temperature inducing a pyroelectric current. The diode laser was chopped by modulating the current with an optical

power rise time of 3 µs and was focused on the Pd electrode pad. The current signal was converted to a voltage signal with a current-voltage converter at a transconductance of $10^8$ V/A and measured with a lock-in amplifier.

The dielectric properties of the FVO films were investigated by measuring the capacitance of a Pd/FVO/Nb:STO device. The structure of the device is shown in **Figure 5.2**. A 100-nm-thick FVO film was deposited on an Nb doped (0.05%wt) $SrTiO_3$ substrate. 100-nm-thick Pd top electrodes with 1 mm diameter were deposited on the FVO/Nb:STO film, and then the sample was bounded to a Be-Cu plate with Ti/Au/Ag paste as the bottom electrode. Aluminium wires were bounded to the top and bottom electrodes with silver paste. The dielectric measurements were carried out with an impedance bridge (Agilent 4284) at an excitation voltage of 100 mV.

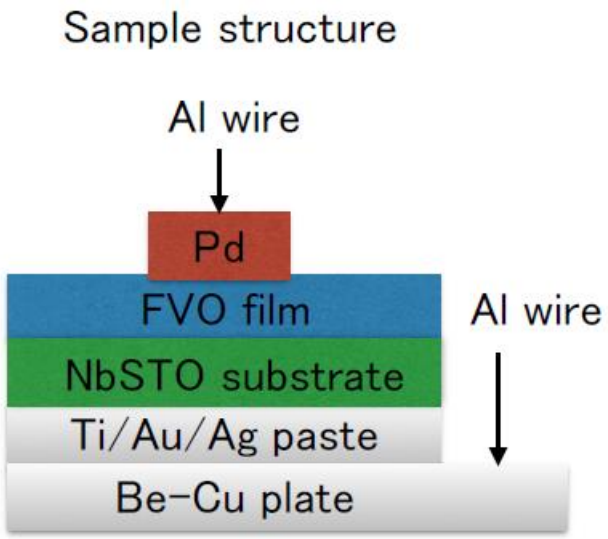


**Figure 5.2** Schematic diagram of the Pd/FVO/Nb:STO device used for the dielectric proper measurements.

## 5.3 Results and Discussion

### 5.3.1 Resistivity

The measured resistivity of a 100-nm-thick FVO/STO sample is shown in **Figure 5.3**. As we can see, the resistivity increases exponentially as temperature decreases. It is about 3 Ω·cm at room temperature and rises higher than 2000 Ω·cm at ~120 K.

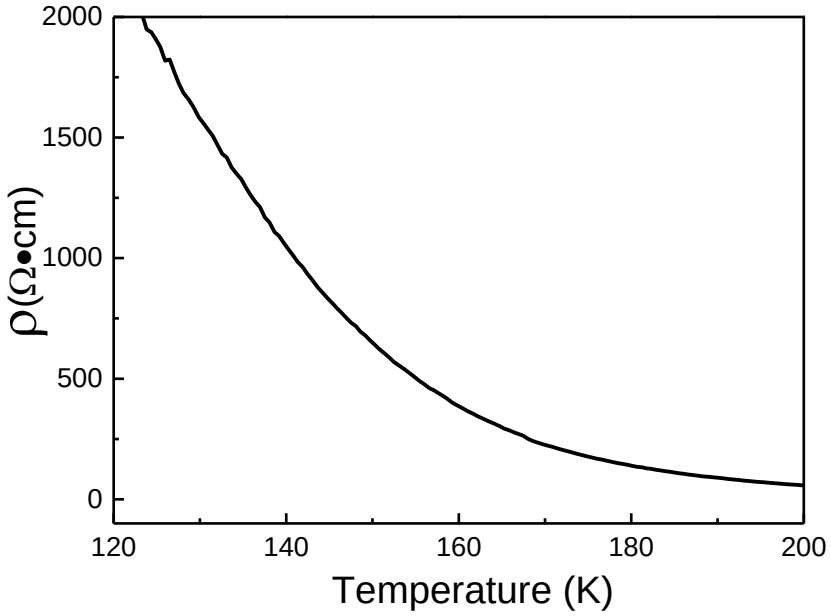


**Figure 5.3** Temperature dependence of the resistivity of a 100-nn-thick FVO/STO film.

To understand the mechanism of the temperature dependence of the resistivity of FVO films, Arrhenius law (Eq.5.4), the polaron model (Eq.5.5) and the Variable-range-hopping model (Eq.5.14) were used to fit the measured data. The fitting curves are shown in **Figure 5.4**. All three models show good fittings, and among them, the VRH model has the best fit, indicating that FVO have localized carriers in the measured temperature range. The activation energy calculated from Arrhenius law is 0.29 eV and the characteristic barrier energy parameter $T_0$ obtained from the VRH model is $2.448 \times 10^8$ K.

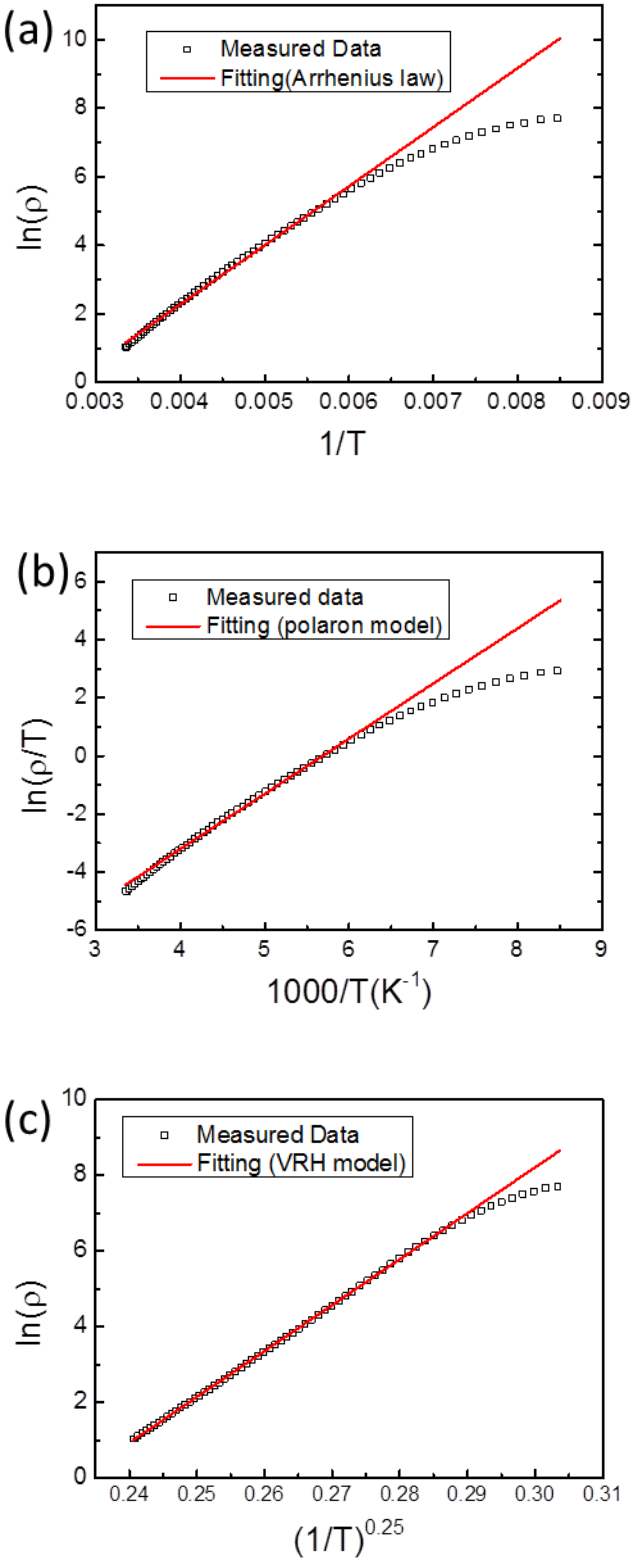


**Figure 5.4** Fitting of the resistivity of the FVO/STO film with (a) Arrhenius law, (b) Polaron Model and (c) Variable-range-hopping model.

### 5.3.2 Pyroelectric Current

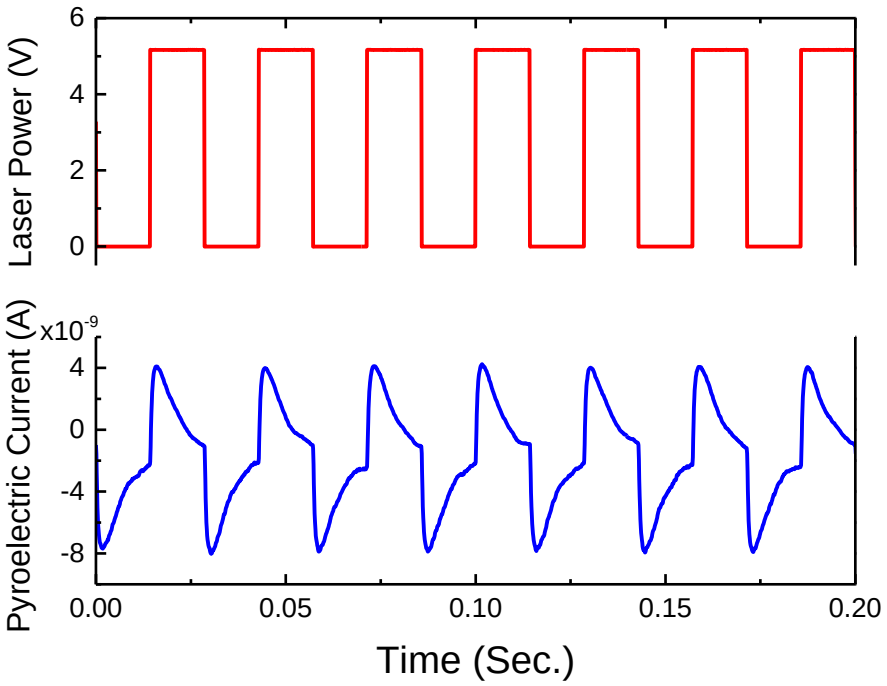


**Figure 5.5** Laser power (top) and current (Bottom) as a function of time at 100 K.

**Figure 5.5** shows the Laser power and pyroelectric current as a function of time taken at the temperature of 100 K. Spikes in the curve appear at the point when the illumination is turned on and off, with opposite directions, and is caused by the temperature dependence of the spontaneous polarization in polar materials. This indicates that, at 100 K, the FVO film possesses spontaneous polarization.

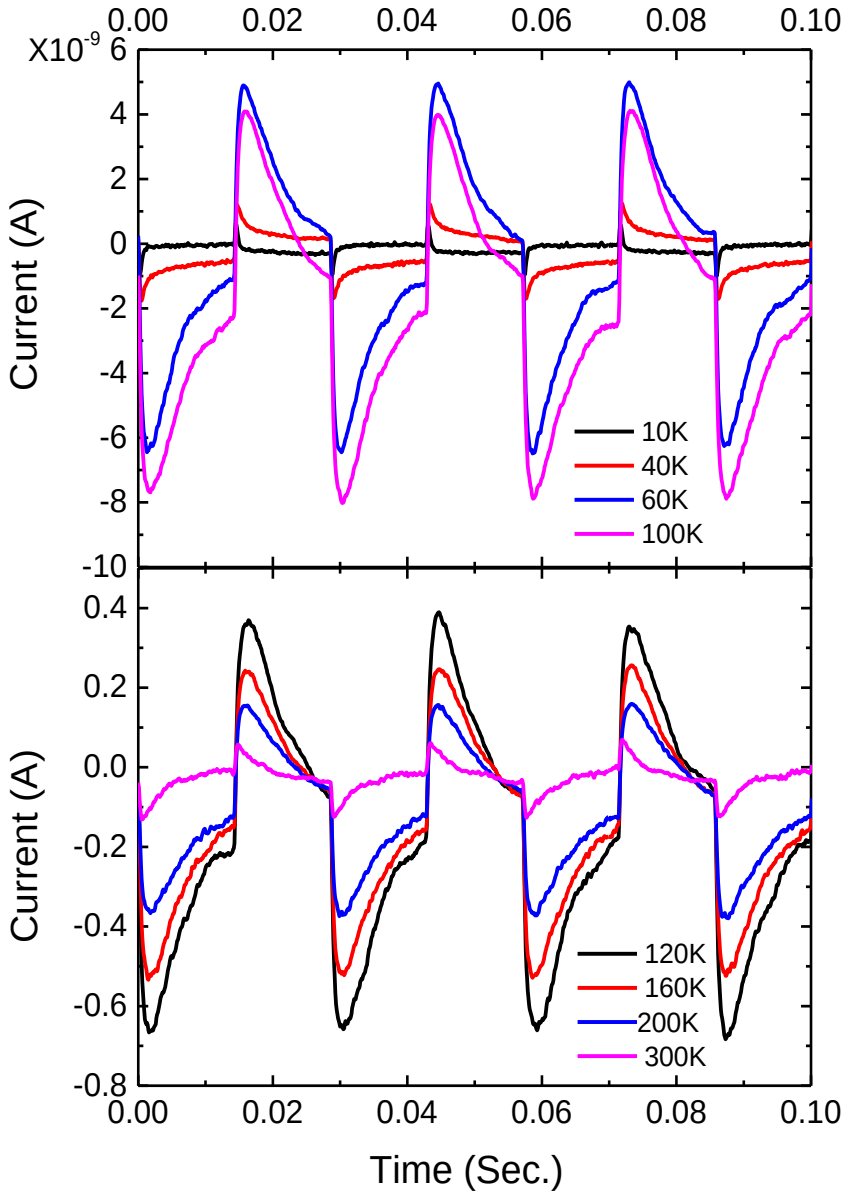


**Figure 5.6** Pyroelectric current measured at different temperatures.

The pyroelectric current was then measured at different temperature points, shown in **Figure 5.6**. All curves show the spikes and the intensity varies as the temperature changes. To further study the trend of the pyroelectric current, a continuous pyroelectric response amplitude, as well as the phase vs. temperature were measured, and shown in **Figure 5.7**(a). The current increases as the temperature decreases from 300 K, and the maximum signal is observed at 100 K. As the temperature further decreases, the signal decreases rapidly and then stabilises at below 40 K, accompanied by a sharp change in the phase curve.

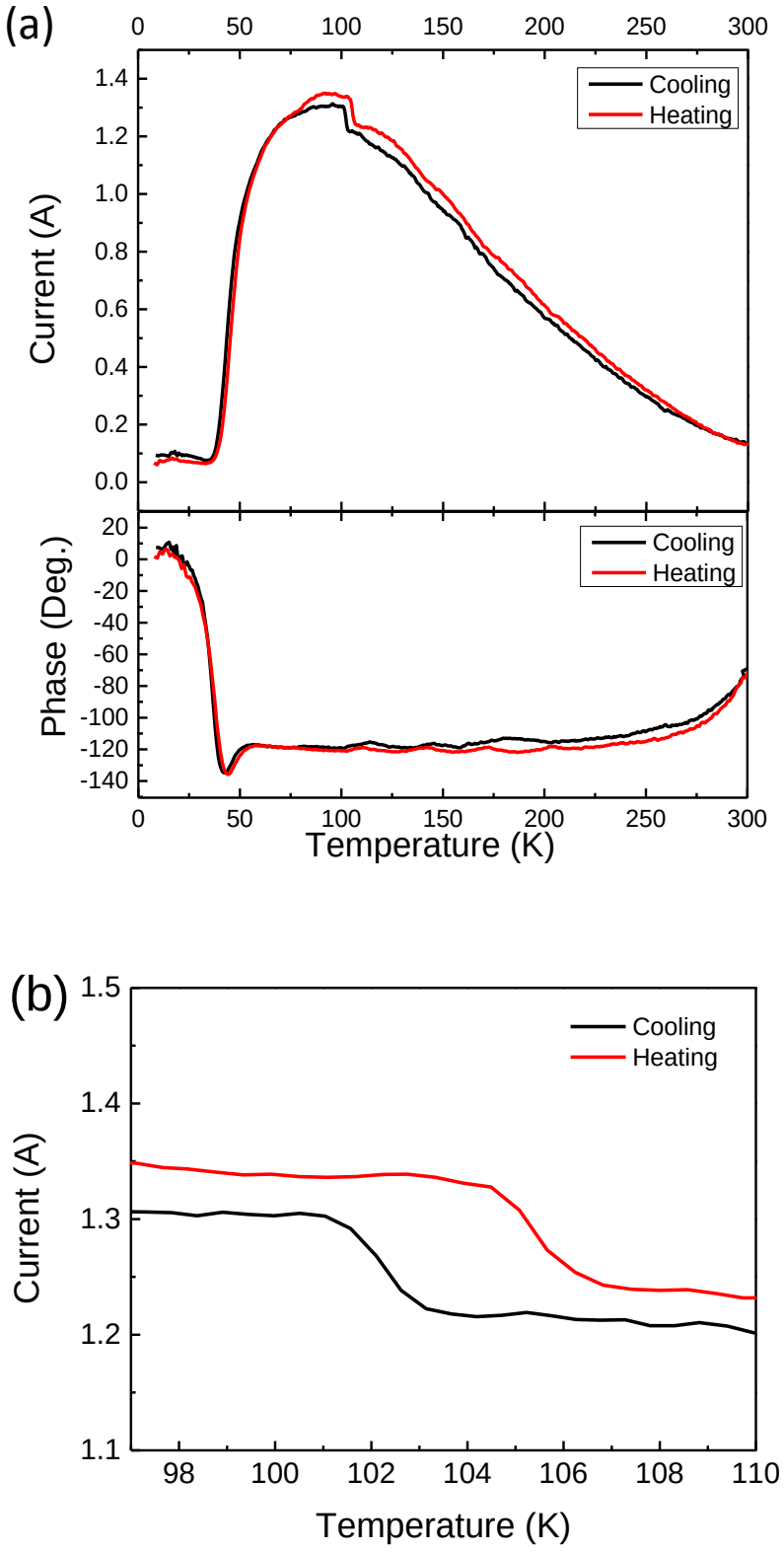


**Figure 5.7** (a) Pyroelectric response amplitude and phase as a function of temperature. (b) A sharp change of the amplitude at 105 K induced by the phase transition of STO substrate.

This change corresponds to the phase transition of the FVO crystal, from an orthorhombic phase to a low temperature tetragonal phase. A sharp change of the amplitude is observed at 105 K, **Figure 5.7**(b). This is caused by the structural transition in the STO crystals (the substrate) at 105 K, and the strain state of the FVO film is changed at this temperature. Similar behaviour in pyroelectric response was found in other ferroelectric films on STO substrates.[5] Generally, the pyroelectric current is proportional to the differential of the polarization, and the polarization as a function of temperature can be estimated by the integration of the pyroelectric current [4]. **Figure 5.8** shows the temperature dependence of the polarization of the FVO/Nb:STO sample. Obviously, the sample shows spontaneous polarization at low temperatures. The polarization increases as the temperature drops and saturates at 40 K.

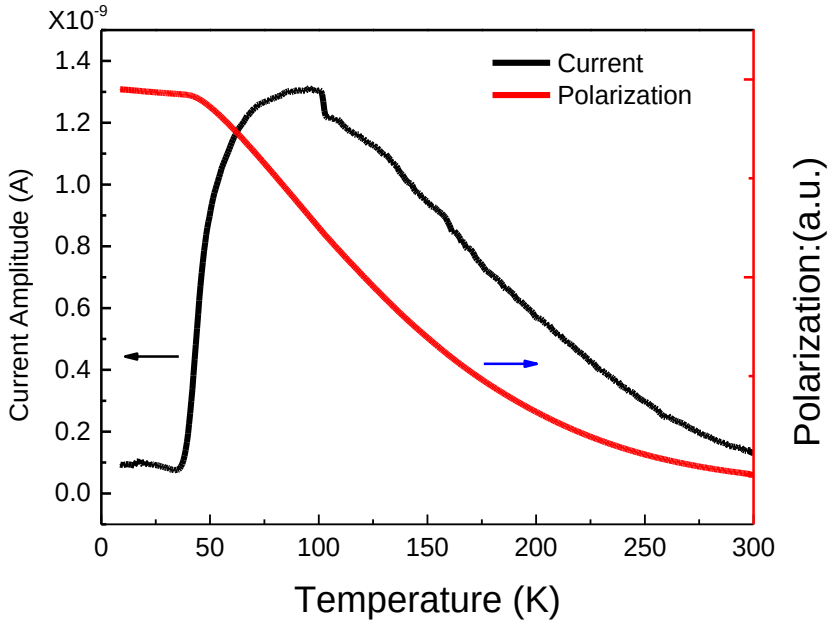


**Figure 5.8** Pyroelectric response (in black) amplitude and polarization (in red) of the FVO/STO sample.

The pyroelectric current we observed in the Pd/FVO/Nb:STO device indicates a spontaneous polarization, however the origin of the polarization is still unknown, since the measurement is not reliable as we cannot repeat the result. Moreover, the pyroelectric current is detected at high temperatures up to 300 K, in the cubic paramagnetic phase of FVO. The pyroelectric current is more likely to

have been induced from the interface effect rather than the FVO thin film. Further experiments need to be done in order to identify the origin of pyroelectric effect in the sample.

### 5.3.3 Dielectric Properties

#### 5.3.3.1 Interfacial Resistance

As the interfacial resistance will greatly affect the measured capacitance of the device[6], we first measured the temperature dependent *I-V* characterization of the device to identify the Schottoky barrier height of the FVO/Nb:STO interface. The $I$-$V$ curves acquired at different temperatures are shown in **Figure 5.9**. The currents increase as the temperature increases. Within thermionic emission theory, the current density J can be expressed as:

$$J = A^{*}T^{2}\exp\left(-\frac{q\Phi_B}{kT}\right)\exp\left(\frac{qU_F}{nkT}\right)\left[1-exp\left(-\frac{qU_F}{kT}\right)\right] \tag{5.49}$$

$$I \approx SA^{*}T^{2}exp\left[-\frac{q}{kT}\left(\Phi_B-\frac{U_F}{n}\right)\right] \tag{5.50}$$

$$E_a = \Phi_B - \frac{U_F}{n} \tag{5.51}$$

where $S$ is the surface area of the electrode, $A$* is the effective Richardson constant, $T$ is absolute temperature, $q$ is the elementary charge, $k$ is the Boltzmann constant, $\Phi_B$ is the effective Schottky barrier height, and $U_F$ is the forward bias voltage. From Eq.5.18, we plotted $ln(I/T^2)$ as a function of $q/kT$, and it gave a linear dependence, as shown in **Figure 5.10**(a), where the absolute value of the slope equals to the activation energy, $E_a$. From Eq.5.3, the Schottky barrier height, $\Phi_B$, and ideality factor, $n$, can be extracted from the intercept and slope of the $E_a$ vs $U_F$ plot, respectively. **Figure 5.10**(b) shows the linear fit of $E_a$ vs $U_F$ plot, and the estimated value of $\Phi_B$ and $n$ are 0.207 eV and 3.45, respectively. Our experimental value of the barrier height between Pd and Nb:STO is much lower than the expected value which is 1.1 V. The reduction of the Schottky barrier height has been found in other junctions such as metal/Pb(ZrTi)$O_3$/$SrRuO_3$.[7] Such reduction of barrier height at the interface can be attributed to the potential shift caused by the internal field in the polar film. In the thermionic model, with an

ideality factor larger than 2, 3.45 in our case, the contact is non-ideal Schottky contact. Besides the thermionic current, there are other components that contribute to the total current. This indicates that our Pd/FVO/Nb:STO junction is a metal-insulator-semiconductor device other than a pure metal-semiconductor Schottky junction, and the conductivity of the spinel film is much higher than that of the FVO/Nb:STO Schottky junction.

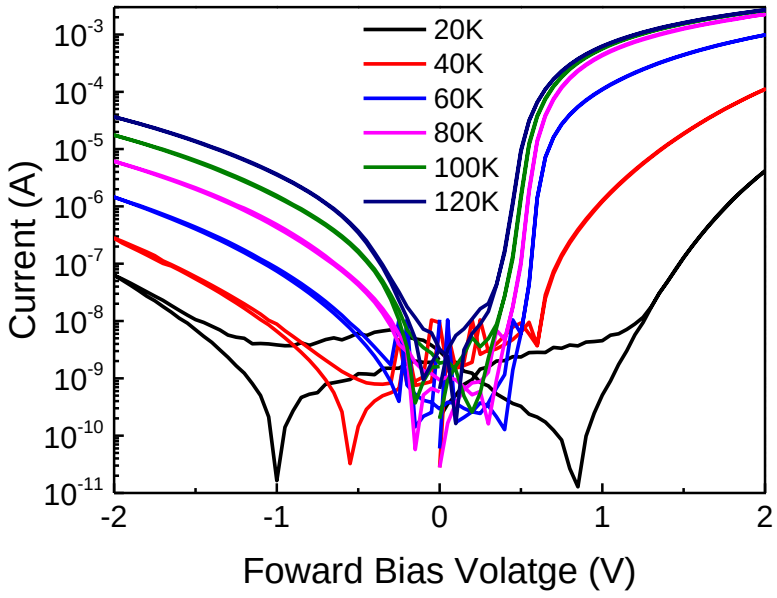


**Figure 5.9** *I-V* curves of the Pd/FVO/Nb:STO junction taken at various temperatures.

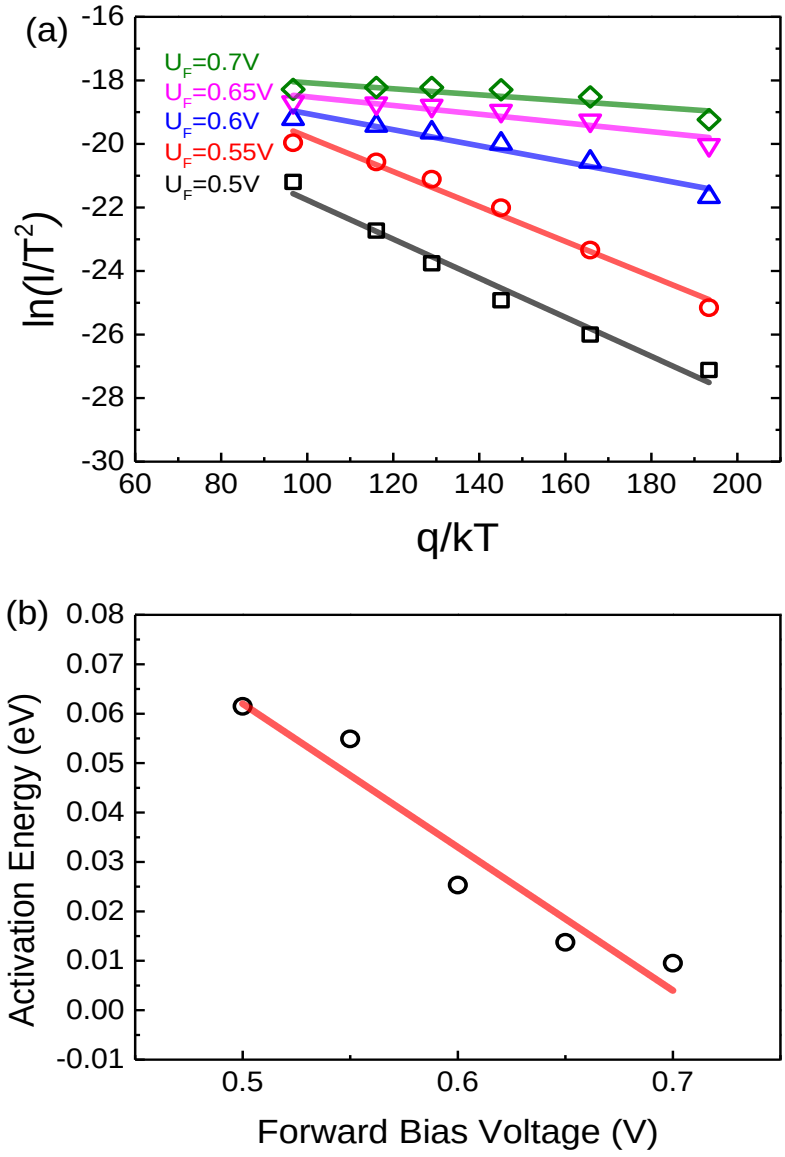


**Figure 5.10** (a) A Richardson plot of $ln(I/T^2)$ vs $q/kT$ at different forward bias voltage (from 0.5 V to 7 V). (b) Activation Energy, $E_a$, vs Forward Bias Voltage, $U_F$.

### 5.3.3.2 Temperature Dependence of Capacitance

The temperature dependence of the capacitance and $tan\delta$ of the Pd/FVO/Nb:STO sample were measured at various frequencies, as shown in **Figure 5.11**(a,b) (open symbols). Similar to earlier reports on $CaCu_3Ti_4O_{12}$, $BiMnO_3$ and $Fe_3O_4$[8-10], the capacitance exhibits a steplike increase from a low-temperature plateau to a high-temperature plateau. The two plateaus typically represent 2 relaxations; one is the intrinsic film, and the other is the extrinsic Maxwell-Wagner-type dielectric relaxation which is caused by the formation of an interface Schottky-type barrier. We modelled the two element device with a series circuit of two ideal resistor-capacitor (RC) elements. The equivalent circuit was shown in **Figure 5.11**(c), where $R_1C_1$ and $R_2C_2$ represent the intrinsic film contribution and the extrinsic Maxwell-Wagner-type relaxation respectively.

The film resistance, $R_1$, can be estimated from the 4 point resistivity measurement of the FVO/STO film, as discussed earlier in this chapter. It follows the Variable-range-hopping model, and can be expressed as Eq.5.14. The calculated $\rho_0$ and $T_0$ are 6.549x10$^{-13}$ Ω·cm and 2.448x10$^8$ K, respectively. The interfacial resistance, $R_2$, was then estimated from the Eq.5.1 as

$$R_2 = \frac{V}{I} = lT^{-2}exp\left(\frac{m}{T}\right) \tag{5.52}$$

where $V$ is the bias voltage. The coefficients $l$ and $m$ were estimated to be 6.147x10$^8$ and 402, respectively. **Figure 5.12** shows the temperature dependence of the $R_1$ and $R_2$ used in the calculation of the total capacitance of the equivalent circuit.

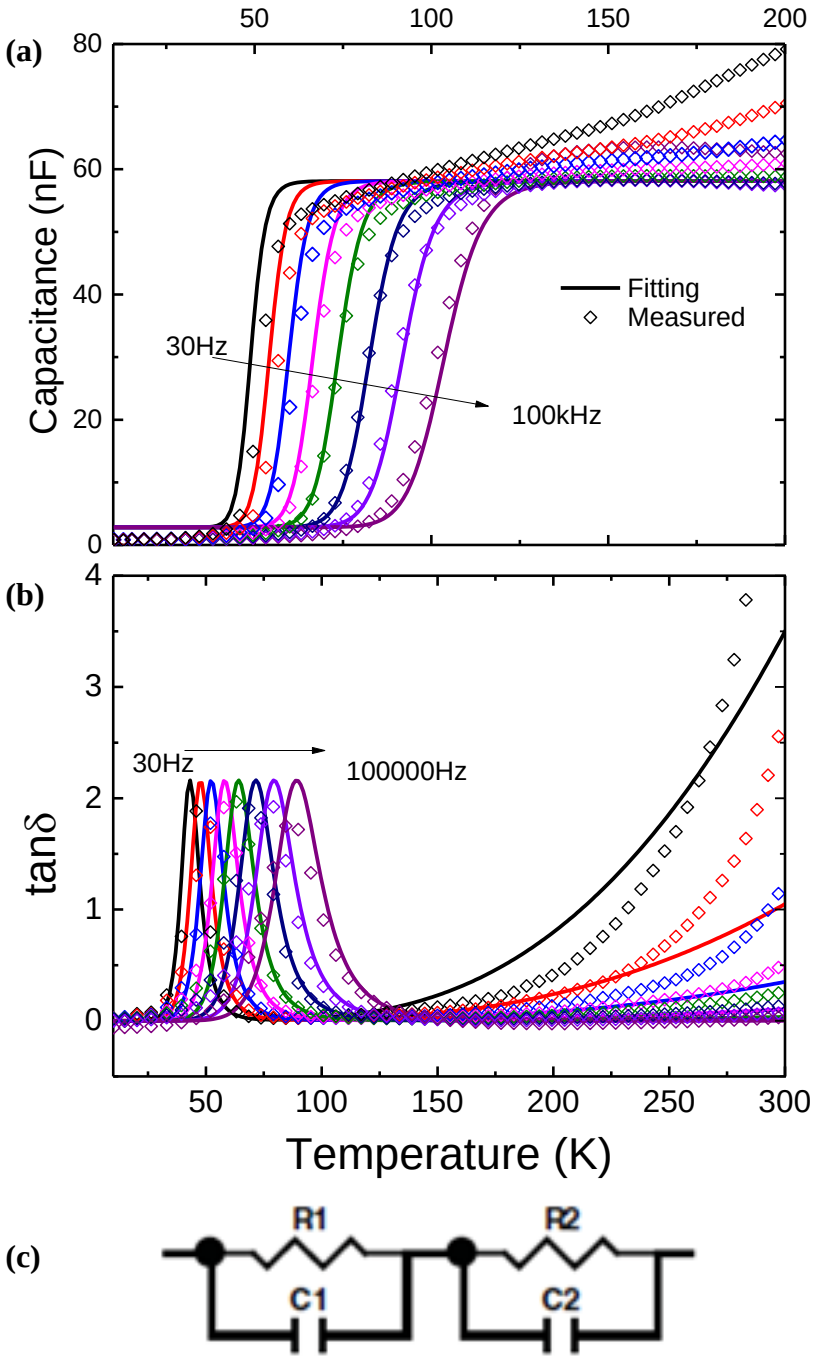


**Figure 5.11** (a,b) The temperature dependence of the capacitance and $tan\delta$ of the Pd/FVO/Nb:STO junction of various measuring frequencies (measured data in open symbols and calculated data in solid lines). (c) The two RC elements equivalent circuit.

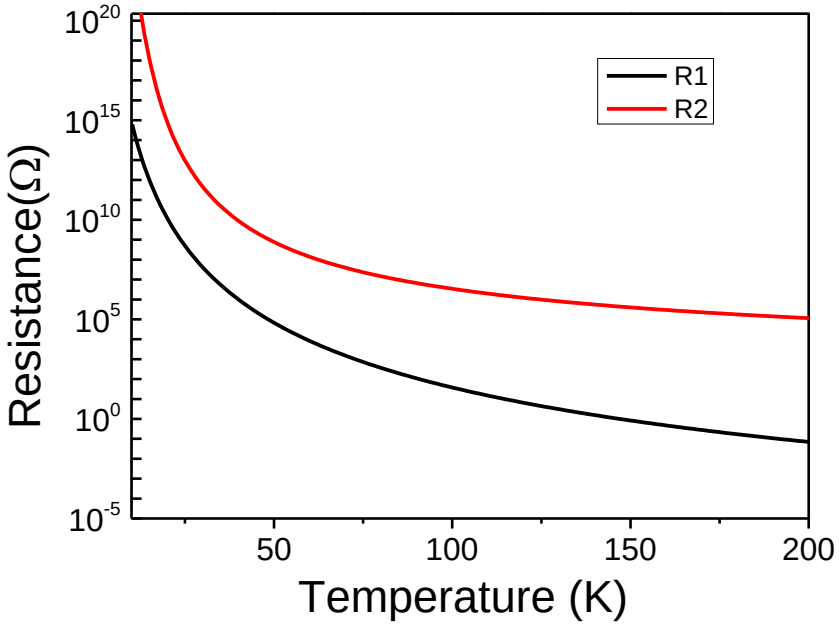


**Figure 5.12** Resistance of $R1$ and $R2$ used in the calculation of of $C_{total}$ and $tan\delta$

The impedance $Z=Z_1-iZ_2$ was calculated as[9]

$$Z_1 - iZ_2 = \frac{R_1}{1+\omega^2 C_1^2 R_1^2} + \frac{R_2}{1+\omega^2 C_2^2 R_2^2} - i\left(\frac{\omega C_1 R_1^2}{1+\omega^2 C_1^2 R_1^2} + \frac{\omega C_2 R_2^2}{1+\omega^2 C_2^2 R_2^2}\right) \tag{5.53}$$

where $Z_1$ and $Z_2$ are the real and imaginary parts of the impedance and $\omega=2\pi f$ is the measurement frequency. For comparison with the measured data, the impedance was converted to $tan\delta$, $R_{total}$ and $C_{total}$ as

$$tan\delta = d = \frac{Z_1}{|Z_2|} \tag{2.54}$$

$$R_{total} = \frac{Z_1^2 + Z_2^2}{Z_1} \tag{2.55}$$

$$C_{total} = \frac{1}{\omega D R_{total}} \tag{2.56}$$

The simulated results of the temperature dependence of capacitance and tanδ were shown in **Figure 5.11**(a,b)(solid lines). The fitting is in good agreement with the measured data, showing two plateaus of capacitance which represent the intrinsic and extrinsic Maxwell-Wagner-type relaxations. The step shifts to higher temperatures with increasing frequency accompanied by a peak in tanδ, which is a common behaviour of Maxwell-Wagner-type relaxations.[11]

To further investigate the nature of the relaxations, the frequency dependence of the tanδ peak position obtained from **Figure 5.16**(b) (open symbol) is shown in **Figure 5.13**. The variation of the peak position follows Arrhenius' law,

$$f = f_0 exp\left(-E_a/k_B T_p\right) \tag{2.57}$$

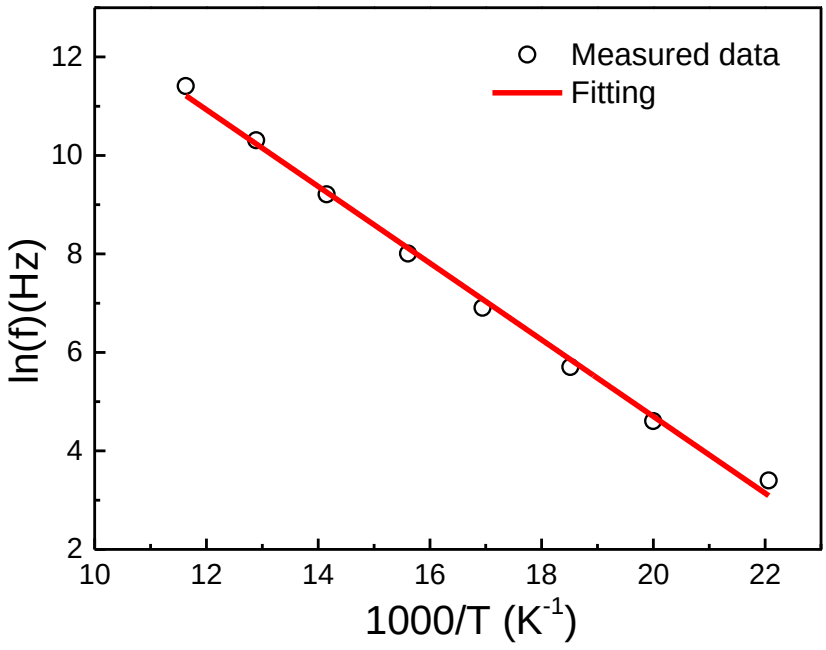


**Figure 5.13** Plot of the peak position extracted from Figure 5.16(b) (open symbols) as a function of the reciprocal temperature. The solid line is a linear fitting according to Arrhenius relation.

where $f_0$ is the relaxation frequency at an infinite temperature and $E_a$ is the activation energy for the relaxation. The value for $E_a$ and $f_0$ are 67 meV and $6.374\times10^8$ Hz, respectively. The values are in good agreement with those of some other perovskite materials in which the Maxwell-Wagner-type relaxation

dominates.[10, 12-13] The activation energy is determined by the Schottky interface between the film and semiconductor Nb:STO substrate.[10]

#### 5.3.3.3 Frequency Dependence of Capacitance

Similarly, the frequency dependence of the capacitance of the device was also measured. **Figure 5.14** shows the frequency dependence of $\varepsilon'$ and $\varepsilon''$ (effective) for the Pd/FVO/Nb:STO junction as measured at various temperatures (open symbols). The plots show a typical signature of relaxation: a stepwise change in $\varepsilon'$ accompanied by a $\varepsilon''$ peak. Increasing the temperature, the peak position of $\varepsilon''$ shifts to the right side. As the relaxation time $\tau$=1/(2$\pi$×frequency), τ becomes smaller at a higher temperature.

Here, we used the empirical Havriliak-Negami(HN) model[14] to analyse the relaxation behaviour. The model is generally used to model the polymeric relaxation behaviour with respect to dielectric data in the frequency domain, and it can be expressed as

$$\varepsilon^* = \varepsilon' - i\varepsilon'' = \varepsilon_\infty + \frac{\varepsilon_0 - \varepsilon_\infty}{[1 + (i\omega\tau)^{1-\alpha}]^\beta} \tag{5.58}$$

where ε* is the complex impedance, $\varepsilon'$ and $\varepsilon''$ are the dielectric constant and dielectric loss, respectively, $\varepsilon_\infty$ and $\varepsilon_0$ are the high- and low-frequency dielectric constants, respectively, i is the characteristic complex number $\sqrt{-1}$, ω is the angular frequency (where $\omega = 2\pi f$), τ is the relaxation time and α and β are the broadening and asymmetry factors of the curves, where $0 < \alpha, \beta \leq 1$.

Within the HN model, the dielectric constant, ε', and loss, ε", can be resolved as

$$\varepsilon' = \varepsilon_\infty + \frac{(\varepsilon_0 - \varepsilon_\infty)cos(\beta\theta)}{\left[1 + 2\omega^\alpha\tau^\alpha cos\left(\frac{\alpha\pi}{2}\right) + \omega^{2\alpha}\tau^{2\alpha}\right]^{\frac{\beta}{2}}} \tag{5.59}$$

and

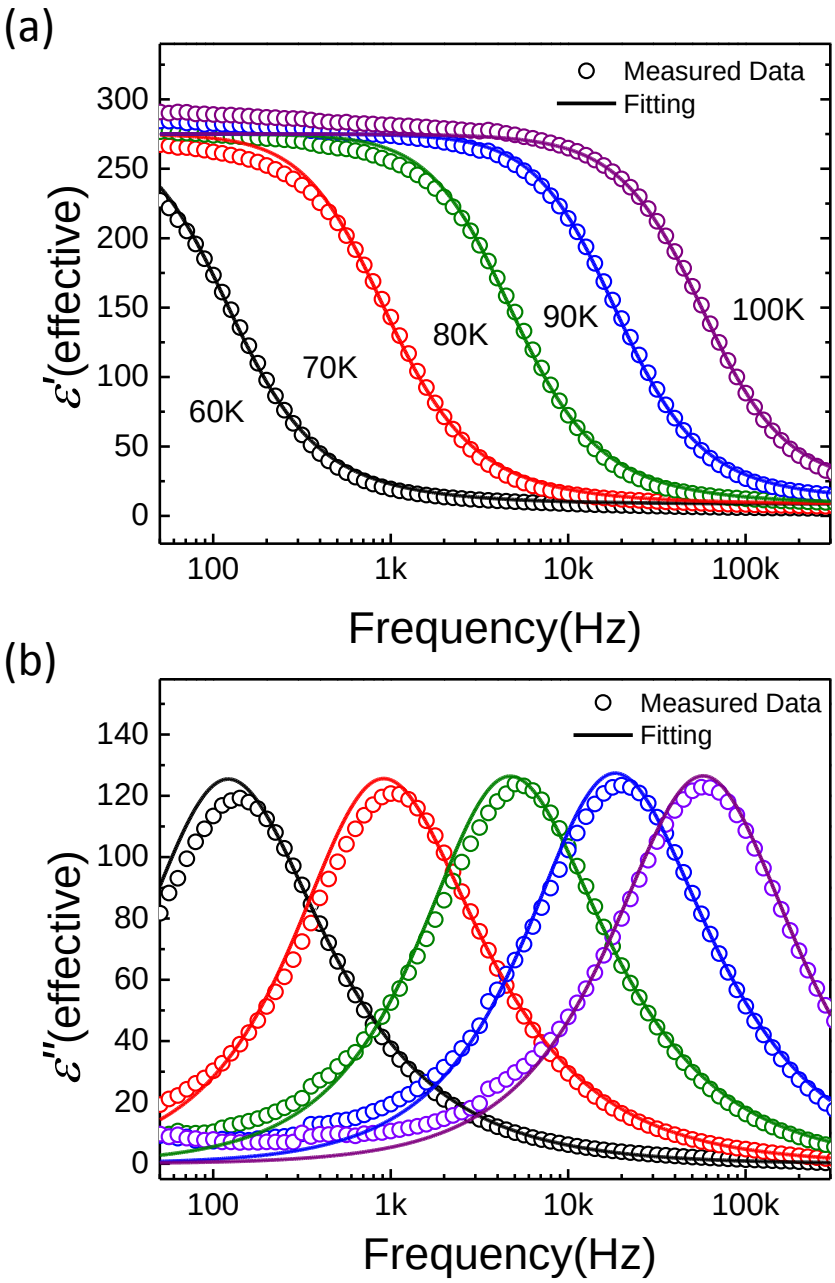


**Figure 5.14** Frequency dependence of $\varepsilon'$ and $\varepsilon''$ for a Pd/FVO/Nb:$SrTiO_3$ junction for several measurement temperatures. The open symbols and solid lines are the measured data and the Havriliak-Negami fitting results, respectively.

$$\varepsilon'' = \frac{(\varepsilon_\infty - \varepsilon_0) sin(\beta\theta)}{\left[1 + 2\omega^\alpha \tau^\alpha cos\left(\frac{\alpha\pi}{2}\right) + \omega^{2\alpha}\tau^{2\alpha}\right]^{\frac{\beta}{2}}} \tag{5.60}$$

with

$$\theta = tan^{-1}\frac{\omega^{\alpha}\tau^{\alpha}sin\left(\frac{\alpha\pi}{2}\right)}{1+\omega^{\alpha}\tau^{\alpha}cos\left(\frac{\alpha\pi}{2}\right)} \tag{2.61}$$

The high- and low-frequency permittivities were estimated from the Cole-Cole plots, shown in **Figure 5.15**. The value of $\varepsilon_{\infty}$ and $\varepsilon_0$ are 8.5 and 278 respectively. By substituting the estimated value of $\varepsilon_{\infty}$ and $\varepsilon_0$ into Eq.5.11 and Eq.5.12, we acquired the optimized value of $\alpha$, $\beta$ and $\tau$. The fitting results are shown in **Figure 5.14** as solid lines. As we can see, the measured data at all temperatures are fitted excellently well by the HN function.

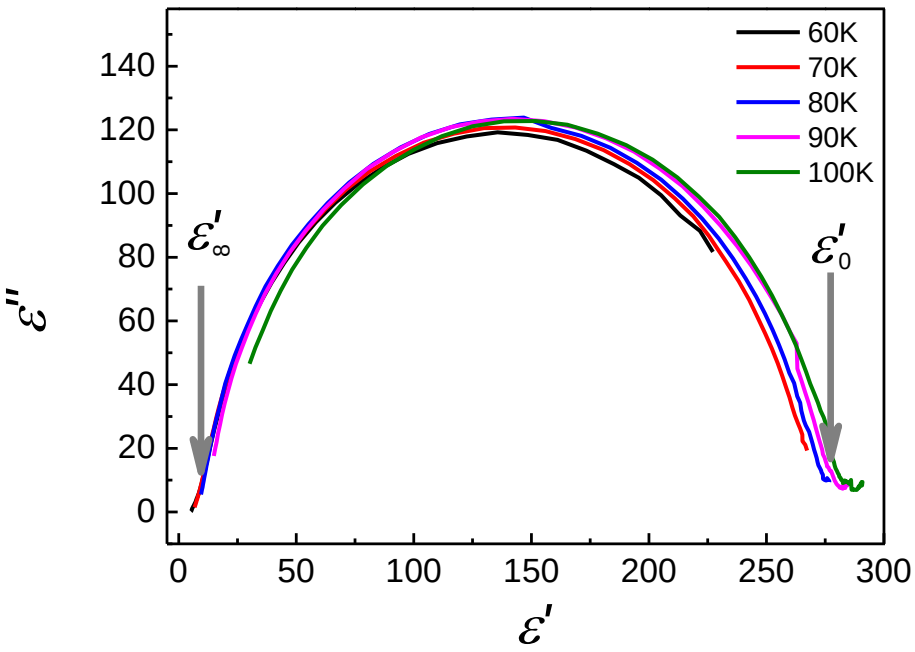


**Figure 5.15** Cole-Cole plot of $\varepsilon'$ and $\varepsilon''$.

The HN model can be recast to allow the computation of the relaxation time as

$$\tau = \frac{1}{i\omega}exp\left[\frac{1}{\alpha}log\left\{exp\left|\frac{1}{\beta}log\left(\frac{\varepsilon_0-\varepsilon_{\infty}}{\varepsilon^*-\varepsilon_{\infty}}\right)\right|-1\right\}\right] \tag{5.62}$$

and can be expressed by an Arrhenius representation

$$\tau = \tau_0 exp\left(\frac{E_a}{k_B T}\right) \tag{5.63}$$

where $\tau_0$ is a pre-factor, $k_BT$ is the thermal energy, and $E_a$ is the activation energy.

The relaxation time of different measurement temperatures, acquired from the HN function fitting, was plotted against the reciprocal temperature in **Figure 5.16** (open symbols). The activation energy $E_a$ is estimated from the slope of a linear fitting of the plot and the value is 81 meV. The intercept of the fitting line yields a pre-factor value of $\tau_0$=0.25 ns, corresponding to an attempt frequency of 4×10$^9$ Hz. Both $E_a$ and $\tau_0$ are close to the values which were yielded from the Arrhenius fitting of the temperature dependence of the capacitance data, as discussed earlier in this chapter.

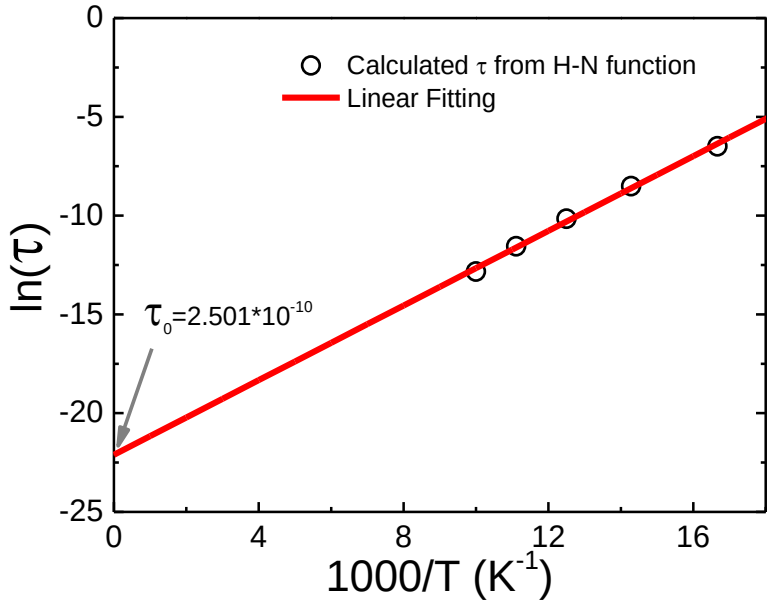


**Figure 5.16** Arrhenius plot of relaxation times obtained from the Havriliak-Negami fitting. The estimated activation energy and pre-factor are 81 meV and 0.25 ns, respectively.

## 5.3.4 Magnetocapacitance

The above characterization of the dielectric properties was then extended to understand the magneto(di)electric effect in these films. The magnetocapacitance behaviour of single crystal FVO has previously been reported,[15] but has not been studied for thin films. The magnetoelectric coupling of the low temperature tetragonal phase in our FVO films was studied by

measuring the capacitance of the Pd/FVO/Nb:STO junction as a function of an applied magnetic field (up to 0.7 T) at 10 K, well below the structural and ferrimagnetic transitions. At this temperature, the capacitance is dominated by the intrinsic relaxation[9] as discussed previously, which means the interface contribution can be neglected. The *effective*[1] dielectric constant of FVO film is calculated as a simple parallel plate capacitor and the magnetocapacitance (MC) is defined as[16]

$$MC = \frac{\varepsilon'_H - \varepsilon'_{H=0}}{\varepsilon'_{H=0}} \times 100 \quad (5.64)$$

As shown in **Figure 5.17**(a), by applying an out-of-plane magnetic field ($\boldsymbol{B}//\boldsymbol{E}$), MC decreases with the increasing of $\boldsymbol{B}$. A clear hysteresis loop of $MC$ is also observed. A similar shaped hysteretic MC effect was reported on single crystal FVO samples[15] by Kismarahardja et al. However in their case the effect was explained based purely on the geometrical effect; that is, when the random oriented magnetic domains are aligned with $\boldsymbol{B}$, the sample expands along the magnetic field direction and contracts perpendicularly to the magnetic field, leading to a decreasing of capacitance when an out-of-plane magnetic field ($\boldsymbol{B}//\boldsymbol{E}$) is applied, and an increase when applying an in-plane magnetic field ($\boldsymbol{B}\perp\boldsymbol{E}$). An important distinction with the thin film samples studies here, is that in their case the out-of-plane c-axis was smaller than the in-plane a-axis. In the FVO thin films investigated here, the $MC$ hysteresis is only observed when the magnetic field is along the out-of-plane direction, indicating a reorientation of magnetic anisotropy in the thin film FVO. Similar behaviour has been reported on other spinel magnetics, namely cobalt ferrite, and the driven force of the phenomenon has proved to be the lattice strain.[17-19] In the FVO thin films investigated here, the $MC$ hysteresis is only observed when the magnetic field is along the OOP direction, indicating a magnetic anisotropy in the thin film FVO. No $MC$ effect is observed in the **Figure 5.17**(c). Although the IP coercive field is smaller than that of OOP, the magnetic field we applied for $MC$ measurement is lower than either of them. It is most likely

[1] Although the intrinsic capacitance dominates at this temperature the measured dielectric permittivity is still an effective one.

that the $MC$ effect we detected here originates from magnetoelectric coupling of the 'phase B', as we discussed earlier in Chapter 4, which has a weak coercive field and only appears in the OOP curves.

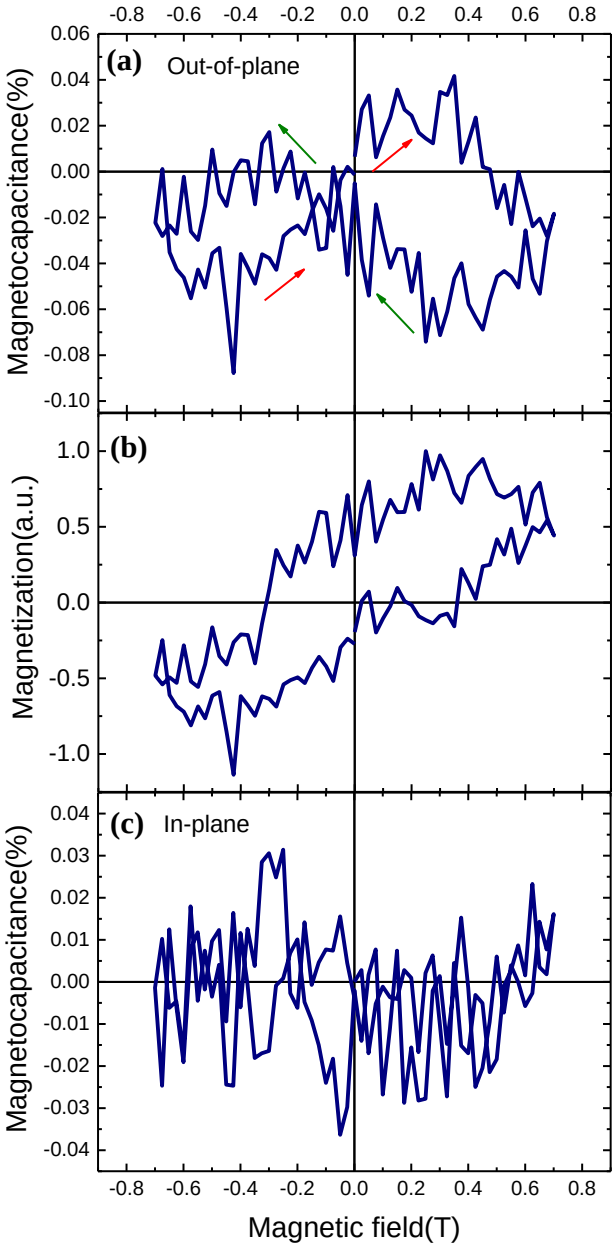


**Figure 5.17** Isothermal magnetocapacitance (measured at 1 kHz) effect at 10 K during increasing and decreasing out-of-plane (a) and in-plane (c) magnetic field in Pd/FVO/Nb:STO junction. The arrows mark the direction (increasing and decreasing) of the magnetic field. (b) Converted magnetocapacitance signal for FVO based on the $MC \sim M^2$ relation proposed in Ref[20].

The hysteresis loop of $MC$ may originate from the aligning of the magnetic domains to the direction of the applied magnetic field as we observed in the MFM

measurements. A strong correspondence between the magnetocapacitance signal and the magnetization, namely, $M^2 \sim MC$, in FVO bulk materials was reported by Kismarahardja et al. [15] and Takei et al.[20]. In general, the extreme of the loop corresponds to the coercive field $\mathbf{B}_c$ where the magnetization $M$=0. The hysteresis loop of MC is then converted to the magnetization hysteresis loop, as shown in **Figure 5.17**(b) using $M \sim MC^{1/2}$ where the sign of the magnetization between $B_c$ is reversed. Since the MC effect corresponds to the phase B in the sample, we find that the out-of-plane $\mathbf{B}_c$ of the 'phase B' in a 100-nm-thick FVO film at 10 K is ~0.35 T.

## 5.4 Summary

In this chapter, we investigated the electrical properties of the FVO films. The resistivity of the film was measured and fitted with the VRH model. A Pd/FVO/Nb:STO junction was used to measure the dielectric properties of the film. The temperature and frequency dependence of capacitance shows that at low temperature, T < 40 K, the intrinsic relaxation contributes most to the total capacitance of the device, while at a higher temperature, a Maxwell-Wagner type relaxation is dominant, which is deduced from the Schottky interface between the film and semiconductor Nb:STO substrate. The calculated activation energy $E_a$ and relaxation frequency $f_0$ are 67 meV and $6.374\times10^8$ Hz, respectively. The magnetocapacitance effect along out-of-plane direction was observed by measuring the capacitance as a function of applied magnetic field. The anisotropy of the $MC$ effect of the device is similar to the magnetic anisotropy of the FVO film and can possibly be attributed to the presence of the $Fe^{3+}$ excess 'phase B' in the system.

References

[1] R. M. Kusters, J. Singleton, D. A. Keen, R. Mcgreevy, W. Hayes,Magnetoresistance Measurements on the Magnetic Semiconductor Nd0.5Pb0.5MnO3, Physica B 1989, 155, 362.
[2] G. J. Snyder, R. Hiskes, S. DiCarolis, M. R. Beasley, T. H. Geballe,Intrinsic electrical transport and magnetic properties of La0.67Ca0.33MnO3 and La0.67Sr0.33MnO3 MOCVD thin films and bulk material, Phys. Rev. B 1996, 53, 14434.
[3] M. Viret, L. Ranno, J. M. D. Coey,Colossal magnetoresistance of the variable range hopping regime in the manganites, J. Appl. Phys. 1997, 81, 4964.
[4] A. G. Chynoweth,Dynamic Method for Measuring the Pyroelectric Effect with Special Reference to Barium Titanate, J. Appl. Phys. 1956, 27, 78.
[5] R. Takahashi, I. Ohkubo, K. Yamauchi, M. Kitamura, Y. Sakurai, M. Oshima, T. Oguchi, Y. Cho, M. Lippmaa,A-site-driven ferroelectricity in strained ferromagnetic La2NiMnO6 thin films, Phys. Rev. B 2015, 91.
[6] R. Schmidt, J. Ventura, E. Langenberg, N. M. Nemes, C. Munuera, M. Varela, M. Garcia-Hernandez, C. Leon, J. Santamaria,Magnetoimpedance spectroscopy of epitaxial multiferroic thin films, Phys. Rev. B 2012, 86.
[7] L. Pintilie, I. Vrejoiu, D. Hesse, M. Alexe,The influence of the top-contact metal on the ferroelectric properties of epitaxial ferroelectric Pb(Zr0.2Ti0.8)O-3 thin films, J. Appl. Phys. 2008, 104.
[8] P. Lunkenheimer, R. Fichtl, S. G. Ebbinghaus, A. Loidl,Nonintrinsic origin of the colossal dielectric constants in CaCu3Ti4O12, Phys. Rev. B 2004, 70, 172102.
[9] R. Schmidt, J. Ventura, E. Langenberg, N. M. Nemes, C. Munuera, M. Varela, M. Garcia-Hernandez, C. Leon, J. Santamaria,Magnetoimpedance spectroscopy of epitaxial multiferroic thin films, Phys. Rev. B 2012, 86, 035113.
[10] R. Takahashi, Y. Cho, M. Lippmaa,Interfacial capacitance between a ferroelectric Fe3O4 thin film and a semiconducting Nb:SrTiO3 substrate, J. Appl. Phys. 2015, 117, 014104.
[11] C. C. Wang, H. B. Lu, K. J. Jin, G. Z. Yang,Temperature-dependent dielectric strength of a Maxwell-Wagner type relaxation, Mod. Phys. Lett. B 2008, 22, 1297.
[12] L. Zhang, Z. J. Tang,Polaron relaxation and variable-range-hopping conductivity in the giant-dielectric-constant material CaCu3Ti4O12, Phys. Rev. B 2004, 70, 174306.
[13] C. C. Wang, C. M. Lei, G. J. Wang, X. H. Sun, T. Li, S. G. Huang, H. Wang, Y. D. Li,Oxygen-vacancy-related dielectric relaxations in SrTiO3 at high temperatures, J. Appl. Phys. 2013, 113, 094103.
[14] Havrilia.S, S. Negami,A Complex Plane Representation of Dielectric and Mechanical Relaxation Processes in Some Polymers, Polymer 1967, 8, 161.
[15] A. Kismarahardja, J. S. Brooks, H. D. Zhou, E. S. Choi, K. Matsubayashi, Y. Uwatoko,Dielectric properties of single crystal spinels in the series FeV2O4, MnV2O4, and CoV2O4 in high magnetic fields, Phys. Rev. B 2013, 87, 054432.
[16] G. Catalan,Magnetocapacitance without magnetoelectric coupling, Appl. Phys. Lett. 2006, 88, 102902.
[17] A. Lisfi, C. M. Williams, L. T. Nguyen, J. C. Lodder, A. Coleman, H. Corcoran, A. Johnson, P. Chang, A. Kumar, W. Morgan,Reorientation of magnetic anisotropy in epitaxial cobalt ferrite thin films, Phys. Rev. B 2007, 76.
[18] S. Matzen, J. B. Moussy, R. Mattana, F. Petroff, C. Gatel, B. Warot-Fonrose, J. C. Cezar, A. Barbier, M. A. Arrio, P. Sainctavit,Restoration of bulk magnetic properties by strain engineering in epitaxial CoFe2O4 (001) ultrathin films, Appl. Phys. Lett. 2011, 99.

[19] M. A. Tanaka, K. Harada, M. Takemura, K. Mibu, J. Inoue,Nonlinear strain dependence of magnetic anisotropy in CoFe2O4 films on MgO(001) substrates, J. Appl. Phys. 2014, 115.
[20] H. Takei, T. Suzuki, T. Katsufuji,Nonvolatile memory effect of capacitance in polycrystalline spinel vanadate, Appl. Phys. Lett. 2007, 91, 072506.

# CHAPTER SIX

# 6 STUDY OF ELECTRICAL PROPERTIES OF COBALT CHROMITE FILMS

## 6.1 Synopsis

The previous chapters focused on the magnetic and electric properties of non-collinear multiferroic spinel FVO thin films, as well as the coupling between the two orders at low temperatures. This chapter is focused on another non-collinear multiferroic spinel cobalt chromite, $CoCr_2O_4$(CCO), which has been theoretically[1-2] and experimentally[3] proven to have an intrinsic magneto-electric coupling in its low temperature ferrimagnetic phase. Firstly, the synthesis and structural characteristic of CCO thin films on STO and LSMO buffered STO substrates is presented. A shift of lattice parameter, caused by changing the oxygen pressure during the PLD process, was observed. Then, the ferroelectric behaviour of the film was investigated by piezoelectricity force microscopy (PFM) at room temperature, in its paramagnetic phase. Although the PFM images show reversible contrast, this is most likely induced by the charges accumulated at the interface of the CCO and LSMO caused by the oxygen vacancies at the interface. Interestingly, we also observed a resistivity switching behaviour of the CCO/LSMO/STO samples by conductivity force microscopy (CFM) as well as by conducting conventional I-V tests. It is proposed that the switching of the resistivity is due to the migration of the vacancy at the CCO/LSMO interface driven by the external electric field.

## 6.2 Synthesis and Structural Characterization of Cobalt Chromite Films

PLD was employed as the growth method of the CCO films and $CoCr_2CO_4/La_{0.67}Sr_{0.33}MnO_3$ (CCO/LSMO) heterostructure. The deposition system was described in Chapter 3. (001) orientated single crystal $SrTiO_3$ with a miscut angle of ~ 1° was used as substrate. Substrates were pre-treated and annealed as described in Chapter 3. The targets used in the deposition were commercial CCO and LSMO targets supplied by Kurt J. Lesker with 99.9 wt% purity and 98% density. Laser energy density was set to 2 J/cm$^2$ at 2 Hz, while the deposition temperature was 500 °C.

To find out the proper ambient oxygen pressure for the deposition, we ran two depositions, one under 20 mTorr and the other under $1\times10^{-5}$ Torr oxygen pressures. The XRD 2-θ scan patterns of the samples are shown in **Figure 6.1.**

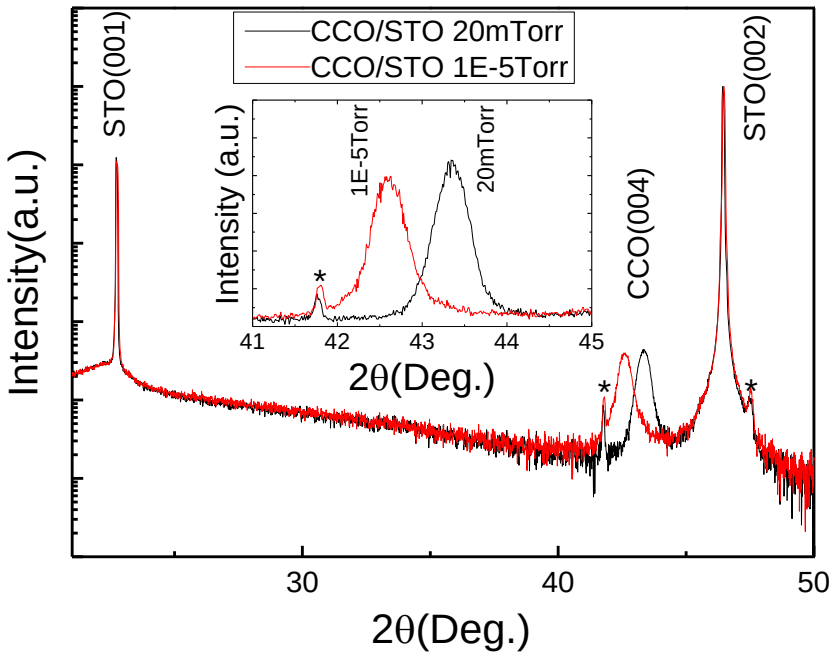


**Figure 6.1** 2-θ scan of CCO/STO samples grown under different $O_2$ pressure.

We can find the (004) peak of CCO in both patterns, while the peak positions of the 2 samples deposited under different pressures are obviously different. The

peak positions of the low and high pressure samples are 42.6 ° and 43.35 ° respectively, while that of the bulk material is 43.4 °. The low pressure sample shows a considerably large shift towards to the left side, indicating a larger out-of-plane lattice parameter which may be caused by the higher oxygen vacancy density, since it was grown in an oxygen deficiency ambience. However, the 20 mTorr sample shows a lattice parameter very close to that of the bulk material, indicating less stress and defects in the sample, as compared to the low pressure sample. To further confirm the structure of epitaxial CCO film, we checked the position of the (311) diffraction peak, as shown in **Figure 6.2**, and it showed a very similar 2-θ degree to that of the powder diffraction data, which confirms the CCO structure of the 20 mTorr CCO/STO sample.

We used AFM to observe the topography of the sample and the image is shown in **Figure 6.3**. As can be seen, the surface of the CCO/STO sample is particle free and smooth with an Rms = 0.85 nm.

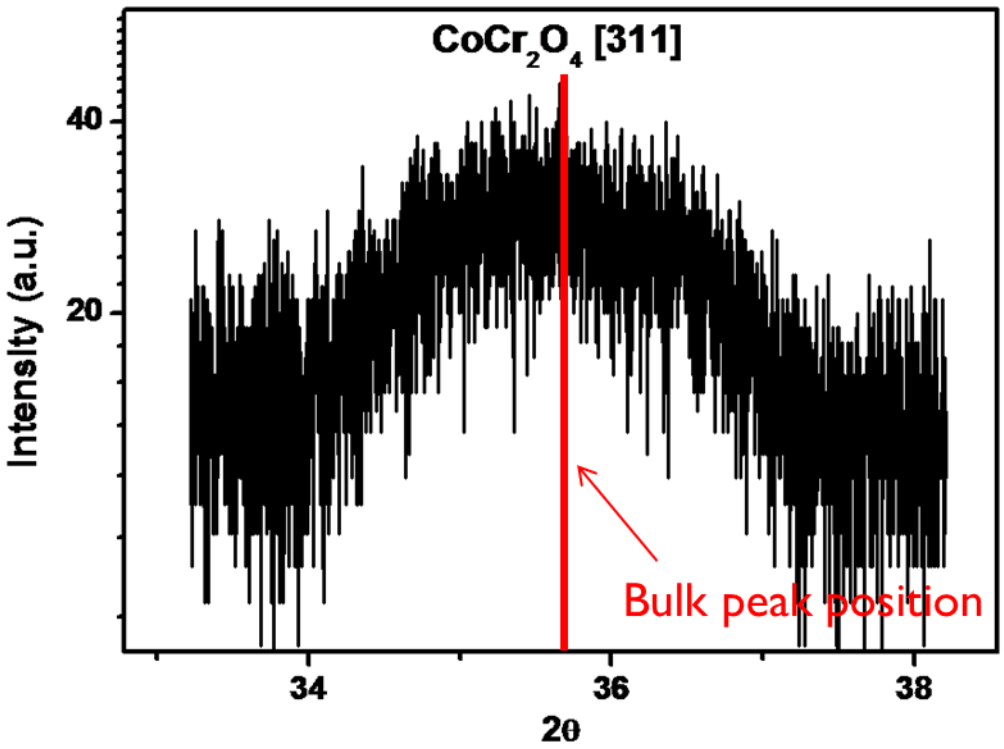


**Figure 6.2** XRD 2-θ scan of 20 mTorr CCO/STO sample around (311) peak.

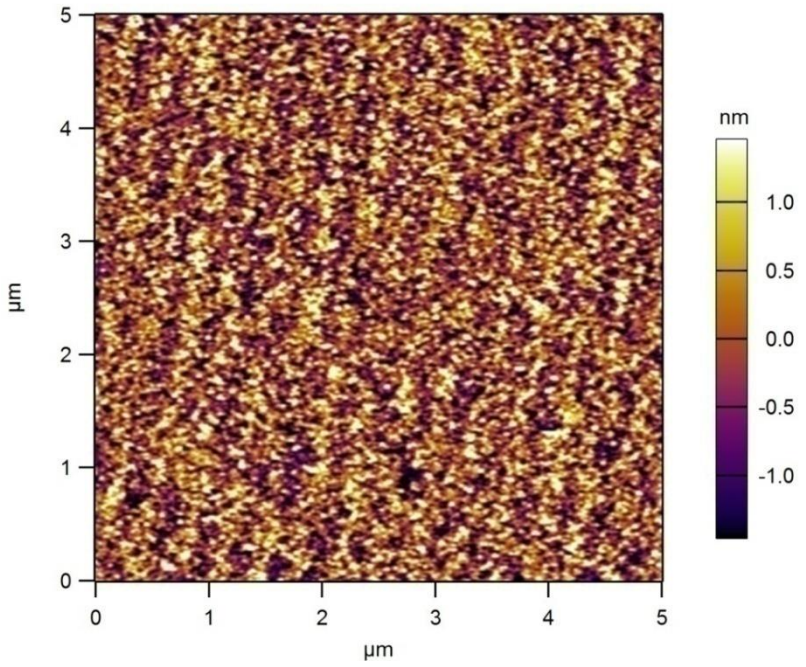


**Figure 6.3** AFM topography image of 20 mTorr CCO/STO sample.

To fabricate the CCO/LSMO heterostructure, a 40-nm-thick LSMO layer was grown on a STO substrate before the deposition of CCO thin film. The growth conditions of the LSMO layer are listed in **Table 6.1**.

| Oxygen Pressure | Substrate Temperature | Laser energy | Frequency | Number of Pulses |
|---|---|---|---|---|
| 100 mTorr | 750 °C | 200 mJ | 2 Hz | 2400 |

**Table 6.1** Parameters of the LSMO growth.

CCO films were then deposited on the top of the LSMO layer under different oxygen pressures, 20 and 100 mTorr, respectively. The XRD 2-θ scan patterns of the two samples are shown in **Figure 6.4**. We can clearly see the LSMO [001] peaks and CCO (004) peaks from the XRD pattern without any evidence of secondary phases. The CCO (004) peaks of the two samples are shown in the inset of **Figure 6.4.**

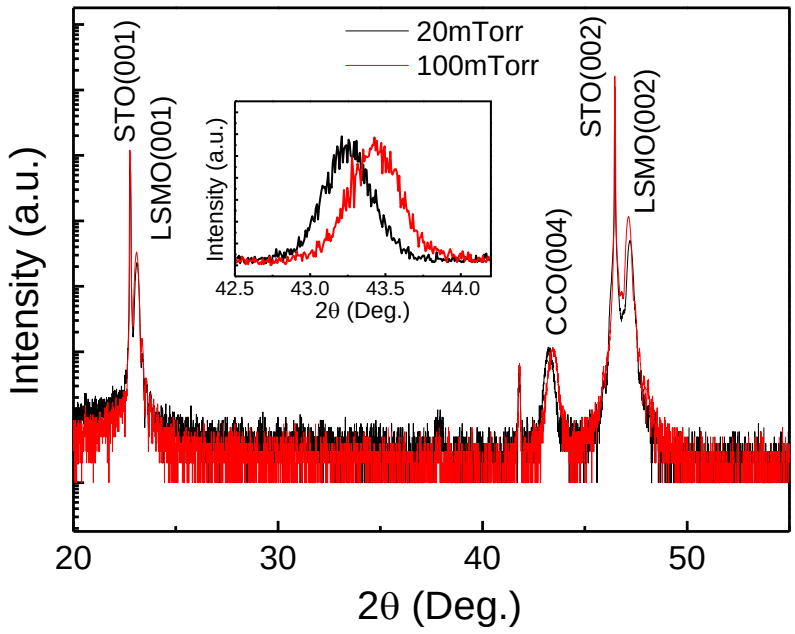


**Figure 6.4** 2-θ plots of CCO/LSMO/STO samples. Inset: CCO (004) peaks.

The topography images of CCO/LSMO/STO samples are shown in **Figure 6.5**. Both samples are particle free and smooth. The 20 mTorr sample is smoother than the 100 mTorr sample.

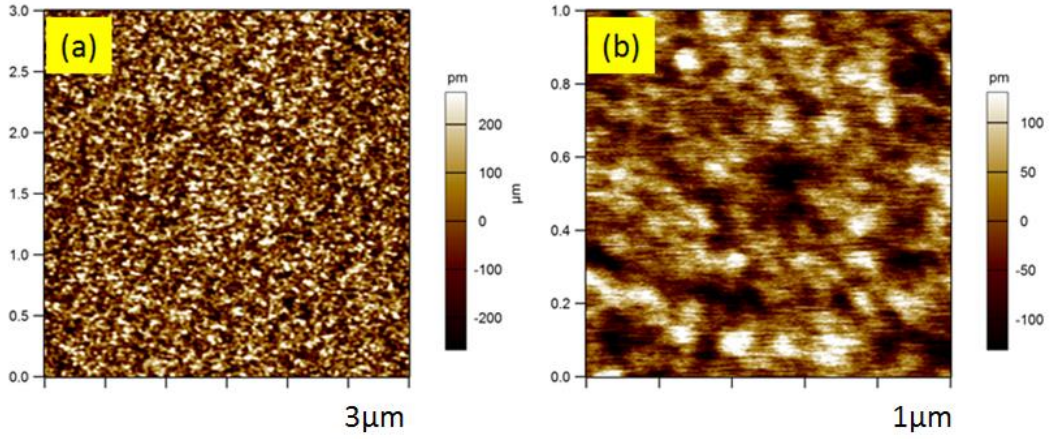


**Figure 6.5** Topography images of 20 mTorr (a) and 100 mTorr (b) CCO/LSMO/STO samples.

## 6.3 Investigation of Polarization of CCO/LSMO heterostructure at Room Temperature

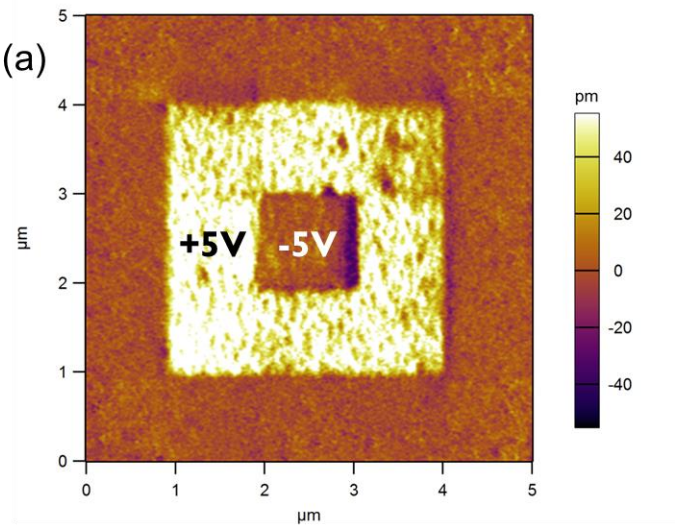


**Figure 6.6** PFM, amplitude (a) and Phase (b), images of a CCO/LSMO/STO sample. Strong contrast shows in both phase and amplitude signals.

Spinel CCO is a ferrimagnetic with a Néel temperature of ~ 94 K. It is experimentally proven that at lower temperature regimes, T < ~28 K where its magnetic moments of Co and Cr are canted and form a canted conical magnetic ordering. CCO shows a polar ordering which is coupled intrinsically with the

magnetic ordering and can be reversed by an applied magnetic field. Here, we attempt to probe the polarization of the CCO/LSMO heterostructure at room temperature, in its paramagnetic phase, with piezoresponse force microscopy (PFM). Theoretically there is no polarization in its paramagnetic phase. Surprisingly, as shown in **Figure 6.6**, a strong contrast in both phase and amplitude signals of the PFM image can be observed after applying an electric field with different direction on the sample. Hysteresis loops were also acquired by PFM spectroscopy, as shown in **Figure 6.7**. A clear Hysteresis loop in phase and butterfly shaped loop in amplitude were observed. Generally, in a ferroelectric material, areas with different colours in the PFM images represent domains with different directions of polarization and can be regarded as a proof of ferroelectricity. Since CCO is not known as either ferroelectric or piezoelectric at room temperature, in its paramagnetic phase, there should not be any ferroelectricity induced by magnetic ordering. Thus we suspect that factors other than spontaneous polarization in CCO induce the PFM signals.

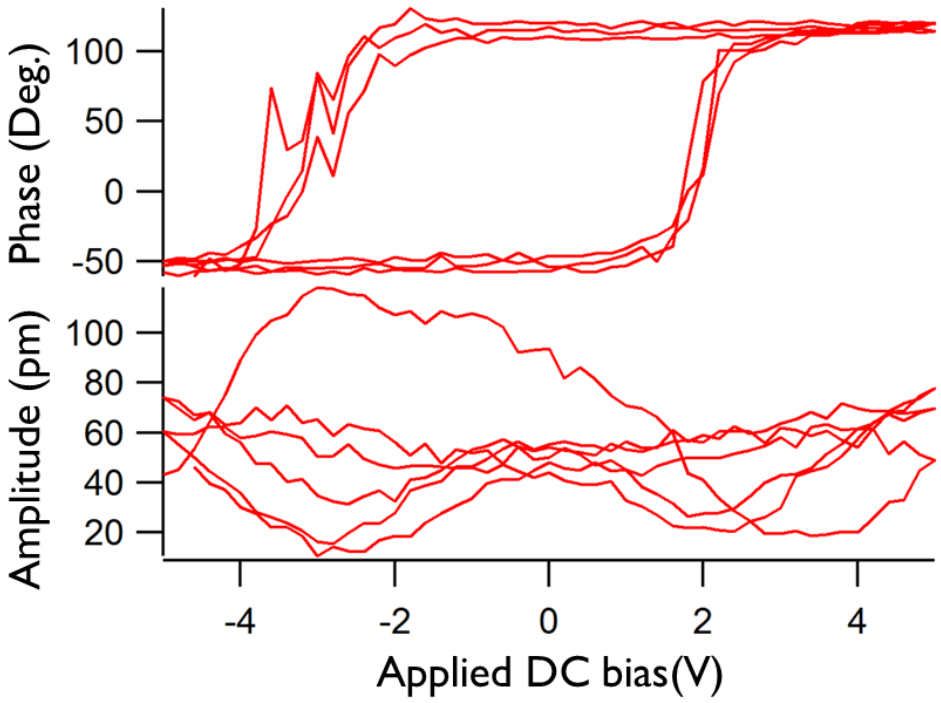


**Figure 6.7** Hysteresis loops acquired by PFM spectroscopy.

First we measure the PFM on a LSMO/STO sample which was grown under the same conditions as a CCO/LSMO/STO sample, and observed that there was no mechanical response to the electric field, as shown in **Figure 6.8**, which indicates that the PFM signal is induced by either the CCO layer or the CCO/LSMO interface.

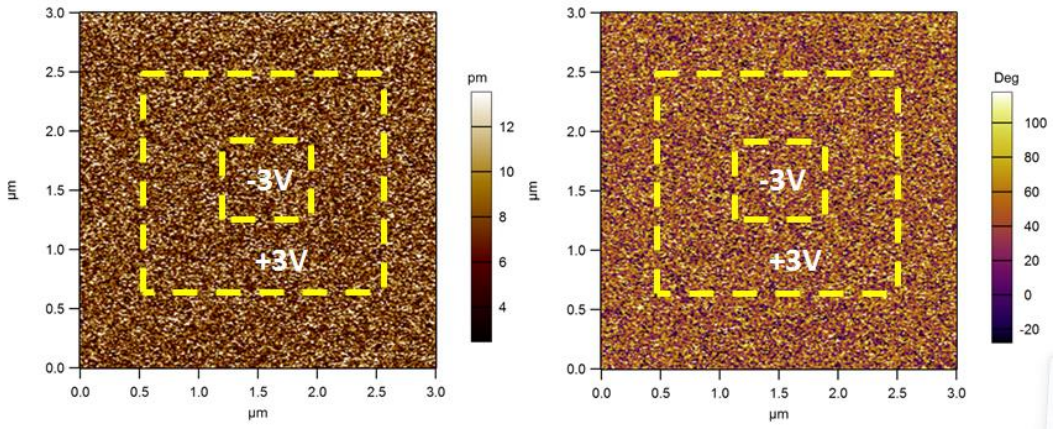


**Figure 6.8** The PFM images of a 40-nm-thick LSMO/STO sample.

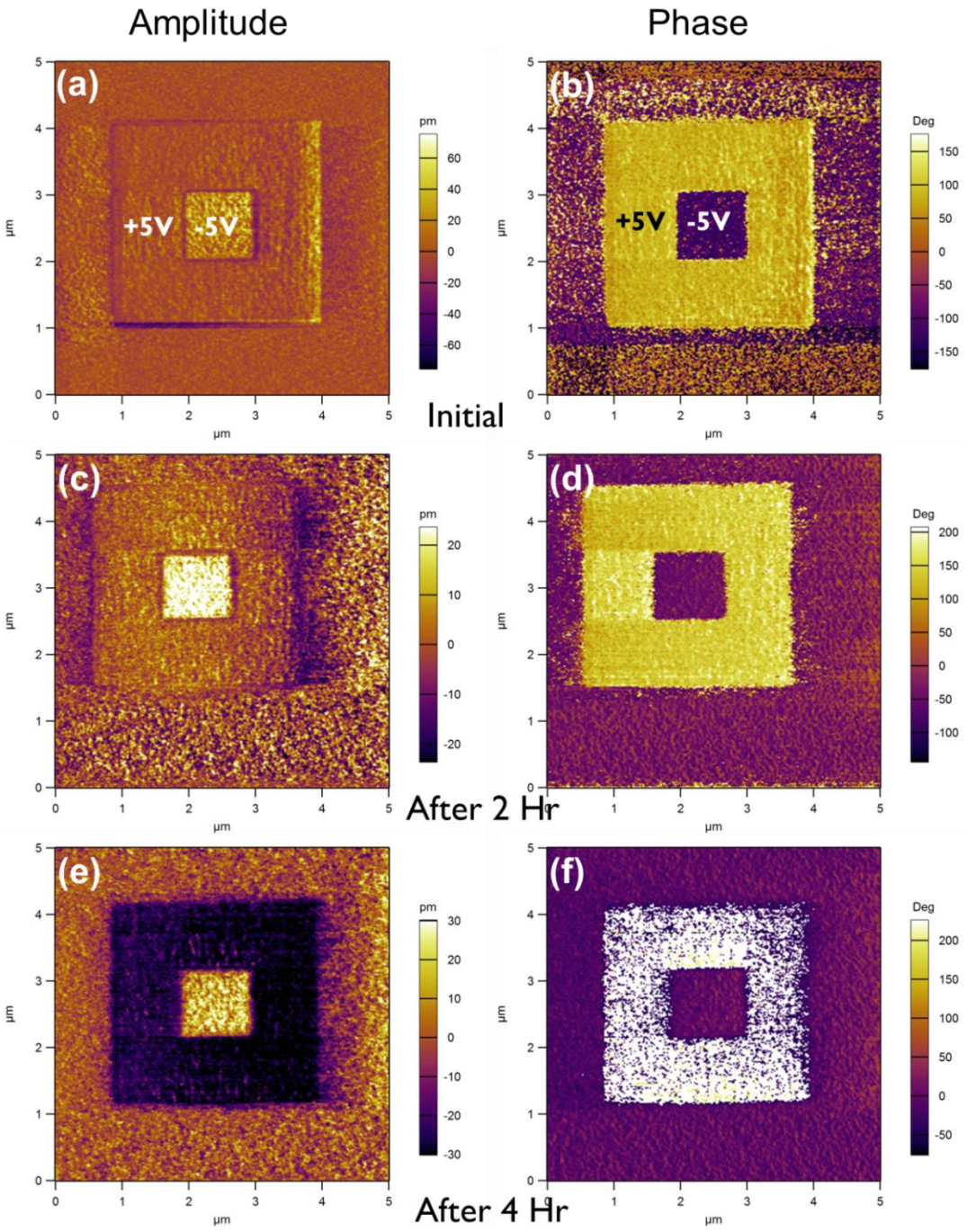


**Figure 6.9** PFM images of a 20 mTorr CCO/LSMO/STO sample. (a, c, d): amplitude; (b, d, f): phase.

It is reported that some materials without spontaneous polarization can also show such contrast in their PFM images.[4] One possibility is that electric charges can remain at the sample surface where the electric field was applied, and induce some response during the PFM scan. One way to identify this kind of charge induced signal is to scan the sample after a certain amount of time, as the charge

accumulated at the sample surface will disappear and the response will be gone. We then conducted the PFM scan 2 and 4 hours after we applied the electric field, as shown in **Figure 6.9**. The signal stays, and both the 2 and 4 hour images show strong contrasts, indicating that the PFM signal may not be induced by the surface charge.

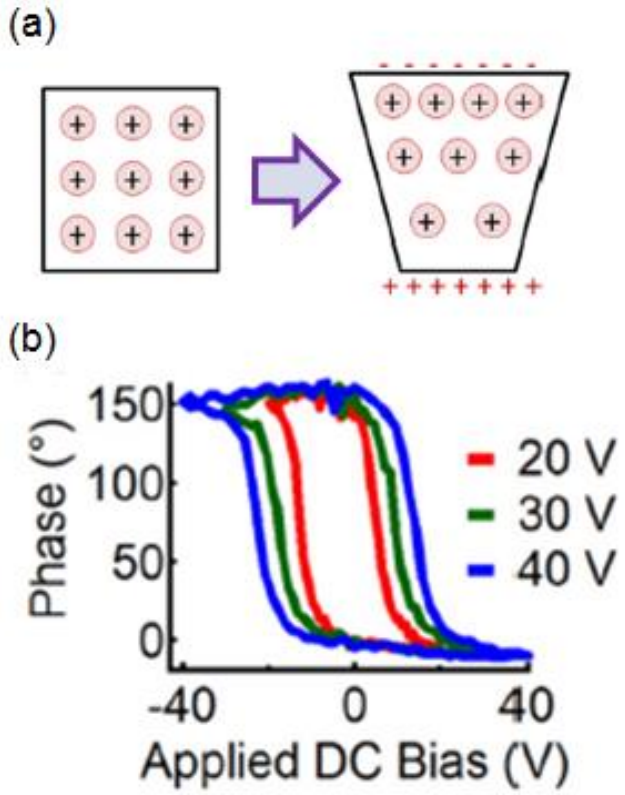


**Figure 6.10** (a) Schematics of microscopic mechanisms of electrochemical induced electromechanical coupling; (b) hysteresis loops of soda-lime glass. Adapted from Ref.[4]

The electromechanical coupling of a material, such as soda-lime glass[4], could be related to dipoles induced by ionic motion under an external electric field, as shown in **Figure 6.10**(a). This kind of system can cause much confusion as it possesses mixed characteristics of both polar and electrochemical systems. However, in such systems, the coercive field is usually not well defined. Because a higher applied electric field would induce larger extents of ionic diffusion, which further opens the hysteresis loop with increased max voltage. Hence the coercive field changes with the changing maximum voltage which can be observed in glass, as shown in **Figure 6.10**(b). So, we can test the coercive field of CCO/LSMO/STO

samples to check whether the piezoresponse signal is induced from ferroelectricity or ionic motion. **Figure 6.11** shows the hysteresis loops in phase signals of 20 mTorr and 100 mTorr CCO/LSMO samples acquired by PFM spectroscopy. As can be seen, in both samples, the hysteresis loop opens further as the maximum voltage is increased, a very similar behaviour compared to that of soda-lime glass, as shown in **Figure 6.10**(b), which has an electromechanical coupling due to ionic motion being driven by external electric fields.

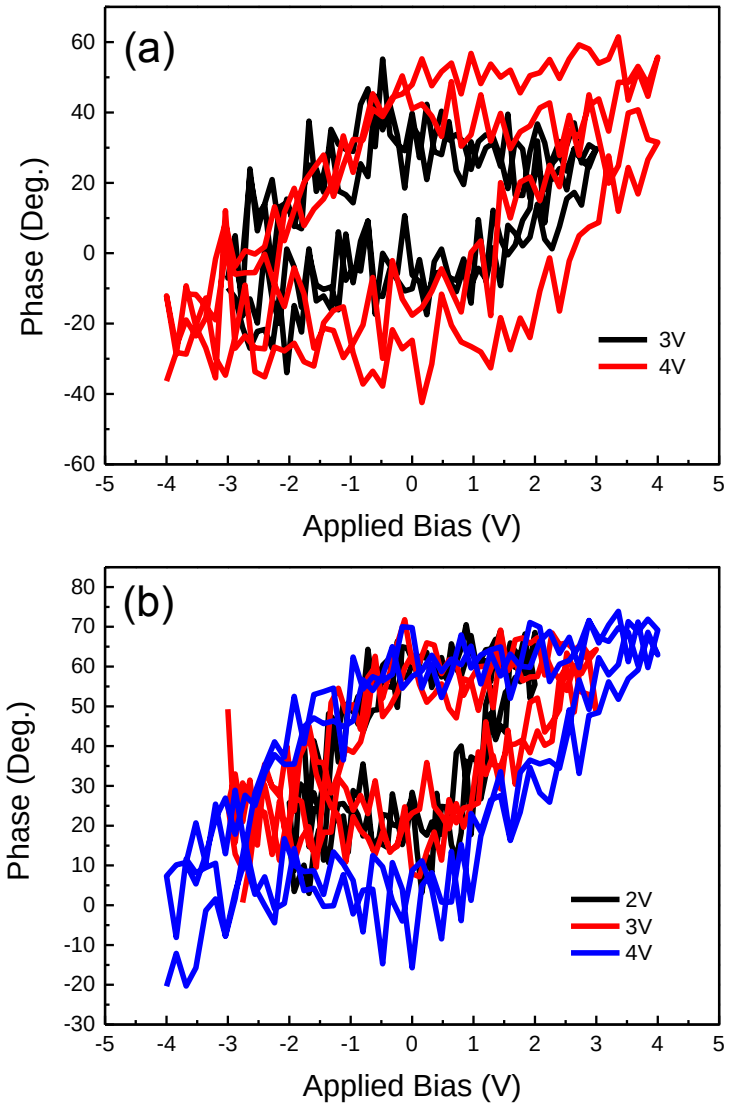


**Figure 6.11** Hysteresis loops of CCO/LSMO/STO samples with different maximum applied bias. (a) 20 mTorr sample and (b) 100 mTorr sample.

## 6.4 Resistivity Switching Behaviour of CCO/LSMO Heterostructure

In the last section, ionic motion was found in the CCO/LSMO heterostructure which induced piezoresponse in the sample. The ionic motion can also induce other phenomena such as Resistivity switching (RS). RS is an interesting phenomenon which has a wide range of applications, such as creating non-volatile memories. It has been demonstrated and analyzed in several non-magnetic and magnetic oxide systems,[5-7] among them, some Spinal Ferrite/LSMO heterostructures, such as $NiFe_2O_4$/LSMO[8] and $CoFe_2O_4$/LSMO,[9] which show a very efficient spin filtering effect at room temperature. In this section, the RS behavior of CCO/LSMO heterostructure is investigated by conducting-AFM (C-AFM) and Current Perpendicular to Plane (CPP) $I$-$V$ measurements.

The C-AFM of the 40-nm-thick 20 mTorr CCO/LSMO/STO sample after applied ± 5 V on different areas (marking in dashed box) is shown in **Figure 6.12**(a). As can be seen, the current at the - 5 V area is lower (with higher resistivity) while the current at + 5 V area is higher (with lower resistivity) than the virgin state, which indicates a RS driven by applied voltage. The signal point I-V curve taken by C-AFM with a voltage sweep between ± 5 V is shown in **Figure 6.12**(b). A RS, from high resistivity to low resistivity, is seen towards positive polarity (LSMO + V terminal) at a threshold voltage ~ 4.5 V, while a reverse transition, from low resistivity to high resistivity, occurs in the negative bias cycle, though it is not as sharp as the positive cycle. **Figure 6.13** shows the $I$-$V$ curves of two CCO/LSMO/STO samples with different CCO thicknesses (40 nm and 60 nm) performed by means of a probe station. 500 μm × 500 μm Indium electrodes were deposited on the top of the CCO, which acts as the grounded top contact, and an LSMO layer was used as the bottom electrode by which the bias voltage was applied. Both I-V curves show a similar RS behaviour as we observed via C-AFM, and they are almost identical to each other, indicating that the RS of CCO/LSMO heterostructure is independent on the thickness of the CCO layer, which implies that it is a purely interfacial phenomenon. The diode-like rectifying characteristics observed here can be attributed to the formation of Schottky barrier at the metal-manganite

interfaces, particularly in the case of $Pr_{0.7}Ca_{0.3}MnO_3$ (PCMO).[10] A similar rectifying characteristic was also found in the $CoFe_2O_4$/LSMO heterostructure.[11]

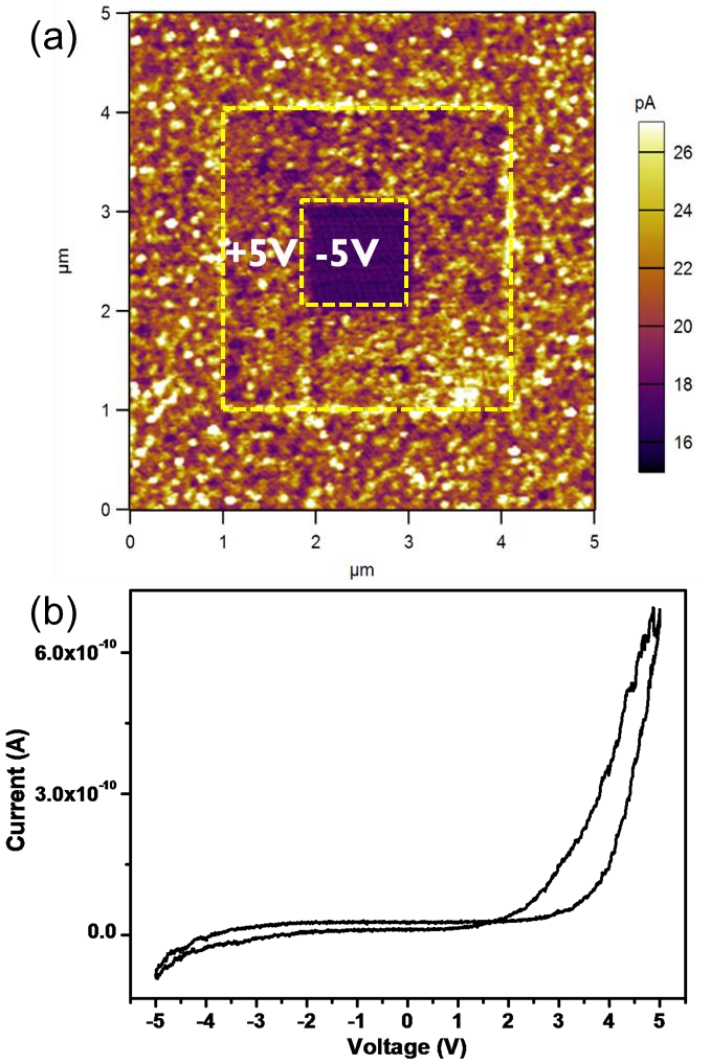


**Figure 6.12** (a) C-AFM of the 40-nm-thick 20 mTorr CCO/LSMO/STO sample. (b) Single point *I-V* curve taken by C-AFM.

The observed RS phenomenon of CCO/LSMO heterostructure can be explained reasonably well using the model proposed in Ref.[11] $La_{0.67}Sr_{0.33}MnO_3$ is a ferromagnetic conductor at room temperature, due to its large bandwidth and nearly linear $Mn^{3+}$-O-$Mn^{4+}$ bond. Small changes in the Mn-O-Mn bond properties at an interface can, however, change the transport and magnetic properties significantly.[12-13] During the deposition of the CCO layer of the heterostructure, LSMO was kept in an oxygen deficient environment, and a depleting layer of LSMO was formed close to the CCO/LSMO interface.

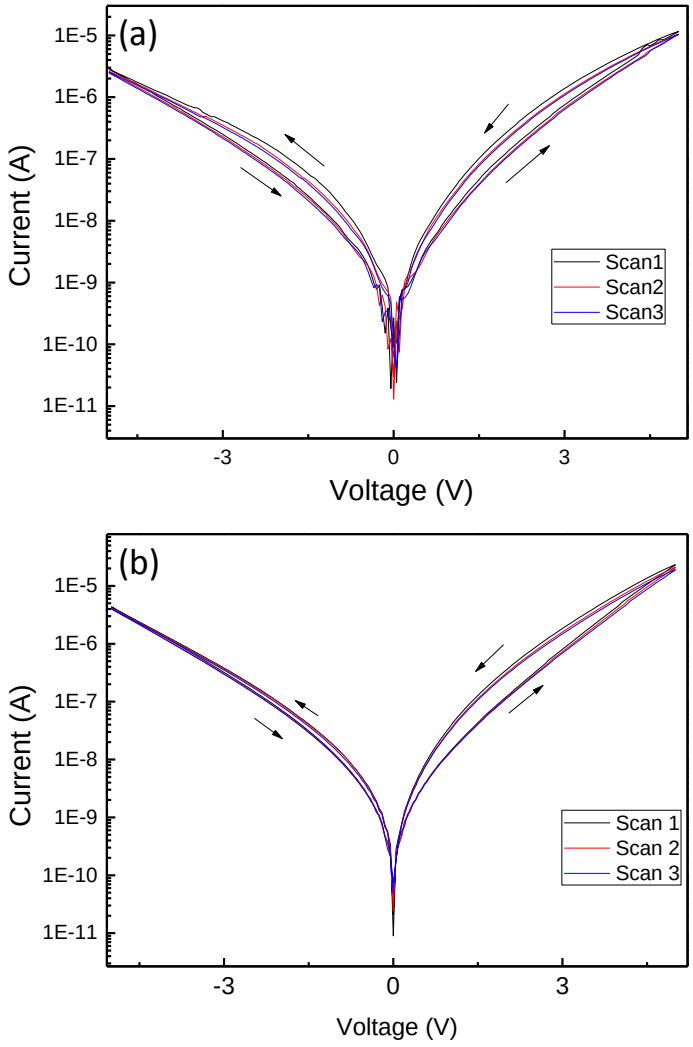


**Figure 6.13** CCP $I$-$V$ curves of 40-nm-thick (a) and 60-nm-thick (b) CCO/LSMO samples.

Hence, in the CCO/LSMO device, the bulk of the LSMO away from the interface is metallic at room temperature, while the interfacial LSMO and the CCO layer are expected to contribute significantly to the resistance of the junction. Since the total resistance of the junction is independent of the thickness of the CCO layer, it is very likely that the oxygen depleting layer of LSMO plays a dominant role in the junction at its high-resistant state, schematically shown in **Figure 6.14**(a). Under a positive forward bias, the voltage is shared by the CCO and interfacial LSMO layer, as shown in **Figure 6.14**(b). As external voltage increases, the voltage across the interfacial LSMO layer will increase and reach a threshold value that can push the

positively charged oxygen vacancies towards the CCO layer, and eventually push them into the CCO layer, as shown in **Figure 6.14**(c). As the oxygen depleting layer of LSMO, which is high-resistant, disappears, any LSMO close to the interface will increase its metallicity, thereby quenching the insulating interfacial barrier layer, leading to switching from the high-resistant state to the low-resistant state. Similarly, when a negative bias is applied to the junction, oxygen vacancies are pushed back into the interfacial LSMO layer, eventually making it insulating, and will switch the device back to high-resistant from the low-resistant state.

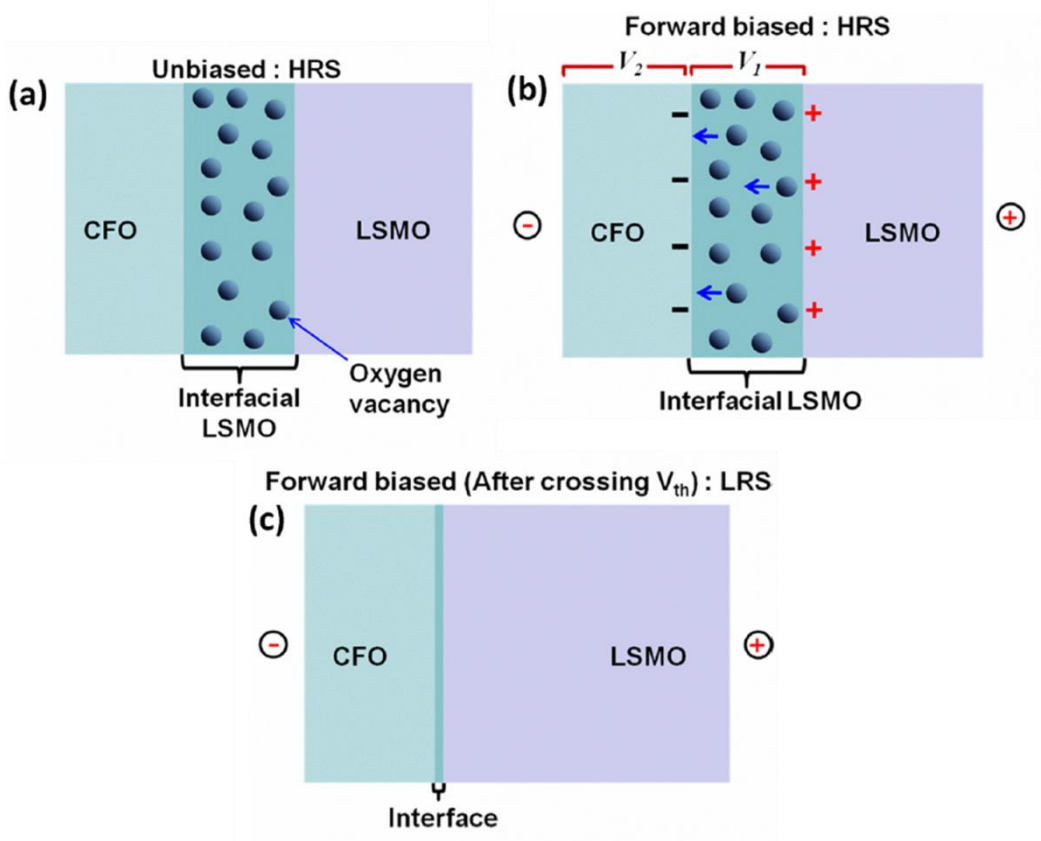


**Figure 6.14** Schematic showing (a) unbiased interfacial barrier formed at LSMO/CFO interface as a result of oxygen vacancies in HRS. (b) Under forward bias before switching and (c) after switching from HRS to LRS. Adapted from Ref.[11]

## 6.5 Summary

CCO thin films on STO substrates are successfully fabricated using PLD. The XRD θ-2θ scan shows that the films are phase pure without secondary phases. However, a noticeable peak shift can be observed in the samples that were grown in low oxygen pressure. The CCO/LSMO heterostructures were grown on STO substrates, as well. A piezoresponse signal in CCO/LSMO heterostructure was picked up by PFM measurements, which was not expected. A changing coercive field with increasing maximum bias voltage suggests that the origin of the piezoresponse is from the ionic motion driven by external electric fields. An interesting resistivity switching behaviour is also observed in the CCO/LSMO heterostructure by C-AFM and conventional $I$-$V$ measurement. Since this behaviour is not thickness sensitive, it is very likely induced from the interface between the CCO and the LSMO. The RS behaviour is explained by the migration of oxygen vacancies in the LSMO near the interface driven by the bias voltage.

References

[1] Y. Tokura,Materials science - Multiferroics as quantum electromagnets, Science 2006, 312, 1481.
[2] H. Katsura, N. Nagaosa, A. V. Balatsky,Spin current and magnetoelectric effect in noncollinear magnets, Phys. Rev. Lett. 2005, 95.
[3] Y. Yamasaki, S. Miyasaka, Y. Kaneko, J. P. He, T. Arima, Y. Tokura,Magnetic reversal of the ferroelectric polarization in a multiferroic spinel oxide, Phys. Rev. Lett. 2006, 96.
[4] Q. N. Chen, Y. Ou, F. Y. Ma, J. Y. Li,Mechanisms of electromechanical coupling in strain based scanning probe microscopy, Appl. Phys. Lett. 2014, 104.
[5] A. Sawa,Resistive switching in transition metal oxides, Mater. Today 2008, 11, 28.
[6] R. Waser, M. Aono,Nanoionics-based resistive switching memories, Nat. Mater. 2007, 6, 833.
[7] R. Waser, R. Dittmann, G. Staikov, K. Szot,Redox-Based Resistive Switching Memories - Nanoionic Mechanisms, Prospects, and Challenges, Adv. Mater. 2009, 21, 2632.
[8] U. Luders, A. Barthelemy, M. Bibes, K. Bouzehouane, S. Fusil, E. Jacquet, J. P. Contour, J. F. Bobo, J. Fontcuberta, A. Fert,NiFe2O4: A versatile spinel material brings new opportunities for spintronics, Adv. Mater. 2006, 18, 1733.
[9] A. V. Ramos, M. J. Guittet, J. B. Moussy, R. Mattana, C. Deranlot, F. Petroff, C. Gatel,Room temperature spin filtering in epitaxial cobalt-ferrite tunnel barriers, Appl. Phys. Lett. 2007, 91.
[10] A. Sawa, T. Fujii, M. Kawasaki, Y. Tokura,Hysteretic current-voltage characteristics and resistance switching at a rectifying Ti/Pr0.7Ca0.3MnO3 interface, Appl. Phys. Lett. 2004, 85, 4073.
[11] V. Thakare, G. Z. Xing, H. Y. Peng, A. Rana, O. Game, P. A. Kumar, A. Banpurkar, Y. Kolekar, K. Ghosh, T. Wu, D. D. Sarma, S. B. Ogale,High sensitivity low field magnetically gated resistive switching in CoFe2O4/La0.66Sr0.34MnO3 heterostructure, Appl. Phys. Lett. 2012, 100.
[12] A. Rana, K. Bogle, O. Game, S. Patil, N. Valanoor, S. Ogale,Nanoscale modulation of electronic states across unit cell steps on the surface of an epitaxial colossal magnetoresistance manganite film, Appl. Phys. Lett. 2010, 96.
[13] A. Urushibara, Y. Moritomo, T. Arima, A. Asamitsu, G. Kido, Y. Tokura,Insulator-Metal Transition and Giant Magnetoresistance in La(1-x)Sr(x)MnO3, Phys. Rev. B 1995, 51, 14103.

# CHAPTER 7

# 7 CONCLUSIONS

## 7.1 Introduction

In this thesis, the PLD growth conditions of non-collinear multiferroic spinels, FVO and CCO, films on STO substrates, with and without electrode (SRO and LSMO) layers, were optimized. Structural characterizations, such as XRD and TEM, were carried out and revealed the epitaxial growth of the films. Various methods, such as XAS, XMCD and MFM, were employed to systematically study the magnetic and electrical properties of epitaxial FVO films. Magnetoelectric coupling in FVO films was revealed by the magnetocapacitance effect in a Pd/FVO/Nb:STO device. Interesting phenomena, such as room temperature piezoresponse and resistance switching, were observed in the CCO/LSMO heterostructure. These phenomena were studied and possible explanations were given. The work on the non-collinear multiferroic spinel thin films can pave the way for a new class of functional materials that can be used in modern devices.

In this final chapter, a summary of the findings about the project is presented, and includes the optimal fabrication conditions of the films, the electron and spin states of FVO films, the magnetic, dielectric properties and magnetocapacitance effect of the FVO films, room temperature piezoresponse and resistivity switching of CCO/LSMO heterostructures. Last but not least, some suggestions for further examination of these interactions and behaviours are proposed, to potentially add to the current academic knowledge and literature in this area.

## 7.2 Growth and Structural Characterization of FVO Films

Because of the instability of the $Fe^{2+}$ and $V^{3+}$ ions at high temperature, it is difficult to get phase pure FVO films. In this study, I tried to eliminate the oxidation of $Fe^{2+}$ and $V^{3+}$ ions by reducing the ambient oxygen pressure during the PLD process. I found that films grown under pressure lower than $1\times10^{-5}$ T ambient pressure show no secondary phase peaks in the XRD θ-2θ scans.

The surface roughness can be affected by changing the deposition temperature. The grain size is larger in high temperature samples than those for low temperature samples, because of the higher grain growth rate at higher temperatures. 500 °C was found to be the optimal deposition temperature to provide a smooth, Rms ≈ 1 nm, surface and optimal crystallization. The deposition temperature also affects the epitaxial strain as the film has more compressive strain as the deposition temperature decreases.

The cross-sectional STEM and SAED images show that the FVO film is cubic-on-cubic epitaxial when grown on the (001) orientated STO substrate and the film is almost fully relaxed, even though there are misfits at the interface and lattice tilting.

In-situ RHEED shows that the growth of FVO is a hybrid 2D to 3D mode. The initial layers of the film follow a layer by layer growth, characterized by the RHEED oscillation and streak-like RHEED pattern. As the film became thicker, the RHEED pattern changed to a spot-like pattern, accompanied by the disappearance of oscillation, indicating an island growth mode.

The integration of FVO film and electrode layers was accomplished by adding an extra cooling step between the depositions of two layers, which minimized oxygen loss in the electrode layer and the oxidation of FVO during the deposition.

### 7.2.1 Magnetic Properties of FVO Film

We employed XAS and XMCD to investigate the electron and spin states of the FVO film. The XAS data shows that Fe ions in the film are mostly divalent and V ions are trivalent. However, a small amount of trivalent $Fe^{3+}$ ions are also found in the Fe $L_2$ edge XAS spectrum, indicating the presence of excess $Fe^{3+}$ in the system, possibly sitting in the octahedral site of the spinel structure. XMCD shows that the magnetic moments of Fe ions are mainly derived from the $Fe^{2+}$, suggesting that $Fe^{3+}$ makes little contribution to the magnetization of FVO films. The opposite sign in the XMCD peak of Fe and V spectra reveals the antiparallel magnetic arrangement of the FVO film. The temperature dependence of the intensity of the main XMCD peak is in good agreement with the M-T curve of the sample, and the trend of the peak intensities of the Fe and V spectra are identical, indicating a strong coupling between the two magnetic orderings.

M-H loops show a strong magnetic anisotropy, such that the OOP magnetization and coercive fields are much larger than those of the IP loops, indicating that the out-of-plane axis is the easy axis. A small magnetic jump at T=0 is also observed in the OOP loops, suggesting the presence of a soft magnet phase, 'phase B', in the system which is decoupled with the main phase, a hard magnet phase, at low temperature.

The magnetic domain of the FVO film was probed by MFM and visually presented as images. The domain size is around 300 nm. By applying an external magnetic field, the magnetic domains can be switched at 3 T. Another switching which occurs at ~ 0.2 T was also observed which could be related to the soft magnet phase in the system.

### 7.2.2 Electrical Properties of FVO Films

The resistivity of the FVO film was measured by the 4-probe method, and the result shows that the resistivity follows the VRH model with an activation energy $E_a$ of 0.29 eV.

The pyroelectric current of the FVO film was measured by a dynamic method, which indicates the spontaneous polarization of the sample. The polarization was

estimated by integrating the pyroelectric current as a function of temperature, which increases as the temperature decreases and saturates at 40 K ($T_{N2}$).

The dielectric properties of the FVO films were investigated by measuring the capacitance (and loss tan) of a Pd/FVO/Nb:STO junction as a function of temperature and frequency. The temperature dependence of the capacitance and $tan\delta$ was simulated by a 2 RC element model. The results show that there are two relaxations, an intrinsic relaxation and an extrinsic Maxwell-Wagner type relaxation, contributing to the total impedance of the junction. At temperatures higher than 40 K, the extrinsic relaxation is dominant. By fitting the variation of the peak position with Arrhenius law, we estimated the activation energy $E_a$ and relaxation frequency $f_0$ as 67 meV and 6.374×10$^8$ Hz, respectively. The frequency dependence of the effective dielectric constant was fitted with the HN model, and the calculated $E_a$ and $\tau_0$ are 81 meV and 0.25 ns, which are very close to the result from 2 RC element simulations.

The magnetocapacitance effect along the out-of-plane was observed by measuring the capacitance as a function of applied magnetic field. The anisotropy of the MC effect of the device is similar to the magnetic anisotropy of the FVO film, and might possibly contribute to the presence of the $Fe^{3+}$ excess 'phase B' in the system.

## 7.3 Piezoresponse and Resistivity Switching of CCO/LSMO Heterostructure

CCO thin films on STO substrates were fabricated using PLD. The XRD θ-2θ scan shows that the films are phase pure without secondary phases. However, a noticeable peak shift can be observed in the samples that were grown in low oxygen pressure. The CCO/LSMO heterostructure were grown on STO substrates, as well.

A piezoresponse signal in CCO/LSMO heterostructure was picked up by PFM measurements, which was not expected. A changing coercive field, with increasing maximum bias voltage, suggested that the origin of the piezoresponse is the ionic motion driven by external electric fields.

An interesting resistivity switching behaviour was also observed in CCO/LSMO heterostructure by C-AFM and conventional I-V measurement. Since this behaviour is not thickness sensitive, it is very likely induced from the interface between CCO and LSMO. It is proposed that the migration of oxygen vacancies in LSMO near the interface are driven by the bias voltage as an explanation of the RS behaviour.

## 7.4 Future Work

Because of the complexity of spinels, especially those which have 2 ions with degrees of freedom in both A and B sites, such as an FVO, there is great potential for future experimentation to further investigate the interaction between the orderings. A potentially effective method is neutron diffraction/reflection, which can be used to closely study the spin structure of the thin film. Low temperature PFM can also be employed to investigate the ferroelectricity of the FVO in its non-collinear magnetic phase. In the form of epitaxial thin film, we can further engineer the material by strain and orientation using different substrates, changing the thickness and introducing different buffer layers.

# PUBLICATION

Dongyi Zhou, Ryota Takahashi, Yanyu Zhou, Dohyung Kim, Vandrangi Kumar Suresh, Ying-Hao Chu, Qing He, Paul Munroe, Mikk Lippmaa, Jan Seidel and Nagarajan Valanoor, Magnetic and Magnetodielectric Properties of Iron Vanadate Thin Films, Accepted by Advanced Electronic Materials, Nov. 2016